12-2014

Microstructure and Magnetic Behavior Studies of Processing-controlled and Composition-modified Fe-Ni and Mn-Al Alloys

Yunlong Geng
University of Nebraska-Lincoln, gengyunlong@gmail.com

Microstructure and magnetic behavior studies of processing-controlled and composition-modified Fe-Ni and Mn-Al alloys

by

Yunlong Geng

A DISSERTATION

Presented to the Faculty of

The Graduate College at the University of Nebraska

In Partial Fulfillment of Requirements

For the Degree of Doctor of Philosophy

Major: Mechanical Engineering and Applied Mechanics

Under the Supervision of Professor Jeffrey E. Shield

Lincoln, Nebraska

December, 2014

Microstructure and magnetic behavior studies of processing-controlled and composition-modified Fe-Ni and Mn-Al alloys

Yunlong Geng, Ph.D.

University of Nebraska, 2014

Adviser: Jeffrey E. Shield

$L1_0$-type (Space group *P4/mmm*) magnetic compounds, including FeNi and MnAl, possess promising technical magnetic properties of both high magnetization and large magnetocrystalline anisotropy energy, and thus offer potential in replacing rare earth permanent magnets in some applications.

In equiatomic Fe-Ni, the disorder-order transformation from fcc structure to the $L1_0$ structure is a diffusional transformation, but is inhibited by the low ordering temperature. The transformation could be enhanced through the creation of vacancies. Thus, mechanical alloying was employed to generate more open-volume defects. A decrease in grain size and concomitant increase in grain boundary area resulted from the mechanical alloying, while an initial increase in internal strain (manifested through an increase in dislocation density) was followed by a subsequent decrease with further alloying. However, a decrease in the net defect concentration was determined by Doppler broadening positron annihilation spectroscopy, as open volume defects utilized dislocations and grain boundaries as sinks.

An alloy, $Fe_{32}Ni_{52}Zr_3B_{13}$, formed an amorphous structure after rapid solidification, with a higher defect concentration than crystalline materials. Mechanical milling was utilized in an attempt to generate even more defects. However, it was observed that

$Fe_{32}Ni_{52}Zr_3B_{13}$ underwent crystallization during the milling process, which appears to be related to enhanced vacancy-type defect concentrations allowing growth of pre-existing Fe(Ni) nuclei. The milling and enhanced vacancy concentration also de-stabilizes the glass, leading to decreased crystallization temperatures, and ultimately leading to complete crystallization.

In Mn-Al, the $L1_0$ structure forms from the parent hcp phase. However, this phase is slightly hyperstoichiometric relative to Mn, and the excess Mn occupies Al sites and couples antiparallel to the other Mn atoms. In this study, the Zr substituted preferentially for the Mn atoms in the Al layer, resulting in an increase in saturation magnetization, from 115 emu/g in the alloys without Zr to 128 emu/g in $Mn_{53}Al_{43}C_3Zr_1$. To further improve the coercivity in $Mn_{53}Al_{43}C_3Zr_1$, microstructure modification was achieved through the addition of excessive C and through surfactant-assisted mechanical milling. Enhancement in coercivity was accomplished through the microstructure modification, however, the loss of saturation magnetization was observed due to the formation of other equilibrium phases, including ε, β-Mn and ZrO.

Acknowledgements

I would like to show my appreciation to all the people who have helped me along this venture.

First and foremost, I'd like to send my deepest appreciation to my advisor, Dr. Jeffery E. Shield, for his support and guidance during my PH. D. period. I want to thank Dr. Shield for his timely rescue when I lost my faith in academia. I want to thank Dr. Shield for the patient guidance, consistent encouragement and constructive discussions not only on the research but also on my life. He pointed the right direction for my future professional life and set up a perfect sample as a scientist. Thank you, Dr. Shield, for the trust and support which helped me to realize my potentials.

I also would like to thank my wife, Lu Ren, for accompanying with me through my PH. D. time and supporting me during my hard times. And thank my parents and my brothers for their encouragement all the time.

I'd like to thank Dr. Jiashi Yang of the Department of Mechanical & Materials Engineering for the suggestions and recommendations during my application for the PHD program at the University of Nebraska-Lincoln.

I'd like to thank all my committee members: Dr. Jinsong Huang, Dr. Mehrdad Negahban, Dr. Joseph A. Turner from the Department of Mechanical & Materials Engineering, and Dr. Barry Cheung from the Department of Chemistry, for all the guidance and constructive criticism on my research.

I want to extend my sincere gratitude to Dr. Sellmyer for the access to the SQUID, XRD, VSM, SEM, TEM, and AFM. Thanks to Dr. Steven Michalski and Dr. Balamurugan Balasubramanian for training me on SQUID and VSM, Dr. Xingzhong Li on SEM and TEM, Dr. Shah Valloppilly on XRD, and Dr. Lanping Yue on the AFM. Without these facilities, I could never finish my research. Thanks to Dr. Ralph Skomski for the introduction to theory of magnetism.

My special thanks to Dr. Kelvin Lynn, Dr. Marc Weber and Mr. Tursunjan Ablekim for the excellent collaboration on defects concentration study and for the permission of using Doppler broadening positron annihilation spectroscopy.

My greatest thanks will go to my best friends at UNL. My excellent friends in my lab group, Jay T V Jayaraman, Jordan Bornhoft, Mark Koten, Meiyu Wang, Michael Lucis, Pinaki Mukherjee, Xiujuan Jiang, Yuan Tian, and Pam Rasmussen, thanks for making my PHD time so colorful and for the valuable discussions. My coolest friends, Junyi Yang, Qiang Wang, Yao Li, on basketball; Mark Koten, on workout and Shumin Li, Zhanping Xu, Jinya Pu, on fishing; thanks for making my spare time so exciting.

The research conducted in this dissertation could not be accomplished without the funding support from the National Science Foundation and the Department of Energy. I would also give my great thanks to the Central Facilities of the Nebraska Center for Materials and Nanoscience, which is supported by the Nebraska Research Initiative.

Table of Contents

List of Figures

List of Tables

Chapter 1 Introduction

1. 1 Background of Permanent Magnets

Permanent magnets have the unique ability to retain their magnetism even after an applied magnetic field is removed. This characteristic is due to their high magnetocrystalline anisotropy and stability of their magnetization direction with respect to their crystal axes[1]. Magnetic anisotropy is essentially the source of hysteresis and coercivity, which distinguishes permanent magnets (hard magnets) from soft magnetic materials. Compared to electromagnets, permanent magnets can create a magnetic field H in free space without the continuous expenditure of electric or other forms of energy, and thus play an essential role in modern society.

Not only are permanent magnets becoming more common by replacing electromagnets for many purposes, including small motors, dynamos and microwave generators, they are also increasingly becoming indispensable components of many mass-market consumer goods like medical devices, industrial products, and are also part of countless new applications[2]. As a result, magnet ownership by middle-class families has increased nearly a hundred-fold, from barely a handful to one or two hundred, although most people would be hard pressed to identify where these magnets are found Applications for these magnets can be classified into three categories, uniform, nonuniform, and steady[3] (Table 1.1).

Table 1.1 Summary of permanent magnet applications[3]

Field	Magnetic effect	Type	Examples
Uniform	Zeeman splitting	Static	Magnetic resonance imaging
	Torque	Static	Alignment of magnetic powder
	Hall effect, magnetoresistance	Static	Sensors, read-heads
	Force on conductor	Dynamic	Motors, actuators, loudspeakers
	Induced emf	Dynamic	Generators, microphones
Nonuniform	Force on charged particles	Static	Beam control, radiation sources (microwave, uv; X-ray)
	Force on magnet	Dynamic	Bearings, couplings, Maglev
	Force on paramagnet	Dynamic	Mineral separation
Time varying	Varying field	Dynamic	Magnetometers
	Force on iron	Dynamic	Switchable clamps, holding magnets
	Eddy currents	Dynamic	Metal separation, brakes

The earliest permanent magnets known as lodestones were discovered in nature and were composed of naturally occurring Fe_3O_4 containing a fine intergrowth of γ-Fe_2O_3 produced by oxidation[4]. In these kinds of magnets the fine two-phase microstructure inhomogeneity impede magnetic reversal, resulting in coercivity. The first artificial permanent magnets were iron needles “touched” by a lodestone. It has been used as the compass for navigation if supported by a floating straw.

Carbon steels of greater mechanical and magnetic hardness did not become widely used until the late 19th century. These magnets produced a coercivity of 50 Oe with maximum energy products of about 0.3 MGOe which resulted from a possible martensitic microstructure[5]. Fe-based alloys including Fe-W, Fe-Mo, Fe-Cr and Fe-Co-Cr produced even higher coercivity of 90~250 Oe with energy products of ~1 MGOe.

In addition to these historical advances, the development of modern permanent magnetic materials began with the discovery of Alnico[6]. With its high coercivity of 600 Oe and energy products of 1.3 MGOe Alnico was the new standard for permanent magnets. Alnico alloys owe their high coercivity to the needle-like precipitaion of Fe(Co) via spinodal decomposition[7,8]. Further studies on the effects of alloying additions and variations in the processing of Alnico are still going on until today[9-12]. The energy products reach as high as 10 MGOe[13].

Different from the shape anisotropy in Alnico, ferrites derive their hard magnetic behavior from magnetocrystalline anisotropy along the c-axis of the hexagonal $MO.6Fe_2O_3$ (M=Ba or Sr) phase. Aligning the ferrite particles with a magnetic field before pressing and sintering enhances their high coercivity of 2~5 kOe, yielding an energy product of 4.5 MGOe[14]. In spite of their relatively modest magnetic properties, the ferrite magnets still show the best performance to cost ratio, and remain the most-used permanent magnet material both in tonnage and in value[15].

The revolutionary introduction of rare-earth magnets in consumer applications began with their discovery and development due to their large magnetocrystalline anisotropy. The discovery of Sm_5Gd, a rare-earth magnet with a high coercivity of ~8kOe but low net magnetization, was first reported in 1960[16]. The Co_5R compound

boasts a hexagonal structure that can generate sufficiently high crystal anisotropies, magnetizations and curie temperatures with proper R elements[17]. Co_5Sm, a rare-earth magnet produced by liquid phase sintering of magnetically-aligned powder, showed a coercivitiy over 50 kOe and energy products over 25 MGOe. Meanwhile, $Co_{17}R_2$, with higher magnetization but lower coercivity than Co_5R, led to a new generation of rare-earth magnets[18].

Later in the 1970s, cost and supply problems with Co drove the discovery of iron-rare earth compounds. The most notable of these compounds is $Fe_{14}Nd_2B$[19,20] with energy products of >50 MGOe in laboratory settings. These Fe-Nd-B magnets attracted considerable attention because of their higher energy products and less expensive price when compared with Co-Sm magnets. In rare-earth magnets, the transition-metal components provide high magnetization, and the rare-earth components contribute a very large magnetocrystalline anisotropy that produces a high resistance to demagnetization[21].

A summary of different permanent magnetic materials with the corresponding energy product can be found in Figure 1.1[22]. The remarkable increase in the energy product in the hard magnetic materials was accompanied with the tremendous decrease in the volume of the magnets providing the same amount of magnetic energy. The current commercially available hard magnets are mainly hard ferrites, Alnico, $SmCo_5$ and Sm_2Tm_{17} (Tm=Co, Fe, Zr, and Cu), SmFeN and NdFeB.

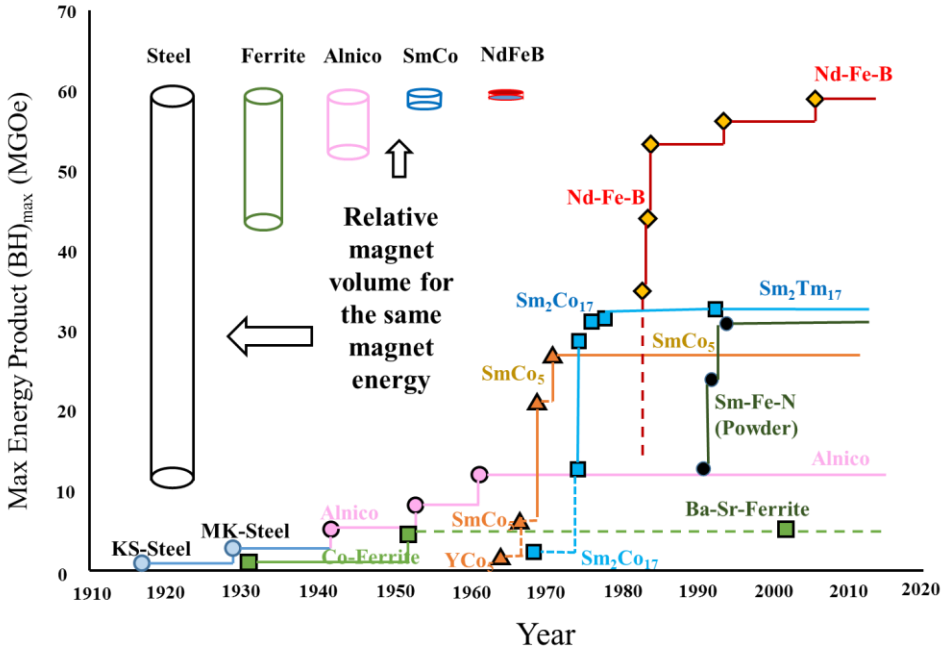

Figure 1.1 Development in energy product of permanent magnetic materials[22]

The rare-earth permanent magnets have become the most important permanent magnets in the market owing to their excellent magnetic properties at room temperature and their relatively low cost per energy-density unit, However, supply chain issues in recent years have created both price and availability issues[23]. The demand for permanent magnets is increasing due to their numerous commercial applications in motors, actuators, generators, wind turbines and hybrid cars. Not only increased demand but limited export from China has led to increased prices for these materials in recent years. These problems are forcing both industry and consumers to pay attention to the possibilities of developing rare-earth-free permanent magnetic materials with large magnetic anisotropy. One way to do this is by using them in conjunction with other magnetic materials systems by controlling their crystal structure, the nanostructure and/or the microstructure of alloys and compounds composed of common and plentiful elements[24]. While the majority of

strongly magnetic transition metal alloys assume a high-symmetry cubic structure that displays low magnetocrystalline anisotropy, certain transition-metal alloys compounds form in the tetragonal $L1_0$ (space group *P4/mmm* or AuCu I structure type) structure, with an associated uniaxial magnetic character. Two of these magnetic compounds that adopt the $L1_0$-type structure—FeNi and MnAl—are anticipated to yield promising technical magnetic properties[21].

1. 2 Overview of $L1_0$-FeNi permanent magnets

$L1_0$-FeNi has a chemically ordered structure consists of alternating Fe and Ni layers along the c-axis, as shown in Fig. 1.2. The reduced symmetry from the fcc to the tetragonal $L1_0$ structure induces a strong magnetocrystalline anisotropy along the [001] direction for $L1_0$ FeNi[25]. $L1_0$-FeNi is known to have high coercivity (500–4000 Oe), magnetic anisotropy (1.3×10^7 erg/cm^3), and a theoretical maximum energy product comparable to the best rare-earth permanent magnets[25-29]. Meanwhile, Fe and Ni are both abundant and inexpensive. Thus, shedding light on $L1_0$-FeNi is a matter of great interest in the field of magnetic materials science due to their comparatively low cost of production[30]. However, due to the extremely low atomic Fe and Ni mobility, the $L1_0$ phase has not yet been produced in bulk by conventional metallurgy methods.

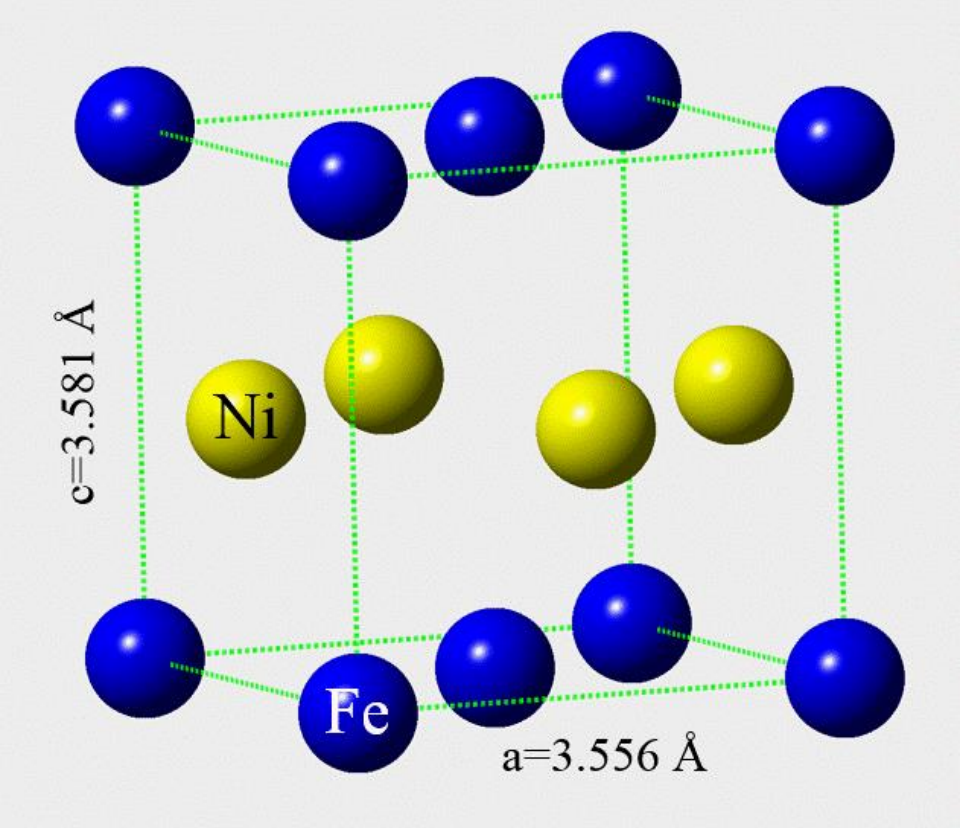

Figure 1.2 Schematic unit cell of superstructure $L1_0$-FeNi

$L1_0$-FeNi was first discovered in an iron meteorite, formed by the long-range thermal diffusion of Fe and Ni in an asteroid's core over a period of 4.6 billion years[31]. The chemical composition, electronic structure, lattice structure and magnetic domains in the iron meteorite were investigated by photoelectron emission microscopy, which revealed its perpendicular magnetic component in the magnetic domain structure with Bloch wall. This characteristic can be ascribed to the large amount of magnetic anisotropy energy found in $L1_0$-FeNi[32-35]. Furthermore, the origin of strong magnetic anisotropy energy (MAE) in $L1_0$-type ordered FeNi phase was studied by angular-dependent magnetic circular dichroism which revealed that the magnetic anisotropy arises from spin–orbit interaction in the 3d electrons of Fe[36]. Recently, fundamental solid-

state properties including sample composition, magnetic hysteresis, crystal structure and electronic structure of $L1_0$-FeNi extracted from a natural meteorite have been analyzed separately by multidirectional analyses using scanning electron microscopy with an electron probe micro-analyzer (SEM-EPMA), a superconducting quantum interference device (SQUID), x-ray diffraction (XRD) and magnetic circular dichroism (MCD). It's obtained that the composition of these materials was confirmed as Fe: 50.47 ±1.98 at.%, Ni: 49.60 ±1.49 at.%, with lattice constants estimated to be a =b=3.582 Å and c=3.607 Å[30].

As shown in the phase diagram (Fig. 1.3), FeNi is a continuous solid solution at high temperature, and the $L1_0$ phase (γ'') is an equilibrium phase below 320℃[37,38]. The ordering to $L1_0$ phase never occurs over this temperature, but the diffusion rates of Fe/Ni atoms are extremely slow below the critical chemical order/disorder temperature[39]. It takes more than 10^4 years to finish one atomic jump at 300℃[25]. Therefore, the $L1_0$-FeNi has not yet been produced in bulk by conventional metallurgy methods.

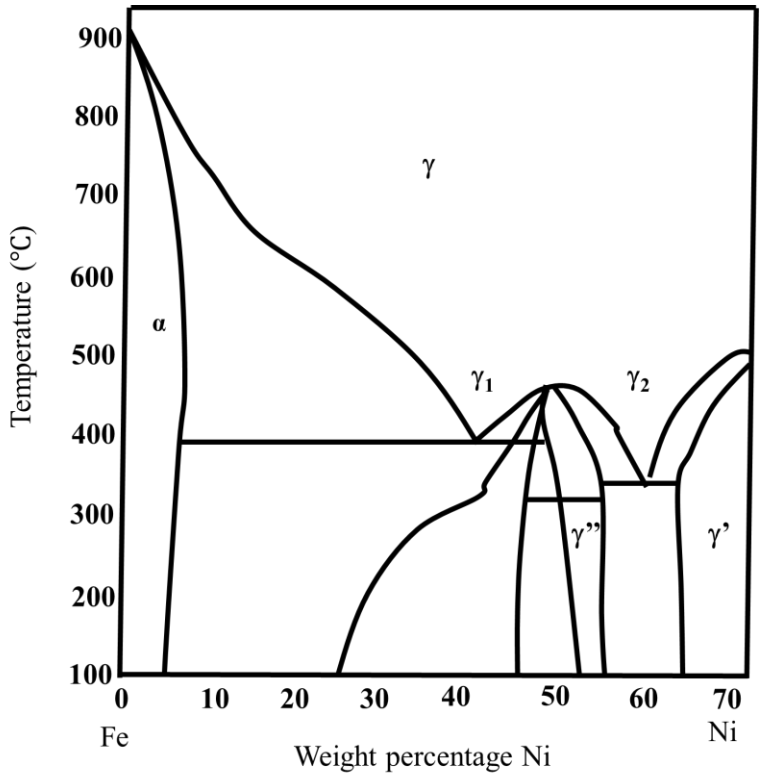

Figure 1.3 The phase diagram of Fe-Ni alloy[37,38]

Ordered $L1_0$-FeNi structure without quadratic distortion in an iron-nickle alloy (50%-50%) was firstly constructed by bombarding a polycrystalline sample with neutrons at ~295℃[25]. High anisotropy constant $K_1=3.2\times10^{-6}$ ergs/cm^3 was firstly obtained experimentally. However, this approach cannot be utilized in bulk due to the high cost and difficulty in massive production. Alternate monatomic layer (ML) deposition technique using molecular beam epitaxy is one approach that has been successfully employed to fabricate the $L1_0$-FeNi. Alternating Fe (0 0 1) and Ni (0 0 1) MLs on MgO (0 0 1) substrates were prepared at 240 ℃, showing the highest degree of ordering and a higher anisotropy constant of 6.3×10^{-6} ergs/cm^3. Since lattice mismatch could induce stain in the Fe-Ni thin film, a variety of buffer layers including Cu[40], AuNi[41], CuNi[42] and Au-Cu-Ni[43] were investigated. It has been reported that magnetic anisotropy is

proportional to the degree of ordering, and a highest magnetic anisotropy of 7.0×10^{-6} ergs/cm^3 was observed with a degree of order of 0.48 with buffer layer of Au-Cu-Ni[43]. However, the magnetic anisotropy of as-synthesized $L1_0$-FeNi has not reached the upper limit yet and the fundamental physical properties of the $L1_0$-FeNi phase are not yet accurately clarified.

1. 3 Overview of Mn-Al permanent magnets

Mn-Al permanent magnets, made of inexpensive elements, shows good magnetic properties superior to even the well-known Alnicos and hard ferrites[44]. Due to the presence of the intermetallic tetragonal $L1_0$ phase (τ phase), Mn-Al shows strong, uniaxial magnetocrystalline anisotropy energy. It was reported that the potential maximum energy product could be as high as 12.64 MGOe, and the magnetocrystalline anisotropy field ~40 kOe[45]. Thus, Mn-Al is a promising rare-earth-free permanent magnetic material[46].

The existence of the ferromagnetic τ phase in Mn-Al system was first discovered in the early 20th century[47,48], but it was not until 1958 that the metallographical investigation of the Mn-Al system was made in the compositional range of 47 at.% to 60 at.% of Mn[49]. The τ phase was found to be formed from the ε phase (hexagonal close packed form) through heat treatment with about 54 atomic percent of manganese. The ε phase, the parent phase to the ferromagnetic τ phase, forms in the range of 53~60 at.% at high temperature[50]. Thus the ε phase could not be formed from equilibrium processing techniques, which require sufficient undercooling to retain the ε phase at room temperature.

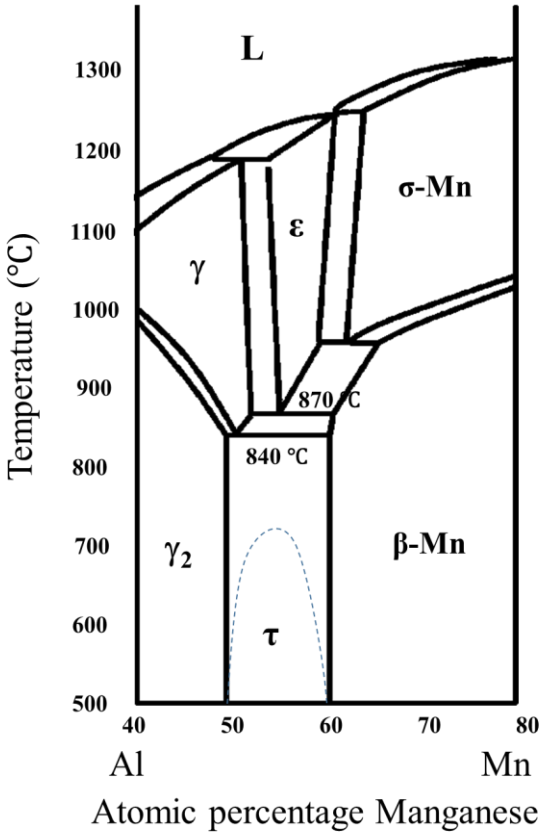

Figure 1.4 Al-Mn binary phase diagram with proposed metastable τ phase region[50]

In general, the τ phase was produced by quenching the high temperature ε phase followed by proper heat treatment, or by cooling the ε phase at a controllable rate[51,52]. The magnetic properties of τ-MnAl is dependent on the composition and microstructure of the materials, which are affected by preparation techniques and subsequent heat treatment process. Up to now, various techniques have been applied to obtain τ-MnAl including mechanical alloying[53], magnetron sputtering[51,54,55], pulsed laser deposition[56], melt spinning[57], plasma arc discharge[58] , hot extrusion[59] and atomization[60]. Mechanical alloying of Mn-Al and Mn-Al-C followed by heat treatment at relatively low temperatures (500-700 ℃) resulted in the formation of the metastable τ phase[53]. A low saturation magnetization (8~20 emu/g) and high coercivity (~3.3 kOe) were obtained, and

these were attributed to the amount of τ phase formed during mechanical alloying. Heat treatment of Mn/Al multilayer from magnetron sputtering drives the formation of τ phase having coercivity ~4 kOe, but the magnetization depends on the thickness of Mn and Al layers[51,54,55]. The highest coercivity of ~6.7 kOe was observed in epitaxial thin film of τ-MnAl grown on (100) GaAs substrate by pulsed laser deposition[56]. Isotropic $Mn_{54}Al_{44}C_2$ ribbons, produced by melt-spinning and subsequent annealing (~500 ℃), resulted in coercivity of ~2 kOe and an energy product of ~1.5 MGOe[57]. Spherical Mn-Al nanoparticles (~100 nm) were synthesized using plasma arc discharge. The highest coercivity of ~6 kOe was achieved in the composition of $(Mn_{20}Al_{80})_{0.95}C_{0.05}$ after heat treatment at 500 ℃ for 30 min[58]. Larger Mn-Al particles (10~80 μm) were produced by gas-water atomization with saturation magnetization 100 emu/g and coercivity ~2 kOe[60].

As shown in the phase diagram (Figure 1.4), the τ-phase is formed in the two-phase region consisting of γ_2 and β-Mn (dashed lines in Figure 1.4). In this phase the material is metastable, with a higher annealing temperature and elongated annealing time, the τ phase will decompose into γ_2 and β-Mn phases. The addition of a small percentage of Carbon proved to enhance its stability, improve the magnetic properties but decrease the Curie temperature[46,59,61-63]. The highest coercivity was observed to be ~5.2 kOe in $Mn_{51}Al_{46}C_3$ with a saturation magnetization of ~70 emu/g. The coercivity is due to the existence of Mn_3AlC phase in the τ phase that can pin the domain walls and improve coercivity. The highest saturation magnetization (134 emu/g) was reported in the $Mn_{54}Al_{44}C_2$ alloy[64], but its coercivity is relatively low at 1.39 kOe. $Mn_{53}Al_{44}C_3$ alloy has a combination of saturation magnetization (115 emu/g) and coercivity (1.7 kOe), but it has a higher phase purity than other alloys.

Another shortfall of the τ- phase MnAl is its lower saturation magnetization, especially compared to Fe- or Co-based permanent magnets. While the Al layer in the $L1_0$ structure effectively increases the Mn-Mn distances, resulting in ferromagnetic coupling, its presence dilutes the magnetization. Further, the $L1_0$ phase in this system is hyperstoichiometric relative to Mn, as the minimum Mn content is governed by the composition of the ε phase from which τ forms. In τ phase of $Mn_{54}Al_{46}$ alloy, 4% of the Mn atoms occupy Al sites, which couple antiferromagnetically with the Mn layers, resulting in a decrease in the saturation magnetization over stoichiometrically perfect $L1_0$[45]. Therefore, one approach to substitutional alloying is to target the Mn atoms in the Al layer, replacing them with non-magnetic atoms which would effectively increase the magnetization.

The alloying effects of several elements including Ti, Ni, Zn, Cu, B, Dy and Pr to substitute the Mn atoms in the Al layer in Mn-Al alloy has been studied[63,65-67]. A decrease of magnetization and constant coercivity were observed with Ni addition[65]. Enhancement of coercivity from 1 kOe to 3 kOe and a reduction in magnetization were caused by doping of B[64]. The phase transformation to τ was slowed by the addition of Ti and Cu, and showed no influence on the magnetic properties of Mn-Al alloys[65]. Mn-Al-Zn alloy, prepared by water quenching the induction-melted alloy followed by heat treatment at 420℃ for 1 h, showed the trend of magnetization with an initial increase followed by a decreasing after Zn additions at more than 1.6 at.%[66]. However, the magnetization of Mn-Al alloy prepared by this technique yields as low as ~15 emu/g while more than ~100 emu/g is produced from melt-spinning followed by heat treatment at 500℃ for 10 min. Doping of rare-earth elements Pr and Dy, however, improved the magnetic properties

slightly. The anisotropy constant enhancements were attributed to either the 3d–4f electron interactions or simply the increase in atomic distance between Mn atoms[63].

As is the case with all magnetic materials, the microstructure, including grain size, texture and defects, all play a critical role in maximizing the extrinsic properties, namely coercivity and remanence. Advancements in grain refinement for Mn-Al have been made by mechanical milling and surfactant-assisted mechanical milling[68,69]. Mechanical milling of ε-phase Mn-Al alloy obtained from gas atomization[68] and melt-spinning[69] resulted in higher coercivity with a loss of magnetization. An even more dramatic loss of magnetization was observed in τ-phase milled alloy[69]. Therefore, an improvement of the magnetic properties to its theoretical energy product is a prerequisite for the Mn-Al permanent magnets to be applied in industry.

1. 4 Objectives

This study aims to develop a new generation of rare-earth-free permanent magnets with magnetic properties between ferrites and NdFeB. In the Fe-Ni system, it could be achieved by the enhancement of the diffusion rate at room temperature, which would shorten the time of the phase transformation from fcc to fct ($L1_0$). Understanding the relationship between defect concentration and mechanical milling is critical in the application of mechanical milling in the design of future magnetic materials. In Mn-Al system, optimization of composition and microstructure for excellent magnetic properties will be explored, and offer references for the improvement of magnetic properties in other permanent magnets.

Specifically, the objectives are:

- To study the defect concentration including grain boundary, dislocations and vacancy/vacancy agglomerates generated by high-energy mechanical milling in Fe-Ni systems;
- To explore the mechanism of milling-induced crystallization;
- To improve the magnetic performance of Mn-Al alloy.

References

1 Skomski, R. & Coey, J. *Permanent magnetism*. (Institute of Physics Publishing Bristol, 1999).

2 Coey, J. Permanent magnets: Plugging the gap. *Scripta Materialia* **67**, 524-529 (2012).

3 Coey, J. Permanent magnet applications. *Journal of Magnetism and Magnetic Materials* **248**, 441-456 (2002).

4 Wasilewski, P. Lodestone-explanation for magnetic properties and characterization of the source of magnetic hardening. *Journal of Applied Physics* **50**, 2428-2430 (1979).

5 Hoselitz, K. Ferromagnetic properties of metals and alloys. (1952).

6 Mishima, T. Nickel-aluminum steel for permanent magnets. *Ohm* **19**, 353 (1932).

7 Bradley, A. & Taylor, A. An X-ray study of the iron-nickel-aluminium ternary equilibrium diagram. *Proceedings of the Royal Society of London. Series A. Mathematical and Physical Sciences* **166**, 353-375 (1938).

8 Bradley, A. & t FRS, M. AN X-RAY INVESTIGATION OF ALUMINIUM-864 RICH IRON-NICKEL-ALUMINIUM ALLOYS AFTER SLOW COOLING. *The Journal of the Institute of Metals* **66**, 53 (1940).

9 Dillon, H. M. Effects of heat treatment and processing modifications on microstructure in alnico 8H permanent magnet alloys for high temperature applications. (2014).

10 Hadjipanayis, G., Frincu, B., Löwe, K., Hu, X. & Gutfleisch, O. Effect of Grain Size on Spinodal Decomposition and Magnetic Properties in Melt-Spun Alnico Alloys. *Bulletin of The American Physical Society* (2014).

11 Liu, T., Li, W., Zhu, M., Guo, Z. & Li, Y. Effect of Co on the thermal stability and magnetic properties of AlNiCo 8 alloys. *Journal of Applied Physics* **115**, 17A751 (2014).

12 Palasyuk, A., Blomberg, E., Prozorov, R., Yue, L., Kramer, M., Mccallum, R., Anderson, I. & Constantinides, S. Advances in Characterization of Non-Rare-Earth Permanent Magnets: Exploring Commercial Alnico Grades 5–7 and 9. *JOM* **65**, 862-869 (2013).

13 Cronk, E. R. Recent Developments in High-Energy Alnico Alloys. *Journal of Applied Physics* **37**, 1097-1100 (1966).

14 Sechovsky, V., Havela, L., Wohlfarth, E. & Buschow, K. Ferromagnetic Materials. *Vol. 4North-Holland, Amsterdam*, 309 (1988).

15 Tenaud, P., Morel, A., Kools, F., Le Breton, J. & Lechevallier, L. Recent improvement of hard ferrite permanent magnets based on La–Co substitution. *Journal of Alloys and Compounds* **370**, 331-334 (2004).

16 Hubbard, W. M., Adams, E. & Gilfrich, J. Magnetic Moments of Alloys of Gadolinium with Some of the Transition Elements. *Journal of Applied Physics* **31**, S368-S369 (1960).

17 Strnat, K. J. COBALT-RARE-EARTH ALLOYS AS PROMISING NEW PERMANENT-MAGNETIC MATERIALS. *COBALT, SEPT. 1967,--36--, 133-143* (1967).

18 Tawara, Y. & Strnat, K. Rare earth-cobalt permanent magnets near the 2-17 composition. *Magnetics, IEEE Transactions on* **12**, 954-958 (1976).

19 Sagawa, M., Fujimura, S., Togawa, N., Yamamoto, H. & Matsuura, Y. New material for permanent magnets on a base of Nd and Fe. *Journal of Applied Physics* **55**, 2083-2087 (1984).

20 Croat, J. J., Herbst, J. F., Lee, R. W. & Pinkerton, F. E. Pr-Fe and Nd-Fe-based materials: A new class of high-performance permanent magnets. *Journal of Applied Physics* **55**, 2078-2082 (1984).

21 Lewis, L. H. & Jiménez-Villacorta, F. Perspectives on permanent magnetic materials for energy conversion and power generation. *Metallurgical and Materials Transactions A* **44**, 2-20 (2013).

22 Gutfleisch, O. Controlling the properties of high energy density permanent magnetic materials by different processing routes. *Journal of Physics D: Applied Physics* **33**, R157 (2000).

23 Poudyal, N. & Liu, J. P. Advances in nanostructured permanent magnets research. *Journal of Physics D: Applied Physics* **46**, 043001 (2013).

24 Nummy, T., Bennett, S., Cardinal, T. & Heiman, D. Large coercivity in nanostructured rare-earth-free MnxGa films. *Applied Physics Letters* **99**, 252506 (2011).

25 Néel, L., Pauleve, J., Pauthenet, R., Laugier, J. & Dautreppe, D. Magnetic Properties of an Iron—Nickel Single Crystal Ordered by Neutron Bombardment. *Journal of Applied Physics* **35**, 873-876 (1964).

26 Albertsen, J., Knudsen, J. & Jensen, G. Structure of taenite in two iron meteorites. *Nature* **273**, 453 (1978).

27 Clarke, R. S. & Scott, E. R. Tetrataenite; ordered FeNi, a new mineral in meteorites. *American Mineralogist* **65**, 624-630 (1980).

28 Albertsen, J. Tetragonal lattice of tetrataenite (ordered Fe-Ni, 50-50) from 4 meteorites. *Physica Scripta* **23**, 301 (1981).

29 Nagata, T. & Funaki, M. Tetrataenite phase in Antarctic meteorites. *Memoirs of National Institute of Polar Research. Special issue* **46**, 245-262 (1987).

30 Kotsugi, M., Maruyama, H., Ishimatsu, N., Kawamura, N., Suzuki, M., Mizumaki, M., Osaka, K., Matsumoto, T., Ohkochi, T. & Ohtsuki, T. Structural, magnetic and electronic state characterization of L1 0-type ordered FeNi alloy extracted from a natural meteorite. *Journal of Physics: Condensed Matter* **26**, 064206 (2014).

31 Yang, C.-W., Williams, D. & Goldstein, J. Low-temperature phase decomposition in metal from iron, stony-iron, and stony meteorites. *Geochimica et Cosmochimica Acta* **61**, 2943-2956 (1997).

32 Kotsugi, M., Mitsumata, C., Maruyama, H., Wakita, T., Taniuchi, T., Ono, K., Suzuki, M., Kawamura, N., Ishimatsu, N. & Oshima, M. Novel magnetic domain structure in iron meteorite induced by the presence of $L1_0$-FeNi. *Applied physics express* **3**, 013001 (2010).

33 Kotsugi, M., Mizuguchi, M., Sekiya, S., Ohkouchi, T., Kojima, T., Takanashi, K. & Watanabe, Y. in *Journal of Physics: Conference Series.* 012095 (IOP Publishing).

34 Kotsugi, M., Wakita, T., Taniuchi, T., Maruyama, H., Mitsumata, C., Ono, K., Suzuki, M., Kawamura, N., Ishimatsu, N. & Oshima, M. Direct metallographic analysis of an iron meteorite using hard x-ray photoelectron emission microscopy. *IBM Journal of Research and Development* **55**, 13: 11-13: 15 (2011).

35 Kotsugi, M., Wakita, T., Kawamura, N., Taniuchi, T., Ono, K., Suzuki, M., Oshima, M., Ishimatsu, N., Taniguchi, M. & Maruyama, H. Application of photoelectron emission microscopy (PEEM) to extraterrestrial materials. *Surface Science* **601**, 4764-4767 (2007).

36 Kotsugi, M., Mizuguchi, M., Sekiya, S., Mizumaki, M., Kojima, T., Nakamura, T., Osawa, H., Kodama, K., Ohtsuki, T. & Ohkochi, T. Origin of strong magnetic anisotropy in L1< sub> 0</sub>-FeNi probed by angular-dependent magnetic circular dichroism. *Journal of Magnetism and Magnetic Materials* **326**, 235-239 (2013).

37 Chuang, Y.-Y., Chang, Y. A., Schmid, R. & Lin, J.-C. Magnetic contributions to the thermodynamic functions of alloys and the phase equilibria of Fe-Ni system below 1200 K. *Metallurgical Transactions A* **17**, 1361-1372 (1986).

38 Reuter, K., Williams, D. & Goldstein, J. Determination of the Fe− Ni phase diagram below 400 °C. *Metallurgical Transactions A* **20**, 719-725 (1989).

39 Shima, T., Okamura, M., Mitani, S. & Takanashi, K. Structure and magnetic properties for L1< sub> 0</sub>-ordered FeNi films prepared by alternate monatomic layer deposition. *Journal of Magnetism and Magnetic Materials* **310**, 2213-2214 (2007).

40 Mizuguchi, M., Sekiya, S. & Takanashi, K. Characterization of Cu buffer layers for growth of L1 0-FeNi thin films. *Journal of Applied Physics* **107**, 09A716-709A716-713 (2010).

41 Mizuguchi, M., Kojima, T., Kotsugi, M., Koganezawa, T., Osaka, K. & Takanashi, K. Artificial fabrication and order parameter estimation of $L1_0$-ordered FeNi thin film grown on a AuNi buffer layer. *Journal of the Magnetics Society of Japan* **35**, 370-373 (2011).

42 Kojima, T., Mizuguchi, M. & Takanashi, K. in *Journal of Physics: Conference Series.* 012119 (IOP Publishing).

43 Kojima, T., Mizuguchi, M., Koganezawa, T., Osaka, K., Kotsugi, M. & Takanashi, K. Magnetic Anisotropy and Chemical Order of Artificially Synthesized $L1_0$-Ordered FeNi Films on Au–Cu–Ni Buffer Layers. *Japanese Journal of Applied Physics* **51**, 010204 (2012).

44 Zeng, Q., Baker, I., Cui, J. B. & Yan, Z. C. Structural and magnetic properties of nanostructured Mn–Al–C magnetic materials. *Journal of Magnetism and Magnetic Materials* **308**, 214-226, doi:10.1016/j.jmmm.2006.05.032 (2007).

45 Park, J., Hong, Y., Bae, S., Lee, J., Jalli, J., Abo, G., Neveu, N., Kim, S., Choi, C. & Lee, J. Saturation magnetization and crystalline anisotropy calculations for MnAl permanent magnet. *Journal of Applied Physics* **107**, 09A731-709A731-733 (2010).

46 Ohtani, T., Kato, N., Kojima, S., Kojima, K., Sakamoto, Y., Konno, I., Tsukahara, M. & Kubo, T. Magnetic properties of Mn-Al-C permanent magnet alloys. *Magnetics, IEEE Transactions on* **13**, 1328-1330 (1977).

47 Hindrichs, G. Some Cr and Mn Alloys. *Z. Anorg. Chem.* **59**, 420-423 (1908).

48 Koster, W. & Bechthold, W. The Manganese-Aluminum Systems. *Z. Metallkd.* **30**, 294-296 (1938).

49 Kōno, H. On the ferromagnetic phase in manganese-aluminum system. *Journal of the Physical Society of Japan* **13**, 1444-1451 (1958).

50 Massalski, T. B., Okamoto, H., Subramanian, P. & Kacprzak, L. *Binary alloy phase diagrams*. (ASM international, 1990).

51 Duan, C. Y., Qiu, X. P., Ma, B., Zhang, Z. Z. & Jin, Q. Y. The structural and magnetic properties of τ-MnAl films prepared by Mn/Al multilayers deposition plus annealing. *Materials Science and Engineering: B* **162**, 185-188, doi:10.1016/j.mseb.2009.04.005 (2009).

52 Houseman, E. & Jakubovics, J. Electron microscope study of the domain structure of MnAlC magnets. *Journal of Magnetism and Magnetic Materials* **31**, 1007-1008 (1983).

53 Saito, T. Magnetic properties of Mn–Al system alloys produced by mechanical alloying. *Journal of Applied Physics* **93**, 8686, doi:10.1063/1.1544526 (2003).

54 Yan, Z. C., Huang, Y., Zhang, Y., Hadjipanayis, G. C., Soffa, W. & Weller, D. Magnetic and structural properties of MnAl/Ag granular thin films with $L1_0$ structure. *Scripta Materialia* **53**, 463-468, doi:10.1016/j.scriptamat.2005.04.045 (2005).

55 <Effect of magnetic annealing on the τ-phase of MnAl thin films.pdf>.

56 <Ferromagnetic τ-MnAl epitaxially grown on (100) GaAs substrates by pulsed laser deposition.pdf>.

57 Fazakas, E., Varga, L. K. & Mazaleyrat, F. Preparation of nanocrystalline Mn–Al–C magnets by melt spinning and subsequent heat treatments. *Journal of Alloys and Compounds* **434-435**, 611-613, doi:10.1016/j.jallcom.2006.08.313 (2007).

58 Lee, J.-G., Li, P., Choi, C.-J. & Dong, X.-L. Synthesis of Mn–Al alloy nanoparticles by plasma arc discharge. *Thin Solid Films* **519**, 81-85, doi:10.1016/j.tsf.2010.07.063 (2010).

59 Pareti, L., Bolzoni, F., Leccabue, F. & Ermakov, A. Magnetic anisotropy of MnAl and MnAlC permanent magnet materials. *Journal of Applied Physics* **59**, 3824-3828 (1986).

60 Berkowitz, A. E., Livingston, J. D. & Walter, J. L. Properties of Mn-Al-C magnets prepared by spark erosion and other rapid solidification techniques. *Journal of Applied Physics* **55**, 2106, doi:10.1063/1.333579 (1984).

61 Zeng, Q., Baker, I., Cui, J. & Yan, Z. Structural and magnetic properties of nanostructured Mn–Al–C magnetic materials. *Journal of Magnetism and Magnetic Materials* **308**, 214-226 (2007).

62 Yang, Y. c., Ho, W. w., Lin, C., Yang, J. l., Zhou, H. m., Zhu, J. x., Zeng, X. x., Zhang, B. s. & Jin, L. Neutron diffraction study of hard magnetic alloy MnAlC. *Journal of Applied Physics* **55**, 2053-2054 (1984).

63 Liu, Z., Chen, C., Zheng, Z., Tan, B. & Ramanujan, R. V. Phase transitions and hard magnetic properties for rapidly solidified MnAl alloys doped with C, B, and rare earth elements. *Journal of Materials Science* **47**, 2333-2338 (2012).

64 Prost, T. E. Magnetic Properties Study of the Mn-Al System with Additions of B or C and Mechanical Milling Techniques. (2012).

65 Sakka, Y., Nakamura, M. & Hoshimoto, K. Rapid quenching and properties of hard magnetic materials in MnAl-X (X= Ti, Cu, Ni, C, B) systems. *Journal of Materials Science* **24**, 4331-4338 (1989).

66 Wang, H., Si, P., Jiang, W., Lee, J., Choi, C., Liu, J., Wu, Q., Zhong, M. & Ge, H. Structural Stabilizing Effect of Zn Substitution on MnAl and Its Magnetic Properties. *Open Journal of Microphysics* **1**, 19 (2011).

67 H. X. Wang, P. Z. S., W. Jiang, X. F. Xiao, J. G. Lee, C. J. Choi, M. Zhong, Z. F. Li and H. L. Ge. Structure and Magnetic Properties of Cu Doped MnAl. *Physical Science International Journal* **4**, 5, doi:10.9734/PSIJ/2014/5326 (2014).

68 Chaturvedi, A., Yaqub, R. & Baker, I. A comparison of τ-MnAl particulates produced via different routes. *Journal of Physics: Condensed Matter* **26**, 064201 (2014).

69 Lucis, M. J., Prost, T. E., Jiang, X., Wang, M. & Shield, J. E. Phase Transitions in Mechanically Milled Mn-Al-C Permanent Magnets. *Metals* **4**, 130-140 (2014).

Chapter 2 Theoretical Aspects

In this chapter, fundamentals of magnetism are introduced, including the origin of magnetism, magnetic anisotropy, domain and domain walls, and magnetization reversal mechanism. Then the effects of microstructure on magnetic property are investigated. Lastly, the fundamentals of phase transformations are discussed. These theoretical concepts help to understand the fabrication and structural and magnetic characterization of $L1_0$-structured permanent magnetic materials.

2. 1 Magnetism

2. 1. 1 Origin of Magnetism

Magnetism is a force of attraction or repulsion acting at a distance, which is caused by a magnetic field. The magnetic field originates from electric current or magnetic moments of elementary particles. The electric current could be an electric current in a circular conductor or the motion of an orbiting electron in an atom, both of which create a magnetic dipole moment. The magnetic moments of elementary particles are from the intrinsic spinning of electrons, photons and neutrons[1].

In all materials, the atomic masses are from the atomic nucleus, while the electrical, chemical and magnetic properties are determined by the electronic structure, which surrounds the nucleus. Electrons are distributed in specific shells at definite distances from the nucleus, which is due to the different energy level in each shell. In the ferromagnetic elements, including α-Fe, Co, Ni and Gd, there are three important features:

1) There must be an unfilled inner electron shell within the atom.

2) There must be uncompensated electronic spins in the unfilled inner shell.

3) The atoms must form a crystal lattice having a lattice constant at least 3 times the radius of the unfilled electron shell.

The electrons in the shells have two types of motion, as they both orbit around the nucleus and spin on their own axis, which will give rise to the magnetic moments. It is in unfilled shells that the spin moments are not compensated. In crystals when the ratio of the crystal spacing to the radius of the unfilled 3d shell exceeds 3 (in transition metals), parallel alignment of the electrons caused by the interaction between the atoms or the ions of the crystal lattice is possible.

Macroscopic magnetic properties of materials are a consequence of magnetic moments associated with individual electrons, which is the sum of spin moment and orbital moment. Depending on the magnetic ordering and the sign, magnitude and temperature dependence of the magnetic susceptibility, the magnetic materials are classified into diamagnetic, paramagnetic, ferromagnetic, antiferromagnetic and ferrimagnetic materials. The magnetic susceptibility χ is a dimensionless proportionality constant that indicates the degree of magnetization of a material in response to an applied magnetic field, and is given by[2]

$$\chi = M/H \tag{2.1}$$

where χ is the magnetic susceptibility, M is the magnetization of the material, and H is the applied field[3].

In diamagnetic materials, the magnetic susceptibility is negative and on the order of -10^{-6} to -10^{-5}. The applied magnetic field would induce an extremely small magnetization in the opposite direction to that of the applied field. This is due to complete cancellation of the electronic motion (orbiting and spinning). Thus, the intrinsic magnetic moment of all the atoms is zero and diamagnetic materials are weakly affected by magnetic field. Diamagnetic susceptibility is independent of temperature.

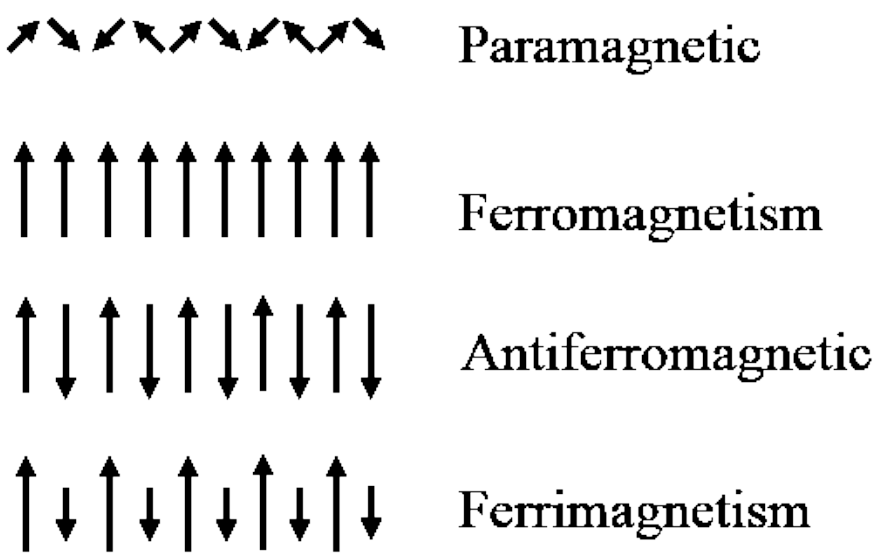

Figure 2.1 Schematic illustration of various types of magnetism

Paramagnetic materials (Figure 2.1) have a positive magnetic susceptibility in the range of 10^{-4} to 10^{-5}. Paramagnetic properties are due to the presence of some unpaired electrons, and results from the realignment of the electron paths caused by the external magnetic field. An applied magnetic field will align the magnetic moments in the field direction which are otherwise random due to thermal agitation. As the temperature increases, the thermal agitation will increase and it will be more difficult to align the

atomic magnetic moments. Thus, there is a strong dependence on temperature for paramagnetic materials.

The characteristic feature of ferromagnetism is its spontaneous magnetization, which is due to alignment of the magnetic moments. The magnetization tends to lie along easy directions determined by crystal structure, atomic-scale texture or sample shape[2]. In quantum mechanics, the Heisenberg model of ferromagnetism describes the parallel alignment of the magnetic moments in terms of an exchange interaction between neighboring moments[3]. If two atoms *i* and *j* have spin angular momentum $S_i h/2\pi$ and $S_j h/2\pi$, respectively, the exchange energy between them is given by

$$E_{ex} = -2J_{ex}S_iS_j = -2JS_iS_j \cos\varphi \qquad (2.2)$$

where J_{ex} is the exchange integral, which occurs in the calculation of the exchange effect, and φ is the angle between the spins. If J_{ex} is positive, E_{ex} is a minimum when the spins are parallel ($\cos\varphi = 1$) and a maximum ($\cos\varphi = -1$) when they are antiparallel. If J_{ex} is negative, the lowest energy state results from antiparallel spins. Since ferromagnetism is due to the alignment of spin moments of adjacent atoms, a positive value of the exchange integral is therefore a necessary condition for ferromagnetism to occur[3].

Ferromagnetic materials are compared in terms of saturation magnetization rather than susceptibility. Saturation magnetization, M_s, is the magnetization when all the magnetic moments are aligned with the external field. Ferromagnetic materials obey the Curie –Weiss law as the temperature increases, thermal agitation of the atoms would decrease the magnetization (Figure 2.2). Above the Curie temperature, the magnetization would decrease to zero. At room temperature, Fe, Co, Ni and rare earth element Gd are the only ferromagnetic elements.

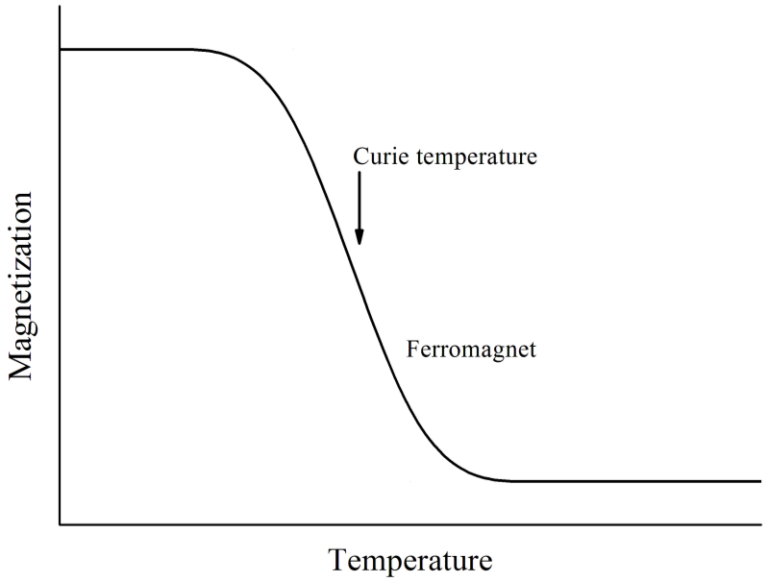

Figure 2.2 Schematic illustration of Magnetization vs Temperature curve

Antiferromagnetic materials are similar to ferromagnetic materials, but the exchange interaction between neighboring atoms leads to an anti-parallel alignment of the atomic magnetic moments. Therefore, the net magnetization of antiferromagnetic materials is zero. A transition from antiferromagnetism to paramagnetism occurs at the Neèl temperature. At room temperature, chromium is the only antiferromagnetic element.

Ferrimagnetism exists only in compounds, within which the exchange interactions lead to parallel alignment of atoms in some of the crystal sites and antiparallel alignment of others. Lower magnetization is observed due to the cancellation of magnetic moments between the parallel aligned atoms and the antiparallel aligned ones. Ferrites are typical ferrimagnetic materials. In $BaO.6Fe_2O_3$, 2/3 of the Fe^{3+} ions have moments aligned parallel while the other 1/3 aligned antiparallel giving a net magnetization parallel to the applied field. Since only 1/3 of the ions contribute to the net magnetization, lower magnetization is obtained.

2. 1. 2 Hysteresis loop

Hysteresis loops provide specific information about the magnetic performance of magnetic materials because they show the relationship between the induced magnetization and the applied field as shown in Figure 2.3. The M-H hysteresis loop is generated by measuring the magnetization of ferromagnetic materials while the applied magnetic field is changed. When all the magnetic moments are aligned with the applied field, the saturation magnetization (M_s) is obtained. With the applied field decreasing to zero, the ferromagnetic material retains a considerable degree of magnetization, namely remanence (M_r). As the applied field is reversed, the applied field needed to reduce the magnetization to zero is the intrinsic coercivity (H_{ci}). Further increase of the applied field in the negative direction will saturate the materials magnetically in the opposite direction. B-H (B is induced magnetic flux density, H is the applied field) hysteresis loop could be calculated from the M-H loop by the following expressions.

$$B = 4\pi M + H \text{ (cgs unit system)} \quad (2.3)$$

$$B = \mu_0(M + H) \text{ (SI unit system)} \quad (2.4)$$

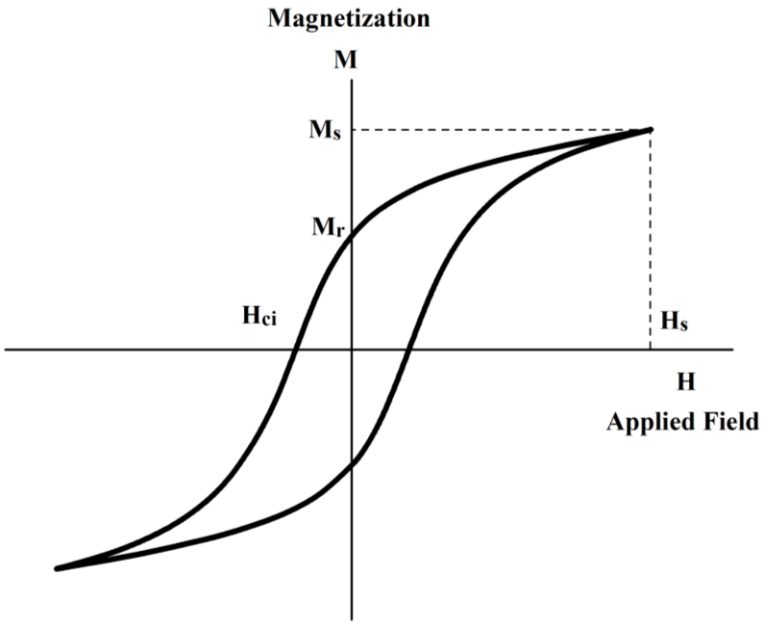

Figure 2.3 M-H hysteresis loop (M is induced magnetization, H is the applied field)

According to the hysteric behavior of the ferromagnetic materials, they are divided into three types in terms of coercivity. When the coercivity is less than 12.6 Oe, it's defined as soft magnets. When the coercivity is larger than 2.5 kOe, it's considered as hard magnets or permanent magnets. Semi-hard magnets are materials, whose coercivity is between 12.6 Oe and 2.5 kOe. The performance of permanent magnetic materials is evaluated by the energy product, the product of H and B on the B-H demagnetization (second quadrant) curve. Maximum energy product, $(BH)_{max}$, shows a yardstick for the maximum amount of magnetic flux taken out from the magnet per unit volume. Higher $(BH)_{max}$ is preferred for permanent magnetic materials.

2. 2 Magnetic anisotropy

Magnetic anisotropy is defined as the directional dependence of the magnetic properties for materials. Specifically, the preferential direction for its magnetic moment

in the absence of an applied magnetic field. Strong easy-axis anisotropy is a prerequisite for hard magnetism, while near-zero anisotropy is desirable for soft magnets. Generally, the tendency for magnetization to lie along an easy axis is represented by the energy density term

$$E_a = K_1 sin^2\theta \tag{2.5}$$

where θ is the angle between the magnetic field and the anisotropy axis, and K_1 is the anisotropy constant, which ranges from ~1 kJ/m^3 to more than 20 MJ/m^3. There are several sources of magnetic anisotropy[2]:

- Magnetocrystalline anisotropy: intrinsic property due mainly to spin-orbit coupling;
- Shape anisotropy: induced by the nonspherical shape of the grains;
- Stress anisotropy: created by applied mechanical stress due to the existence of magnetostriction, which could alter the domain structure;
- Exchange anisotropy: occurs when the interaction between antiferromagnet and a ferromagnet occurs at their interface;
- Anisotropy induced by grain alignment and stress through magnetic annealing, irradiation, and plastic deformation:
  - Magnetic annealing: thermomagnetic treatment (heat treatment in a magnetic field) could introduce anisotropy in certain alloys;
  - Irradiation: when the materials are irradiated by neutron at high temperature in a magnetic field, the direction irradiated will become an easy axis;

- Plastic deformation: plastic tension/compression would cause the specimen volume in tension/compression parallel to the deformation axis, which is the preferred axis to magnetize.

2. 2. 1 Magnetocrystalline anisotropy

The magnetocrystalline anisotropy primarily arises from spin-orbit coupling. When an external field tries to reorient the spin of an electron, the orbit of that electron also tends to be reoriented. But the orbit is strongly coupled to the lattice and therefore resists the attempt to rotate the spin axis. The energy required to rotate the spin system of a domain away from the easy direction, anisotropy energy, is the energy required to overcome the spin-orbit coupling. The strength of the magnetocrystalline anisotropy in any particular crystal is measured by the magnitude of the anisotropy constant K_1, K_2, etc. $L1_0$ structure in this research is in tetragonal symmetry, conventional expression for the anisotropy energy in tetragonal symmetry is:

$$E_a = K_1 sin^2\theta + K_2 sin^4\theta + K_2' sin^4\theta cos4\varphi \ + K_3 sin^6\theta + K_3' sin^6\theta sin6\varphi \qquad (2.6)$$

where K_i are the anisotropy constants, α_i are the direction cosines of the magnetization, θ is the angle between the magnetic field and the anisotropy axis, φ is the angle between the magnetization and the field.

The magnitude of the magnetocrystalline anisotropy generally decreases with temperature more rapidly than the magnetization vanishes at the Curie temperature. Since the anisotropy contributes strongly to the coercive field, it has a great influence on industrial uses of ferromagnetic materials. Materials with high magnetic anisotropy usually have high coercivity; that is they are hard to demagnetize. The high anisotropy

of rare earth metals is mainly responsible for the strength of rare earth magnets, which are widely used in permanent magnets.

2. 3 Domain theory

Domain theory postulates the existence of large regions of uniform magnetization in a macroscopic sample, which are separated by planar regions, the domain walls, where the magnetization rotates from one easy direction to another[4]. So the magnetic domain is a region with uniform magnetization in a magnetic material. The magnetic domain structure is responsible for the magnetic behavior of ferromagnetic materials. When an applied field is applied to the sample, the net magnetization would change either by causing the walls to move or by making the magnetization in the domains rotate towards the applied field direction.

2. 3. 1 Domain structure

In magnetic materials, contributions to the overall energy include magnetostatic energy, magnetic anisotropy energy, exchange energy and Zeeman energy[5]. In magnetic particles (shown in Figure 2.4a), surface charges form on both ends due to the uniform magnetization giving rise to magnetostatic energy. This energy is the volume integral of the field over all space. The magnetostatic energy can be minimized by the splitting of single domain into two domains with magnetization in opposite directions (Figure 2.4b). Further reduction in magnetostatic energy could be achieved by smaller parallel domains with magnetization in alternating directions (Figure 2.4c). Meanwhile, when the domain splits each time, a domain wall is created between the new domains. The domain wall

energy is proportional to the area of the wall. Thus, the minimum domain size is obtained when the net energy, magnetostatic energy and domain wall energy, are minimized.

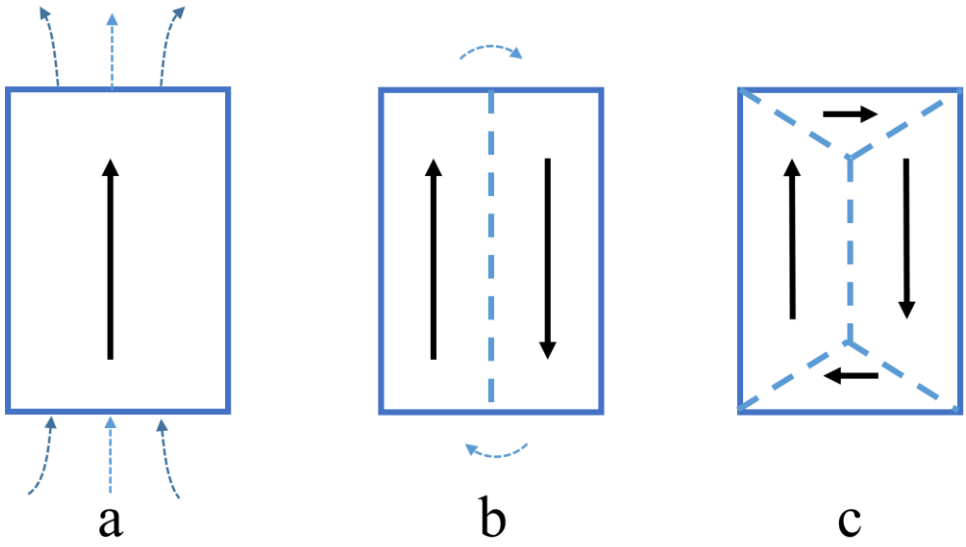

Figure 2.4 Splitting of single domain into smaller domains with magnetization in alternating directions (side view)

2. 3. 2 Domain Walls

Domain walls are interfaces between regions in which the spontaneous magnetization has different directions. It's a transition of magnetization directions from one easy crystallographic direction to another, and undergoes an angular displacement of 90 °or 180 °. Two types of domain walls are observed: Bloch wall and Neel wall. In Bloch wall, the magnetization rotates through the plane of the domain wall, while, in Neel wall, the magnetization rotates within the plane of the domain wall as shown in Figure 2.5. Bloch wall is the commonest, and it creates no divergence of magnetization in the wall. When the thickness of the sample becomes comparable to the thickness of the

domain wall, the energy associated with the free poles that arise where a Bloch wall meets the surface becomes significant. This leads to a change in the wall structure from Bloch wall to Neel wall, with magnetization rotating in the plane of the sample rather than in the plane of the wall.

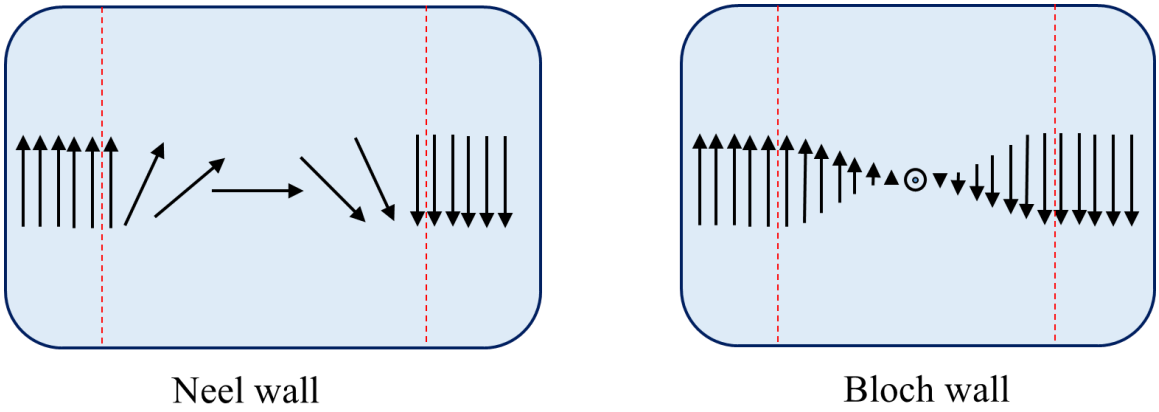

Figure 2.5 Schematic domain structures (Bloch wall and Neel wall)

The wall energy is calculated by the sum of the exchange and anisotropy energies, integrated over the thickness of the wall $\delta = 4\sqrt{AK_1}$ for 180 °wall and $\delta = 2\sqrt{AK_1}$ for 90 °wall, whereas A is the exchange stiffness or the exchange constant, and K_1 is the anisotropy constant. The thickness of domain wall can be obtained from $d = \pi\sqrt{A/K_1}$. The domain wall thickness is generally in the range of 0.1~100 nm. Table 2.1 shows some typical domain wall thickness of selected magnetic materials[6].

Table 2.1 Domain wall thickness of selected magnetic materials[6]

Magnetic material	Domain wall width (nm)
Co	14
$Nd_2Fe_{14}B$	3.9
$Sm_2Fe_{17}N_3$	3.6
FePt	6.3
FePd	11.5
Sm_2Co_{17}	8.6
$Sm(TiFe_{11})$	4
$SmCo_5$	3.6
CoPt	7.4

2. 4 Magnetization reversal

When a reverse magnetic field is applied to the initially magnetized material, the material can reverse its magnetization via several mechanisms depending on the magnitude of the magnetocrystalline anisotropy. For the materials with low magnetocrystalline anisotropy, magnetization reversal could be achieved by coherent rotation of all the atomic moments, non-coherent rotation modes such as fanning, curling, and buckling[7]. However, when there is high magnetocrystalline anisotropy in the material, the magnetization reversal is mainly through domain wall motion. In this study, high magnetocrystalline anisotropy is required in $L1_0$ structure materials, so magnetization reversal through domain wall motion is of great concern.

The magnetic materials reversed by domain wall motion can be divided into two hysteretic behavior categories: pinning and nucleation[8]. When high-volume concentration

and uniform spatial distribution of the defects interact with the domain walls, the wall motion will be accompanied by a constant pinning strength, which determines the intrinsic coercivity of the magnet. The characteristic features of the hysteretic behavior of pinning-controlled magnets are low initial susceptibility, horizontal recoil curves, and stepped field dependence of intrinsic coercivity. In magnetic material with a low-volume concentration of magnetoactive defects within the grains, ease of grain through domain wall motion will be caused by nucleation.

2. 4. 1 Nucleation

In homogeneous materials without obstacle to domain wall motion, the coercivity (H_c) is expressed by the following equation[9-11];

$$H_c = \frac{2K_1}{M_s} - NM_s \tag{2.7}$$

where K_1 is the magnetocrystalline anisotropy, M_s is the saturation magnetization and N is the demagnetization factor due to the local stray field. However, the experimentally obtained coercivity is much lower than the theoretically predicted coercivity value. This discrepancy is due to the existence of regions of reduced anisotropy inside the magnetic material which act as the nucleation sites for the reversed domains at relatively lower applied fields. These regions include inhomogeneities which can have either the form of grain boundaries, granular inclusions and lamellar precipitates which help to reduce the local anisotropy[12], or small changes in lattice parameters due to deviations in stoichiometric compositions which result in large changes in anisotropy[13], or lattice imperfections such as lattice disorders, point defects or dislocations[14]. To achieve a better

agreement with the experimental coercivity value, modification on this model was made[15,16],

$$H_c = \alpha_\varphi \alpha_k \frac{2K_1}{M_s} - NM_s \tag{2.8}$$

where α_φ and α_k denote the reductions of the anisotropy factors due to microstructural inhomogeneity and grain misalignment respectively.

2. 4. 2 Pinning

After nucleation of a reverse domain, the external field exerts a driving force for domain wall motion. The wall motion is hindered by structural defects, such as voids, point defects, dislocations, second phases and antiphase boundaries, as effective pinning centers, which depend on two factors:

1) The scale of the domain wall thickness must be similar to the size of defects or the precipitate.
2) The magnetocrystalline anisotropy of the material must be different with that of the defect or the precipitate, and highest coercivity could be reached when the anisotropy gradient between the defects/precipitates and the matrix is maximum.

Point defects, with sufficient defect density, can act as pinning centers by changing the exchange interaction and the magnetocrystalline anisotropy locally[17]. Antiphase boundaries, a surface or interface between two halves of an ordered crystal structure, were discovered to be another important type of pinning center in FePt[18] and MnAl[19,20]. It is due to the low local magnetocrystalline anisotropy at the boundaries[21].

The pinning effect of residual stress is closely related to this research, so it's discussed separately in the following part.

2. 4. 2. 1 Residual stress

Another kind of hindrance to domain wall motion is residual microstress. It exists in the forms of dislocations and magnetostriction in materials.

1. Since the dislocations distort the surrounding materials, stress field is always associated with dislocations. A complex network of irregular distribution of microstress could be generated by dislocations in different directions, and interaction of dislocations with moving domain walls would impede the wall motion.
2. When ferro- or ferrimagnetic materials are cooled below the Curie temperature, spontaneous magnetostriction acts to distort the magnetic domains in different directions, causing microstresses. They are large enough to cause interactions between domain, domain walls and crystal imperfections.

The effect of residual microstress on 90 °walls and 180 °walls is different. When a 90 °wall moves, the direction of magnetization is altered in the volume swept out by the wall motion, and elastic distortion occurs. The distortion interacts with the local stress distribution in a way that tends to keep the domain wall in its original position. In the 180 ° wall motion, only the sense of the magnetization direction is altered, and no magnetostrictive strain occurs. The effect of local microstress is to change the domain wall energy by adding a stress anisotropy to the crystal anisotropy *K*.

Effect of microstress distribution on the domain wall motion is difficult to calculate though. The actual microscopic stress distribution in materials is unknown, and isolated domain walls don't exist in real materials. Furthermore, domains are in an interconnected network in magnetic materials, and no single wall can move without influencing the position of its connected walls.

2. 5 Phase transformation

The phase of alloys with desired crystalline structure, rather than just the composition, is another important aspect to be considered in determining their magnetic properties. Phase transformations are typically divided into either diffusional or displacive transformations, although subcategories within each also exist [22]. Diffusional transformations occur when the chemical composition changes with the transformation process. Diffusion of atoms over relatively long distances (up to several μm[23]) is required, so the transformation is dependent on temperature and time. Since there are two common atomistic mechanisms in crystal, by which atoms can diffuse through a solid, and the operative mechanism depends on the type of site occupied in the lattice. Substitutional diffusion is based on a vacancy mechanism, while interstitial diffusion is by forcing the atoms diffuse in the interstitial sites between larger atoms. In substitutional diffusion, the diffusion rate is sensitive to the vacancy concentrations and temperature, which offers sufficient vibrational energy for atomic jumps. Displacive transformations do not change the composition of the parent phase, but rather the crystal structure. Thus, long-range atomic movement is not required, while the new phase is formed through slight atomic shuffles of generally less than an atomic diameter and atoms are cooperatively rearranged

into a new, more stable crystal structure with the same chemical composition as the parent phase. Therefore, a displacive transformation is a time-independent process. The transformation speed of the interface between two phases is nearly the speed of sound in most alloys.

The disorder-order transformation from fcc structure to $L1_0$ structure is a representative diffusional transformation[24]; therefore, the transformation is sensitive to the vacancy concentration and the temperature. The diffusion of lattice atoms by way of the vacancy mechanism is given by

$$D_a^v = f_v D_v C_v \tag{2.9}$$

where, D_v is the vacancy diffusion coefficient, C_v is the vacancy concentration and f_v is the correlation coefficient[25]. Thus, increasing the concentration of vacancies will enhance the diffusion coefficient of Ni atoms in FeNi alloy, accelerating the phase transformation process.

References

1 Heck, C. *Magnetic materials and their applications*. (Butterworths, 1974).

2 Coey, J. M. *Magnetism and magnetic materials*. (Cambridge University Press, 2010).

3 Cullity, B. D. & Graham, C. D. *Introduction to magnetic materials*. (John Wiley & Sons, 2011).

4 Kittel, C. Physical theory of ferromagnetic domains. *Reviews of Modern Physics* **21**, 541 (1949).

5 Feynman, R. P., Leighton, R. B. & Sands, M. The Feynman lectures on physics: Mainly mechanics, radiation, and heat (Vol. 1). *IAddison-Wesley Publishing Company, Menlo Park, California*, 2 (1963).

6 Herlach, F. & Miura, N. *High magnetic fields: science and technology*. Vol. 3 (World Scientific, 2006).

7 Cahn, R. W. & Haasen, P. *Physical metallurgy. Vol. 1*. (North-Holland, 1996).

8 Gabay, A., Lileev, A. & Menushenkov, V. *Hysteretic Behavior of Nucleation-controlled Magnets*. (CRC Press, 2001).

9 Brown Jr, W. F. Relaxational behavior of fine magnetic particles. *Journal of Applied Physics* **30**, S130-S132 (1959).

10 Brown Jr, W. F. Virtues and weaknesses of the domain concept. *Reviews of Modern Physics* **17**, 15 (1945).

11 Aharoni, A. Theoretical search for domain nucleation. *Reviews of Modern Physics* **34**, 227 (1962).

12 Goodenough, J. B. A theory of domain creation and coercive force in polycrystalline ferromagnetics. *Physical Review* **95**, 917 (1954).

13 Deryagin, A. 3d-4f METALLIC COMPOUNDS. Magnetic moment, magnetic anisotropy and spin-reorientation phase transition in (4f-3d)-intermetallic compounds. *Le Journal de Physique Colloques* **40**, C5-165-C165-170 (1979).

14 Ramesh, R. A microstructure based magnetization reversal model in sintered Fe-Nd-B magnets. I. *Journal of Applied Physics* **68**, 5767-5771 (1990).

15 Kronmüller, H. Theory of nucleation fields in inhomogeneous ferromagnets. *physica status solidi (b)* **144**, 385-396 (1987).

16 Kronmüller, H., Durst, K.-D. & Sagawa, M. Analysis of the magnetic hardening mechanism in RE-FeB permanent magnets. *Journal of Magnetism and Magnetic Materials* **74**, 291-302 (1988).

17 Kronmüller, H. & Hilzinger, H. The coercive field of hard magnetic minerals. *Int. J. Magn* **5**, 27-30 (1973).

18 VOLKOV, A. & ROMANOV, A. MEETING OF THE DAVIDENKOV SECTION OF STRENGTH AND DUCTILITY OF MATERIALS OF THE GORKY HOUSE OF SCIENTISTS AT LENINGRAD ON THE THEME: THE ROLE OF ROTATIONAL CHANNELS OF DUCTILITY IN THE STRENGTH PROBLEM. *The Physics of Metals and Metallography* **64** (1987).

19 Chen, X. & Gaunt, P. The pinning force between a Bloch wall and a planar pinning site in MnAlC. *Journal of Applied Physics* **67**, 2540-2543 (1990).

20 Hoydick, D., Palmiere, E. & Soffa, W. On the formation of the metastable Ll< sub> o</sub> phase in manganese-aluminum-base permanent magnet materials. *Scripta Materialia* **36**, 151-156 (1997).

21 Young, A. & Jakubovics, J. The effect of planar defects on exchange interactions in ferromagnetic metals. *Journal of Physics F: Metal Physics* **5**, 1866 (1975).

22 Porter, D. A. & Easterling, K. E. *Phase Transformations in Metals and Alloys, (Revised Reprint)*. (CRC press, 1992).

23 Sha, W. & Malinov, S. *Titanium alloys: Modelling of microstructure, properties and applications*. (Elsevier, 2009).

24 Farjami, S., Fukuda, T. & Kakeshita, T. in *Journal of Physics: Conference Series.* 012055 (IOP Publishing).

25 Was, G. S. *Fundamentals of radiation materials science*. (Springer, 2007).

Chapter 3 Experimental Techniques

This chapter will cover the fundamental principles and functions of various techniques utilized in this study. It mainly focuses on two aspects: sample preparation and sample characterization. In the sample preparation part, the techniques include arc melting, melt spinning, mechanical milling/alloying, and heat treatment. The sample characterization methods are x-ray diffraction (XRD), Transmission Electron microscopy (TEM), Scanning Electron Microscopy (SEM), Positron Annihilation Spectroscopy (PAS), Vibrating Sample Magnetometry (VSM), Superconducting Quantum Interference Device (SQUID) magnetometry, and Differential Thermal Analysis (DTA).

3. 1 Sample preparation

3. 1. 1 Arc melting

Arc melting is used to produce alloys from elemental constituents. As shown in the schematic illustration of the arc-melter (Figure 3.1), there are 4 main parts in the arc-melter: vacuum chamber, power supply, melting electrode with water-cooling system, and copper hearth with water-cooling system. The power supply provides firstly, high electrical voltage (low current) in order to initiate the electrical breakdown in the gaseous atmosphere between the electrode and the copper hearth and, secondly, high current power for the subsequent melting process[1]. Electricity passes through the metals, which heats them to melting point. The temperature of the electric arc mostly depends on two factors, the type of gas and the chamber pressure. By controlling the composition of the

gas and the pressure in the chamber, the arc's heat can be altered to fit different applications.

In our arc-melting system, DC power (Synchowave 180 SD, Miller Electric) is utilized to provide a squarewave power. The output could reach as high as 180 Amps with operating mode at TIG position under an electrode positive polarity. A tungsten tip, held in place with a copper sleeve and fastener, was used as electrode, since the melting temperature of tungsten is as high as 3422℃, which is the perfect material for conducting the current. It melts at higher temperature than most alloys, especially all alloys used in this study. The chamber is evacuated and backfilled with ultra-high purity (UHP) Ar to avoid oxidization.

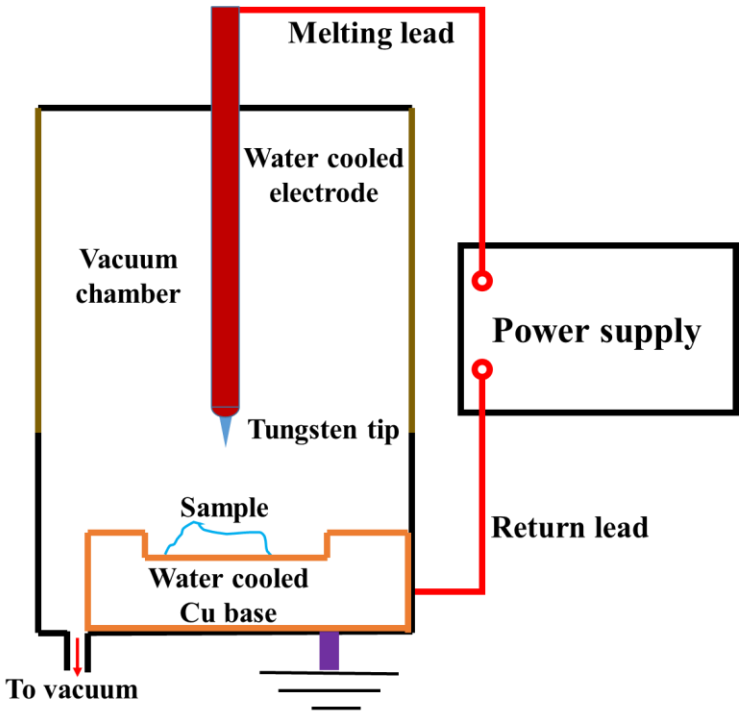

Figure 3.1 Schematic illustration of arc-melter

In the experiment, high purity elements including Fe (99.97%), Ni (99.99%), Zr (99.8%), B (99.5%), Mn (99.9%), Al (99.999%), C (99.97%), Hf (99.9%) (from Alfa Aesar) were used as the raw materials. A micro-balance (SARTORIUS) with an error of ±0.2 mg was used to weigh the raw materials. The smaller pieces (mainly Boron) were placed underneath the larger pieces to prevent them from shifting under the power of the arc. To ensure the homogeneity, the ingot were flipped over at least 2 times and remelted.

3. 1. 2 Melt spinning

Rapid solidification can be achieved through melt spinning process Rapid solidification can result in higher solubility of alloyed elements in solid solutions, especially important for alloys with elements that have a small solubility in equilibrium state[2,3]. Meanwhile, it can cause increased chemical homogeneity, refined grain size and formation of metastable phases[4]. Thus, it's been widely applied in producing amorphous metallic glass and nanocrystalline materials.

As shown in Figure 3.2, the ingot obtained from arc melting is placed into a quartz crucible. High-frequency induction melting was utilized to melt the alloy. An argon over-pressure was then used to eject the molten alloy through the orifice on the high speed spinning wheel. The cooling rates are on the order of 10^4~10^7 K/s corresponding to the wheel speed ranging from 5~60 m/s. As a result, a continuous ribbon is obtained. The thickness of the ribbon (20~100 μm) is a function of the injection pressure, the gap between the nozzle and the wheel, and the cooling rate. In this research, the orifice diameter is 0.5 mm, and the distance between the orifice and the wheel is 5

mm. The chamber is filled with UHP Ar at the pressure of ~900 mbar during experiment. The wheel speed used in this research is 40 m/s for both FeNi and MnAl alloys.

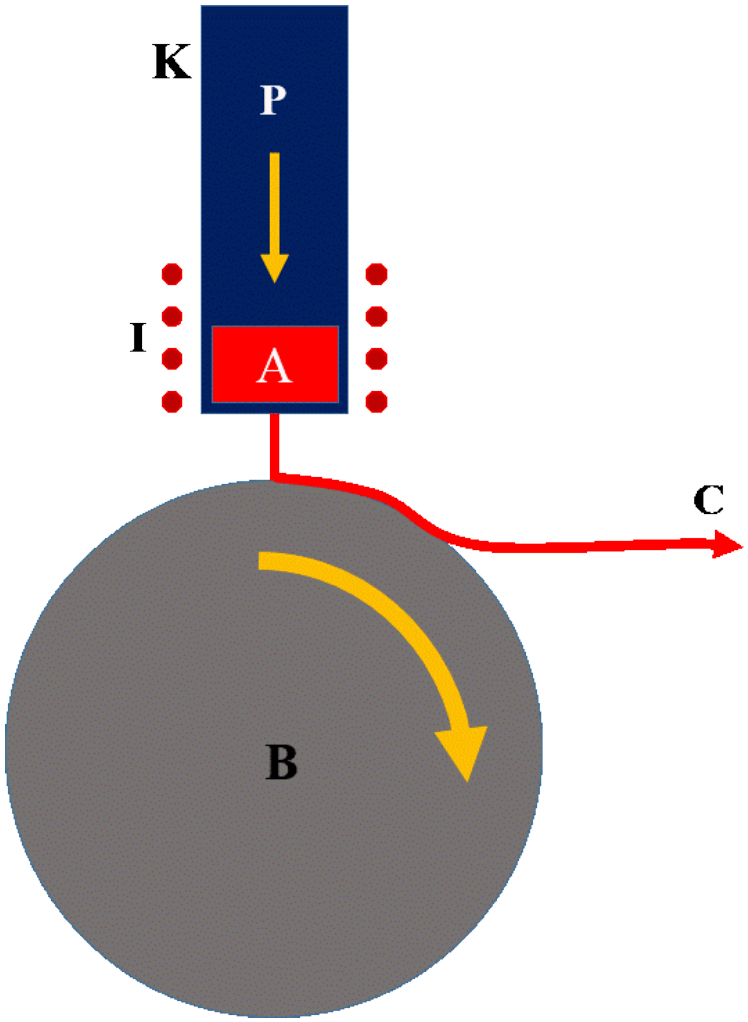

Figure 3.2 The metal (A) is melted by induction coils (I) and pushed by gas pressure (P), in a jet through a small orifice in the crucible (K) over the spinning drum (B) where is rapidly cooled to form the ribbon of amorphous material (C)

3. 1. 3 Mechanical milling

Mechanical milling is a process which is routinely used in powder metallurgy and mineral processing industries. The typical objectives of the milling process include

particle size reduction (comminution), solid-state alloying, mixing or blending, and particle shape changes. Nowadays, mechanical milling could be used to produce different types of materials, including amorphous alloy powders, nanocrystalline powders, intermetallic powders, composite and nanocomposite powders, and nanopowders.

SPEX 8000M Mixer/Mill, as shown in Figure 3.3 (a), is most commonly used for laboratory investigation purposes. The common variety of the mill has one vial (Figure 3.3 (b)) containing the sample and grinding balls secured in the clamp and moves energetically back and forth several thousand times a minute. High-energy milling forces can be obtained using high frequencies and small amplitudes of vibration. Since the kinetic energy of the balls is a function of their mass and velocity, dense materials (harden steel or tungsten carbide) are preferable to ceramic balls.

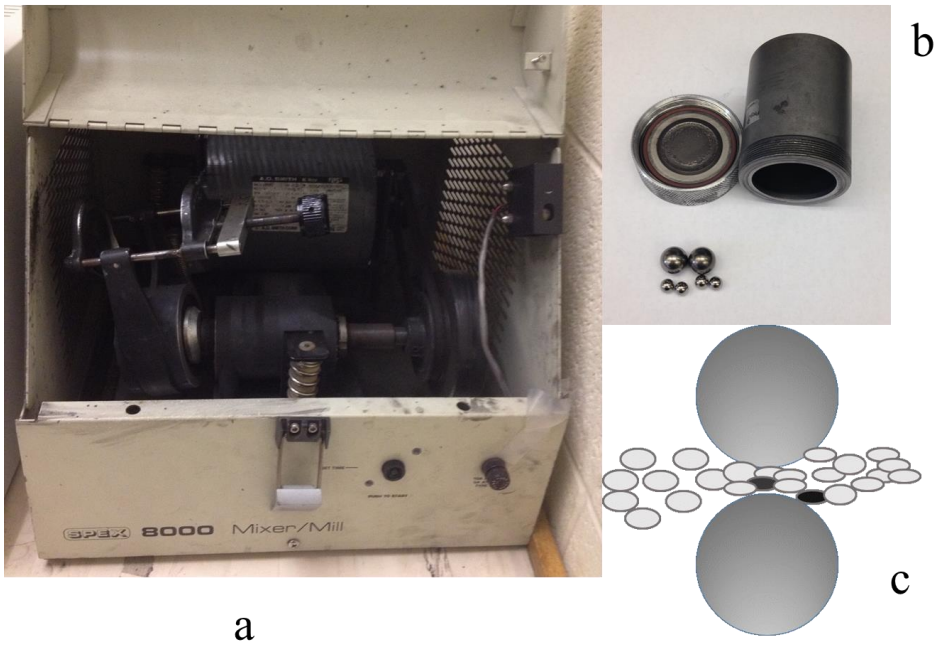

Figure 3.3 (a) A typical high energy ball mill from SPEX-8000M Mixer/Mill; (b) Hardened steel vial and grinding media; (c) Schematic representation of the principle of mechanical milling

As shown in Figure 3.3 (c), when two balls collide, some amount of powder will be trapped in between them. The force of impact plastically deforms the powder particles, leading to work hardening and fracture. The new surfaces created enable the particles to weld together, introducing a possible increase in particle size. The composite particles at this stage have a characteristic layered structure, consisting of various combinations of the starting constituents. With continued deformation, the particles get work hardened and fracture by a fatigue failure mechanism and/or by the fragmentation of fragile flakes. Fragments generated by this mechanism may continue to reduce in size in the absence of strong agglomerating forces. The tendency to fracture predominates over cold welding at

this stage. Further milling would refine the structure of the particles steadily, but the particle size would not be decreased[5].

Mechanical milling process is controlled by various processing parameters, critically impacting the phase or microstructure[6]. These parameters include types of mills, the composition of the jar and balls, the milling speed, the milling time, the ball-to-sample ratio, the milling media, and the milling atmosphere. In this research, we mainly focus on the milling time, the ball-to-sample ratio and the milling media.

The milling time is the most important parameter. Normally the time is so chosen as to achieve a steady state between the fracturing and cold welding of the powder. The time required varies depending on the type of mill, the intensity of milling, the ball-to-powder ratio, and the temperature of milling. However, the contamination increases with the milling time, and some undesired phases form with longer milling time than required[7]. Therefore, controlling the milling time is the key to get the desired powder.

The ratio of the weight of the balls to the powder (BPR) has a significant effect on the time required to achieve a particular phase in the powder being milled. The ratio can vary from 1:1[8] to as high as 220:1[9] for different research. A ratio of around 10:1 is most commonly used while milling the powder in a small capacity mill such as a SPEX. Normally the higher the BPR, the shorter is the time required. It has been demonstrated in a Ti-33 at.% Al powder mixture, formation of an amorphous phase was achieved in 7 h at a BPR of 10:1, in 2 h at a BPR of 50:1 in a SPEX mill[10]. It has been proposed that an increase in the BPR could increase the number of collisions per unit time, and consequently transfer more energy to the powder particle[5].

Surfactant-assisted mechanical milling, which avoids the re-welding, could lead to particle refinement with an appropriate surfactant and organic carrier liquid[11]. Surfactants can lower the surface energy of the freshly formed fine particles by forming a thin organic layer and introducing a long range capillary forces that lower the energy for crack propagation. This prevents the particles from agglomeration and cold welding that substantially increase particle sizes in high energy ball milling operations[12]. The nature and quantity of the surfactant as well as the type of grinding material determine the size, shape and purity of the final product. Increasing the surfactant volume normally reduces the particle size usually by a magnitude of the second or third order[6].

In this research, the mechanical milling experiments were carried out with a SPEX 8000 Mixer/Mill for various periods of time. A cylindrical hardened steel vial and hardened steel balls of diameter 12.5 mm were used. The ball-to-sample weight ratio was kept (7~9):1. The loading of the powders into the vial is done inside glove boxes filled with Nitrogen gas. To reduce heating, the milling was done on an intermittent basis, with 5 minutes of milling followed by 5 minutes off. In surfactant-assisted mechanical milling, heptane (99.8% purity) was used as milling medium, and oleic acid (90%) as surfactant during milling. The amount of surfactant used was the same as the weight of the powder.

3. 1. 4 Heat treatment

Heat treatment is the process of heating or cooling a material to alter their microstructure. The heat treatment process involves heating the material to a predefined temperature, maintaining that temperature for a specific duration and cooling the materials to room temperature. Heat treatment can manipulate the properties of the

materials by controlling the rate of diffusion within the microstructure. In crystalline materials, the atoms will rearrange themselves in the lattice depending on temperature, pressure, etc., which would alter their properties such as hardness, strength, toughness, ductility, elasticity, etc. When in solute state, the process of diffusion causes the atoms of the dissolved element to spread out, attempting to form a homogenous distribution within the crystals of the base metal. Heat treatment can also relieve the stress, reduce/enhance the hardness under different conditions.

In this study, the materials were wrapped in tantalum foil and then sealed in a quartz tube, which is repeatedly evacuated/backfilled with UHP Ar to avoid oxidization. The heat treatment was conducted in the tube/box furnace followed by water quenching or slow cooling in air/furnace.

3. 2 Structure characterization

3. 2. 1 X-ray diffraction (XRD)

3. 2. 1. 1 Bragg's law

X-ray diffraction is a non-destructive analytical technique which reveal the information about the crystal structure and chemical composition of bulk, powder materials and thin films. It's based on observation of scattered intensity of an X-ray beam hitting a sample as a function of incident and scattered angle, polarization and wavelength or energy.

X rays are electromagnetic radiation with wavelengths in the range of 0.01~10 nm. It's comparable to the interatomic distances in the lattice, and diffraction of x-rays

through the closely spaced lattice of atoms in a crystal could be used to reveal the nature of the lattice. When the x-rays impinge on a crystal, they'll be scattered in all directions by the atoms of the crystal. Increase of intensity in some direction could be observed due to the constructive interference of the scattered waves. The conditions for constructive interference are derived from the geometrical analysis of the scattering of an x-ray beam by planes of atoms in a crystal as shown in Figure 3.4. This leads to Bragg's law[13]:

$$n\lambda = 2d_{hkl}\sin(\theta) \tag{3.1}$$

where λ is the wavelength of the x-ray beam, *n* is an integer determined by the order given, θ is the incident angle, d_{hkl} is the interplane distance. A diffraction pattern is obtained by measuring the intensity of scattered waves as a function of scattering angle. Very strong intensities known as Bragg peaks are obtained in the diffraction pattern when the geometry satisfies the Bragg condition.

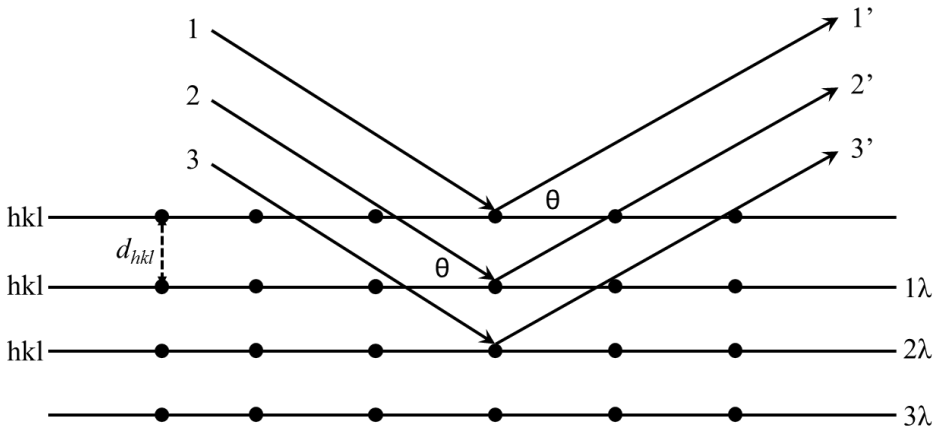

Figure 3.4 Schematic illustration of diffraction of x-rays by a crystal

3. 2. 1. 2 Williamson-Hall equation

While the Bragg equation predicts delta function peaks, real instruments and real materials result in diffraction slightly off of the Bragg angle, leading to Gaussian-type or Lorentzian-type intensity distributions. The crystallite size and lattice strain are the two aspects of a material which influence the peak width The crystallite size broadening varies as $1/\cos\theta$ while strain varies as $\tan\theta$[14].

The Williamson-Hall technique is useful in sorting out the crystallite size and strain effects from one another. First of all, the breadth of a given diffraction peak is due to the crystallite size, the strain and the instrumental effects. The full width at half maximum (FWHM) of the Lorentzian-shaped diffraction peaks was used as the diffraction breadth. The observed peak broadening B_0 could be represented as

$$B_0 = B_c + B_s + B_i \tag{3.2}$$

where B_0 is the observed peak broadening in radians; B_i the broadening due to instrumental factors in radians; B_c is the broadening due to crystallite size and B_s is the broadening due to residual stress.

According to Scherrer equation, the broadening due to crystallite size may be expressed as

$$B_c = \frac{k\lambda}{t\cos\theta} \tag{3.3}$$

where B_c is the broadening due to small crystallite size; k is a constant, usually taken as 1; t is the crystallite size in nanometers; θ the Bragg angle; and λ is the wavelength of incident x-ray beam in nm.

According to Wilson[15], the broadening due to residual strain could be expressed

$$B_s = \eta \tan\theta \tag{3.4}$$

where B_s is the peak broadening due to lattice strain; η the strain distribution within the material, and θ is the Bragg's angle.

Based on Eqs (2) and (3), the Eqs (1) could be transformed

$$B_r \cos\theta = \frac{k\lambda}{t} + \eta \sin\theta \tag{3.5}$$

The plot of $B_r cos\theta$ versus $sin\theta$ gives a straight line with slope equal to η and the intercept along y-axis as $k\lambda/t$. Therefore, the crystallite size t can be calculated from the intercept.

3. 2. 2 Transmission Electron Microscopy (TEM)

Transmission Electron Microscope (TEM) technique is one of the most useful techniques for crystal structure, microstructure characterization, and composition analysis at the atomic scale[16]. Since the resolution of a compound microscope is limited to half of the wavelength of the radiation used for imaging, a huge improvement in resolution is achieved with TEM by replacing the large wavelength light beam with an electron beam that has a wavelength of approximately 0.005 nm. In TEM, the electron beams are generated either by a tungsten or LaB_6 filament, or by a field emission gun. The electron beam is accelerated under vacuum through a voltage of up to 200 kV, and goes through electromagnetic lenses.

The electron column of the TEM is comprised of an electron gun and the condenser lenses, which transfer the electrons from the source to the specimen. In the electron gun, the electron beam is accelerated to an energy in the range of 20~1000 keV, then the electron beam passes through set of condenser apertures before reaching the sample, which would produce a beam of electrons with a desired diameter. The apertures are annular metallic plates, through which electrons are further focused. During this process, the beam intensity is decreased as some electrons are filtered from the beam. Meanwhile, the filtering removes electrons that are scattered to high angles. So the aperture size controls the maximum illumination intensity and the image quality.

During TEM experiment, the sample is placed in front of the objective lens in a form of thin foil, thin section, or fine particles transparent for the electron beam[17]. The incident electron beam is diffracted by the lattices of the crystal, forming the Bragg beams which are propagating along different directions. The electron-specimen interaction results in phase and amplitude changes in the electron wave that are determined by quantum mechanical diffraction theory. The diffracted beams will be focused in the back focal plane, where an objective aperture could be applied. An ideal thin lens brings the parallel transmitted waves to a focus on the axis in the back focal plane. The diffraction pattern would be generated. When the transmitted electron beam is focused on the image plane of an objective lens and introduce an aperture in the back focal plane of the objective lens an image of the sample is produced on the screen (Figure 3.5).

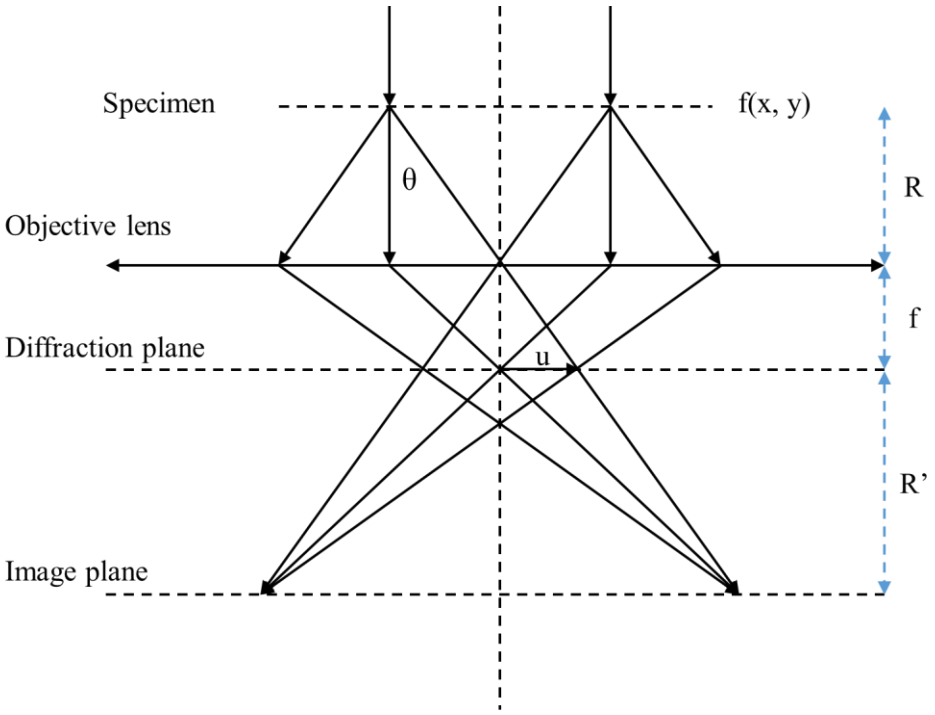

Figure 3.5 Schematic illustration of image formation in a one-lens transmission electron microscope[17]

3. 2. 2. 1 Electron Diffraction

From electron diffraction pattern, quantitative structural and crystallographic information about the crystalline materials can be collected. Since the selected area for diffraction could be as small as several nanometers, unsurpassed localized information of individual nanoparticles can be obtained[18].

Assume the electron beam as monochromatic electron wave, the atoms in the crystalline materials will act as scattering centers as shown in Figure 3.6. Constructive interference of the transmitted electron beam would increase the electron wave amplitude, while destructive interference will cancel out the waves. The results of the propagating

electron wave through the crystal will be a diffraction pattern as regular array of scattered intensities, which carry the information about the crystal structure.

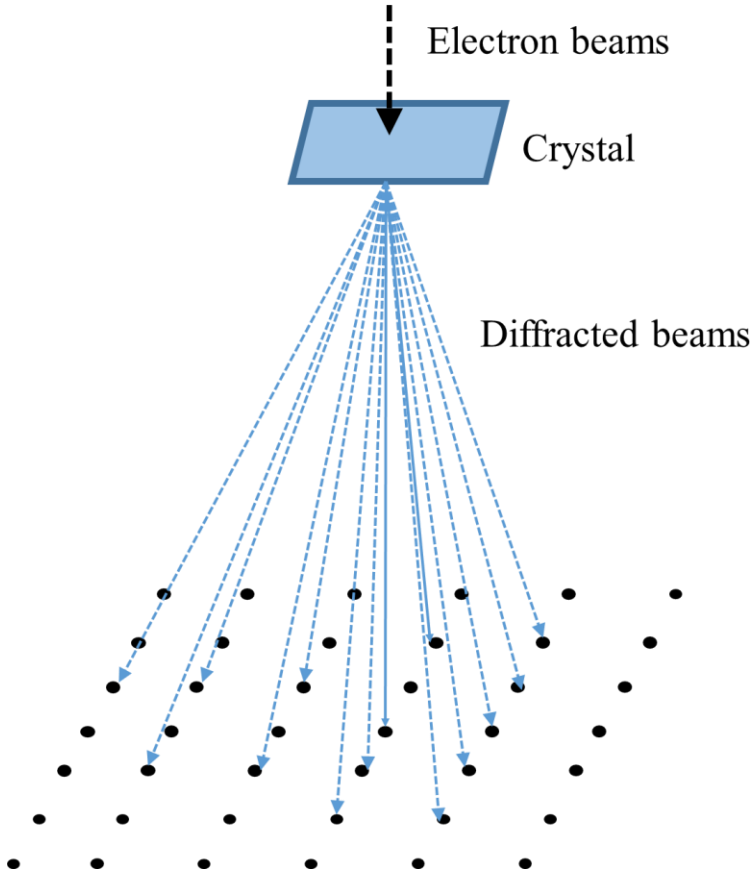

Figure 3.6 Schematic illustration of formation of electron diffraction patterns, which are essentially projections of the reciprocal lattice section in the plane of the crystal normal to the electron beam

3. 2. 2. 2 Image formation in TEM

The modern high-resolution transmission electron microscope allows for direct imaging of the atomic structure of materials through image contrast, which would provide their detailed nano/micro- structure including grain boundary and defects in atomic scale. The image contrast, created by absorption of electrons, thickness and

composition in the material, is dominated by three types of contrast: mass-thickness contrast, diffraction/amplitude contrast and phase contrast[19].

Mass-thickness contrast is due to incoherent elastic scattering of electrons. Electrons are scattered off axis by elastic nuclear interaction when the electrons transmit the specimen. The elastic scattering is proportional to the thickness of the specimen since the mean-free path is fixed. Meanwhile, the cross section for elastic scattering is a function of the atomic number, and higher atomic number would enhance the scattering. Thus differential intensity in an image would form from thick regions to thin regions and from high atomic number region to low atomic number region. Mass-thickness contrast is the primary imaging mechanism for non-crystalline materials. It can be controlled by the size of the objective aperture and the accelerating voltage. Smaller aperture and lower accelerating voltage will increase the difference in the ratio of scattered and transmitted electrons, extensively enhance the mass-thickness contrast.

Diffraction contrast is introduced by interception of diffracted electrons leaving the lower surface of the crystalline specimen by the objective aperture. It's widely used in microstructure (>15 Å) and defects study in crystalline materials. There are three diffraction contrast imaging modes for crystalline materials: bright field (BF), displaced aperture dark field and centered dark field (CDF). BF image can be obtained when a small aperture (5~70 μm diameter) is inserted in the back focal plane of the objective lens to intercept the diffracted beam and only allow the transmitted beam to go through. Alternatively, displaced aperture dark field image could be observed when the objective aperture is displaced from the optic axis to intercept the transmitted beam and allow the diffracted beam to contribute to the image. When the illumination incident on the

specimen is tilted so that the diffracted electrons can travel along the optic axis in the displaced aperture dark field, higher resolution images could be formed, which is centered dark field mode.

Phase contrast arises due to differences in the phases of the electron waves scattered through the specimen. In bright- and dark-field mode, the central electron beam or a single diffracted beam are collected to form an image. But in phase contrast images, interference between the transmitted beam and scattered beam contributes to the high resolution in images. It is the basis for high-resolution TEM (HRTEM), and widely applied in direct lattice plane resolution, multi-beam lattice images, Moiré patterns, and point-to-point resolution tests.

3. 2. 3 Positron Annihilation Spectroscopy (PAS)

Positron Annihilation Spectroscopy (PAS) is a characterization method for probing the local electron density and atomic structure at the site chosen by the electrostatic interaction of the positron with its environment[20]. PAS is based on the detection of gamma radiation after annihilation of a positron with an electron in the material, using either positron lifetime or annihilation gamma ray information, such as energies or angles of detected gamma rays, to extract basic structural features of materials[21].

Existence of positrons was predicted in 1928[22] and the experimental observation of positrons was in 1932[23], but the positron-electron annihilation experiment was conducted in the 1940s and 1950s. Application of positron annihilation in lattice defects

in metals was in the late 60's[24-26]. Information carried by gamma rays after annihilation of positrons can be used to study structural properties of various materials.

The most commonly used source for positron production is sodium-22 with a relatively long half–life of 2.6 years and large rate of positron production (90%). The decay scheme of ^{22}Na is

$$^{22}Na \rightarrow \quad ^{22}Ne + \beta^{+} + v_e + \gamma \tag{3.6}$$

where v_e and γ are the neutrino and gamma ray, respectively, and β^+ is the positron. When an energetic positron is injected into condensed materials, it rapidly loses almost all of its energy by a succession of ionizing collisions with electrons and ions of the medium, with thermal energies (~0.27 eV) remaining. The process of transferring energy to the material is called thermalization. During the energy loss process, the positrons travel certain distances into the materials, depending on the initial energy and type of interaction. After stopping in the material, positrons can be directly annihilated with the surrounding electrons, either from a freely diffusing state or from a trapped state (at a defect site), predominantly producing two gamma rays. Because of mass motion of the annihilating positron-electron system, the gamma rays will be Doppler shifted from the center energy of 511 keV. Since the positrons are thermalized, the Doppler shift will be dominated by the momentum of the electrons participating in the annihilation. Generally, valence electrons mainly contribute to the low momentum part of the spectrum and core electrons give rise to the high-momentum region of the annihilation line[21]. Thus, the shape of the annihilation spectrum can be analyzed by line shape parameters *S* and *W* as shown in Figure 3.7, where *S* is defined as the ratio of counts in the peak region of the spectrum to the total counts, whereas the *W* parameter is the ratio of counts in the wing (tail) region to

the total counts[27]. The *S* parameter represents the fraction of positrons annihilated mainly with the valance electrons and the *W* parameter represents the fraction of annihilations with core electrons with a large momentum component. When positrons annihilate after being trapped at vacancy-type defect sites, annihilation occurs predominantly with lower momentum electrons as opposed to the annihilation events occurred in the defect-free region where annihilation mostly comes from higher momentum electrons. As a result, open-volume defects produce higher *S* values compared to defect-free regions of the sample. The measured value of the *S* parameter is directly related to the size or concentration (or mix of both) of open-volume defects. A larger *S* value corresponds to larger open-volume or higher vacancy-type defect concentration. The *W* parameter is primarily associated with the chemical environment of annihilation sites.

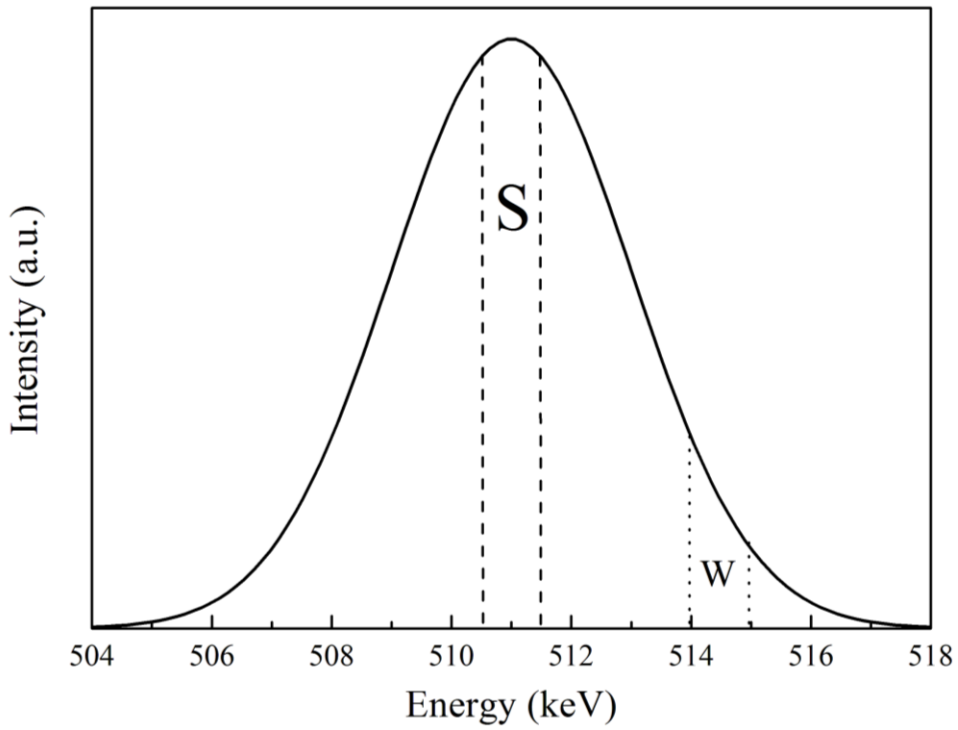

Figure 3.7 Schematic illustration of S- and W- Parameter calculation regions

3. 3 Magnetic property characterization

The characteristics of magnetic materials, including saturation magnetization, coercivity, and permeability, are best determined from a hysteresis loop. The most common measurement method employed for hysteresis loop determinations at ambient temperature is the Vibrating Sample Magnetometer (VSM), while Superconducting Quantum Interference Device (SQUID) is preferred when sensitivity is required. In the measurements, ribbon samples with mass around 1 mg were measured directly, but the powder samples were embedded in epoxy resin, ensuring the sample would not move under varying magnetic field. In this study, a Quantum Design Magnetic Property Measurement System (MPMS) superconducting quantum interference device magnetometer (SQUID) with applied field of 7 T and vibrating sample magnetometer (Lakeshore 8500) with magnetic field up to 9 kOe were employed for magnetic measurements.

3. 3. 1 Vibrating Sample Magnetometer (VSM)

VSM systems are used to measure the magnetic properties of materials as a function of magnetic field, temperature, and time[28-30]. Powders, solids, liquids, single crystals, and thin films are all readily accommodated in a VSM. Experimental flexibility, both in terms of achievable field strengths, and in terms of allowable sample sizes are provided since the gap spacing may be adjusted to maximize either[28]. As shown in Figure 3.8, the sample is placed on a long rod and then driven by a mechanical vibrator. The rod is positioned between the pole pieces of an electromagnet to which detection coils have been mounted. The oscillatory motion of the magnetized sample will induce a voltage in

the detection coils. The induced voltage is proportional to the sample's magnetization, which can be varied by changing the dc magnetic field produced by the electromagnet[31].

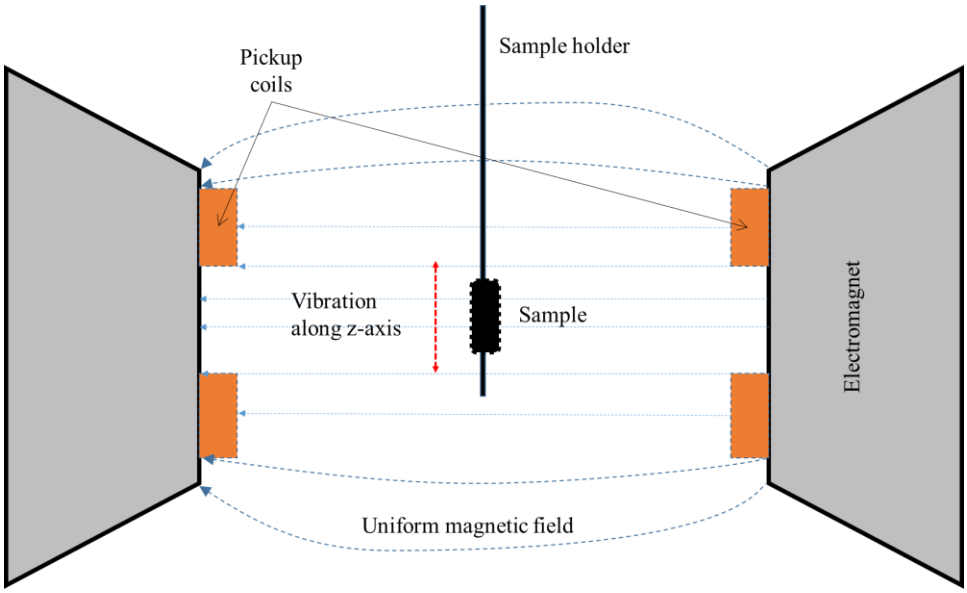

Figure 3.8 Schematic illustration of sample holder and detection mechanism in VSM

3. 3. 2 Superconducting Quantum Interference Device (SQUID)

The superconducting quantum interference device (SQUID) magnetometer is one of the most sensitive experimental techniques to magnetically characterize samples , as the sensitivity is on the order of 10^{-9} emu[32]. It is based on superconducting loops containing Josephson junctions, which consists of two superconductors separated by thin narrow insulating gaps. Typically, a SQUID combines several superconducting components including a superconducting magnet, detection coils, flux transformer and superconducting shields as shown in Figure 3.9. To make a measurement, the sample attached on the sample rod is scanned through the superconducting coil, which forms a closed flux transformer. Changes of sample position cause variable magnetic flux through the coils. The shape and magnitude of the response curve can be analyzed to obtain a

corresponding magnetic moment. The magnetic field is produced by the superconducting magnet and is uniformly distributed throughout the coil area. Temperature control is conducted by placing the sample in a sealed variable temperature insert, which is thermally isolated from the coil by an annular vacuum space. Normally, SQUID systems offer the ability to measure in high applied fields over a temperature range from above room temperature down to below 10 K.

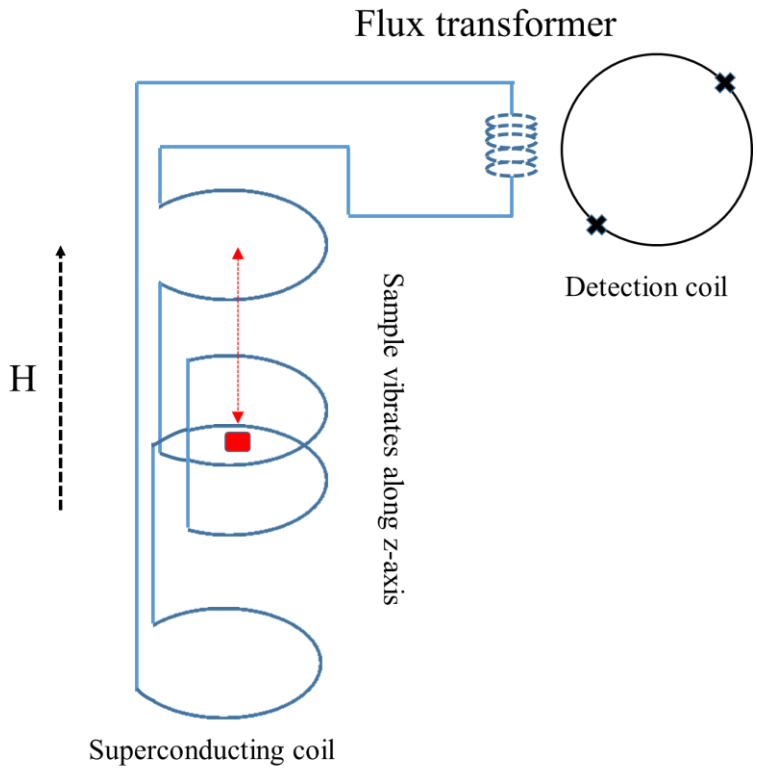

Figure 3.9 Schematic diagram of SQUID magnetometer

In this research, samples (~1mg) embedded in epoxy resin are mounted in a straw with vertical length <5mm. A SQUID magnetometer utilizing a Quantum Design MPMS with a maximum field of 7 T was employed for the measurement at 300 K.

3. 4 Thermodynamic characterization: Differential Thermal Analysis (DTA)

DTA involves heating or cooling a test sample and an inert reference under identical conditions, while recording any temperature difference between the sample and reference. Changes in the sample which lead to the absorption or evolution of heat can be detected relative to the inert reference. Thus, the DTA curve provides information on the first-order transformations, such as glass transitions, crystallization, melting and sublimation. The area under a DTA peak represents the enthalpy change and is not affected by the heat capacity of the sample.

As shown in Figure 3.10, the DTA is mainly composed of 4 parts: sample holder comprising thermocouples, sample containers and a ceramic or metallic block; furnace; temperature programmer and recording system. Experiments are frequently performed on powders so the resulting data may not be representative of bulk samples, where transformations may be controlled by the buildup of strain energy. The shape of the DTA peak depends on sample weight and the heating rate. Lower heating rate and reduction in sample weight will both lead to shaper peaks with improved resolution. In this study, the reference sample is Al_2O_3 powder and the measurement is under the protection of UHP Ar. The heating rate is set 10 ℃/min controlled by a Perkin-Elmer System.

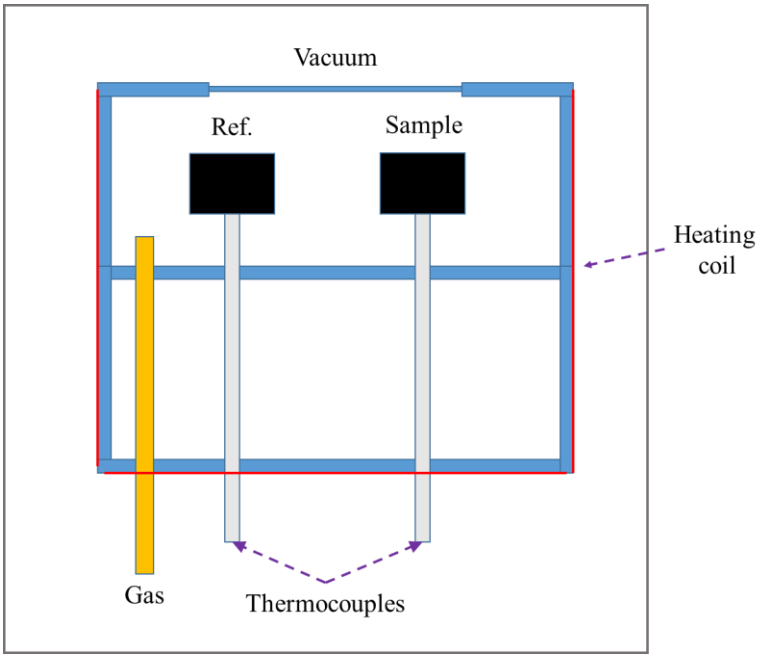

Figure 3.10 Schematic illustration of DTA instrument

References

1 Arajs, S. & Wray, G. A laboratory arc melter. *Journal of Physics E: Scientific Instruments* **2**, 518 (1969).

2 Jacobson, L. A. & McKittrick, J. Rapid solidification processing. *Materials Science and Engineering: R: Reports* **11**, 355-408 (1994).

3 Šuler, M., Kosec, L., Bizjak, M., Kosec, B., Kneissl, A., Brunčko, M., Raić, K. & Anžel, I. Rapidly solidified copper alloys ribbons. *Metalurgija* **14**, 67-74 (2008).

4 Jiang, X. Structural, magnetic and microstructural studies of composition-modified Sm-Co ribbons. (2014).

5 Suryanarayana, C. Mechanical alloying and milling. *Progress in Materials Science* **46**, 1-184 (2001).

6 Ullah, M., Ali, M. E. & Hamid, S. B. A. SURFACTANT-ASSISTED BALL MILLING: A NOVEL ROUTE TO NOVEL MATERIALS WITH CONTROLLED NANOSTRUCTURE-A REVIEW. *Rev. Adv. Mater. Sci* **37**, 1-14 (2014).

7 Suryanarayana, C. Does a disordered γ-TiAl phase exist in mechanically alloyed Ti Al powders? *Intermetallics* **3**, 153-160 (1995).

8 Chin, Z.-H. & Perng, T. in *Materials Science Forum.* 73-78 (Trans Tech Publ).

9 Kis-Varga, M. & Beke, D. L. in *Materials Science Forum.* 465-470 (Aedermannsdorf, Switzerland: Trans Tech Publications, 1984-).

10 Suryanarayana, C., Chen, G.-H. & Froes, F. Milling maps for phase identification during mechanical alloying. *Scripta Metallurgica et Materialia* **26**, 1727-1732 (1992).

11 Chakka, V., Altuncevahir, B., Jin, Z., Li, Y. & Liu, J. Magnetic nanoparticles produced by surfactant-assisted ball milling. *Journal of Applied Physics* **99**, 08E912 (2006).

12 Guérard, D. Ball milling in the presence of a fluid: results and perspectives. *Rev. Adv. Mater. Sci* **18**, 225-230 (2008).

13 Stock, S. & Cullity, B. Elements of X-ray diffraction. *Prentice Hall, New Jersey, 2001) p* **275** (2001).

14 Prabhu, Y. T., Rao, K. V., Kumar, V. S. S. & Kumari, B. S. X-Ray Analysis by Williamson-Hall and Size-Strain Plot Methods of ZnO Nanoparticles with Fuel Variation. *World Journal of Nano Science and Engineering* **4**, 21 (2014).

15 Wilson, A. X-ray optics, Methuen & Co. *Ltd., London* (1949).

16 Williams, D. B. & Carter, C. B. in *Transmission Electron Microscopy* 3-22 (Springer, 2009).

17 Wang, Z. Transmission electron microscopy of shape-controlled nanocrystals and their assemblies. *The Journal of Physical Chemistry B* **104**, 1153-1175 (2000).

18 Fultz, B. & Howe, J. *Transmission electron microscopy and diffractometry of materials*. (Springer, 2012).

19 Reimer, L. & Kohl, H. *Transmission electron microscopy: physics of image formation*. Vol. 36 (Springer, 2008).

20 Tuomisto, F. & Makkonen, I. Defect identification in semiconductors: Experiment and theory of positron annihilation. *Rev. Mod. Phys*.

21 Bosnar, D., Friščić, I., Jerbić-Zorc, G., Makek, M. & Bosnar, S. in *International Topical Meeting on Nuclear Research Applications and Utilization of Accelerators, Book of Abstracts, International Atomic Energy Agency, American Nuclear Society, Vienna.* 46.

22 Dirac, P. A. The quantum theory of the electron. *Proceedings of the Royal Society of London. Series A, Containing Papers of a Mathematical and Physical Character*, 610-624 (1928).

23 Anderson, C. D. The positive electron. *Physical Review* **43**, 491 (1933).

24 MacKenzie, I., Khoo, T., McDonald, A. & McKee, B. Temperature dependence of positron mean lives in metals. *Physical Review Letters* **19**, 946 (1967).

25 Bergersen, B. & Stott, M. The effect of vacancy formation on the temperature dependence of the positron lifetime. *Solid State Communications* **7**, 1203-1205 (1969).

26 Connors, D. & West, R. Positron annihilation and defects in metals. *Physics Letters A* **30**, 24-25 (1969).

27 Asoka-Kumar, P. & Lynn, K. Applications of positron annihilation spectroscopy. *Le Journal de Physique IV* **5**, C1-15-C11-25 (1995).

28 Dodrill, B. Magnetic Media Measurements with a VSM. *Lake Shore cryotronics, Inc* **575**.

29 Noakes, J., Arrott, A. & Haakana, C. Vibrating sample magnetometers. *Review of Scientific Instruments* **39**, 1436-1438 (1968).

30 Smith, D. Development of a Vibrating-Coil Magnetometer. *Review of Scientific Instruments* **27**, 261-268 (1956).

31 Burgei, W., Pechan, M. J. & Jaeger, H. A simple vibrating sample magnetometer for use in a materials physics course. *American Journal of Physics* **71**, 825-828 (2003).

32 Sawicki, M., Stefanowicz, W. & Ney, A. Sensitive SQUID magnetometry for studying nanomagnetism. *Semiconductor Science and Technology* **26**, 064006 (2011).

Chapter 4 Defects analysis in mechanically alloyed stoichiometric Fe-Ni alloys

This chapter describes the effect of high-energy mechanical alloying on the structural and magnetic properties of FeNi alloy. It has been discussed in Chapter 1 that FeNi, with chemically-ordered $L1_0$ tetragonal structure, is a promising material for next-generation rare-earth free permanent magnets. However, due to the extremely low atomic Fe and Ni mobilities below the critical chemical order/disorder temperature of 320℃, no conventional metallurgy methods are able to induce its formation. Since diffusion rates could be enhanced with the creation of excessive vacancies, high-energy mechanical alloying was employed to produce a nanocrystalline Fe-50 at.% Ni alloy. The high energy mechanical milling is expected to change the defect characteristics that would be used to study the effect mechanical alloying has on the defect concentrations. X-ray diffraction revealed that over the entirety of the milling period, the Fe and Ni powders formed an fcc solid solution. The Williamson-Hall equation and Scherrer equation revealed the reduction of grain size. The initial increase in internal strain, and by extension dislocations, was followed by a subsequent decrease with further alloying, which was due to the combination effect of creation of dislocations from mechanical deformation and annihilation of dislocations at increasing grain boundaries. Doppler broadening positron annihilation spectroscopy showed that the overall number of open-volume defects decreased with increasing alloying time. Finally, changes of relative

permeability, for the mechanically alloyed FeNi phase, were explained by the pinning in domain walls by dislocations.

4. 1 Introduction

The $L1_0$-type ordered FeNi alloy, abundant and inexpensive, shows promising permanent magnetic properties: high coercivity (500~4000 Oe) and magnetic anisotropy (1.3×10^7 erg/cm^{-3})[1-5]. It has a chemically ordered tetragonal structure with alternating monatomic layers of Fe and Ni along the c-axis direction. According to the FeNi equilibrium phase diagram, the $L1_0$ phase forms as an equilibrium phase below 320 ℃[6]. Due to the extremely slow Ni diffusion at 320 ℃, it will take 4.6 billion years to complete the transformation from γ_1 phase (the paramagnetic fcc phase) to the γ" ($L1_0$-FeNi) phase[4]. Neutron irradiation at high temperature[4] and alternate monatomic layer deposition using molecular beam epitaxy[7-11] were reported to produce $L1_0$-FeNi. However, these approaches are not ideal for device applications and large-scale production.

Since the disorder-order transformation from the fcc structure to the $L1_0$ structure is dependent on the rate of diffusion, increasing the concentration of vacancies will enhance the diffusion coefficient for Ni atoms in the FeNi alloy[12]. Mechanical alloying, widely used in ceramic and metal processing, can produce ultrafine nanostructured materials. It involves repeated cold welding, fracture, and rewelding of a fine blend of metal, oxide, or alloy particles resulting in size reduction and alloy formation[13]. A rapid increase of vacancy concentration followed by a gradual increase in the concentration of antisite defects was observed in the In-Pd system, while the saturation of defects at ~3% was achieved after 30 min of milling[14]. This is due to the high ordering energy of the

InPd alloy, which favors vacancy production rather than atomic disordering. However, atomic disorder rather than point defect formation was introduced by mechanical alloying in the Fe-Al system[15]. It is unclear whether mechanical alloying will introduce vacancies or structural disorder in the Fe-Ni system, but both may aid in increasing diffusion rates and lead to $L1_0$ ordering post-annealing.

Thus, mechanical alloying is employed in this research to create vacancies in the Fe-Ni system, and changes in defect concentration, with increasing milling time, were investigated by positron annihilation spectroscopy (PAS). PAS is a standard technique used to characterize open volume defects such as vacancies and dislocations in a variety of materials[16]. It also permits an estimate of the free volume fluctuations in condensed matter[17]. PAS has been used to qualitatively assess defect changes in bulk metallic glasses (BMGs) in relation to sub-Tg annealing[18,19], plastic deformation[20,21], cooling rate variations[22] and fatigue-induced cracks[23]. Positron beams with variable, low implantation energies can also be used to study surface behavior[16]. In the present work, Doppler broadening spectroscopy of positron annihilation was applied on Fe-50 at.%Ni samples mechanically alloyed at various intervals up to 90 h. Grain boundaries and dislocations were quantitatively analyzed using the Scherrer equation and Williamson-Hall equation. Finally, the relationship between induced defect concentration and the magnetic properties of FeNi was investigated.

4. 2 Experiment procedure

Fe powder (10 μm, 99.9+% purity, Alfa Aesar Inc.) and Ni powder (5~15 μm, 99.8% purity, Alfa Aesar Inc.) were mechanical alloyed for 10, 20, 30, 40, 60 and 90 h in

a SPEX 8000 Mixer/Mill in an Ar atmosphere. A cylindrical, hardened steel vial and hardened steel balls of diameter 12.5 mm were used. The ball-to-sample weight ratio was 7:1. To minimize heating inherent to the mechanical milling process, the milling was done on an intermittent basis, with 5 minutes of milling followed by 5 minutes off. X-ray diffraction was utilized to determine the phase evolution and was conducted using a PANalytical Empyrean with Cu-Kα radiation. A Quantum Design Magnetic Property Measurement System (MPMS) Superconducting Quantum Interference Device (SQUID) magnetometer with applied field ~2 T was utilized to obtain magnetic measurements at room temperature.

Doppler broadening positron annihilation spectroscopy (DBPAS) was employed to analyze the vacancy-type defects in the material as a function of depth. Samples for DBPAS were prepared from compacted powder and were irradiated by positron beams with energies from several eV to 70 keV. The penetration depth of positrons at 70 keV is ~5 μm in Fe-50 at.%Ni samples. After injection, positrons quickly thermalize and diffuse through the material and either annihilate by combining with free electrons or become trapped in vacancy-type defects before annihilation. Annihilations of positrons with electrons release two γ rays with energy of 511 keV in opposite direction which were detected by high purity Ge detectors. Due to the momenta of the annihilated electrons, the 511 keV line is broadened. This broadening is generally characterized by the line shape parameters *S* and *W*, defined as the fractions of annihilation counts in the central region and the wing region to the total counts in the spectrum, respectively. The *S* parameter is associated with valence band electrons and sensitive to neutral or negatively charged vacancy-type defects. The *W* parameter is mainly associated with the chemical

environment around the annihilation site. A larger S corresponds to a larger open volume or more defect concentrations[24].

4. 3 Grain boundaries and dislocations estimated from XRD pattern

The x-ray diffraction patterns for Fe-50 at.%Ni samples with mechanical alloying times of 10 min, 10h, 20h, 30h, 40h, 60h and 90h are shown in Figure 4.1. The phases present in the 10-min-milled sample are fcc Ni and bcc Fe phases. When milled for 10 h and longer, all of the observed diffraction peaks were indexed to an fcc FeNi structure.

Lattice parameters of all samples were extrapolated from the $a \sim cos(\theta/2)$ function using the first 4 peaks from their XRD patterns, where a is the lattice parameter calculated from each peak, θ is the Lorentz shaped diffraction peak. The lattice parameter is extracted from the intercept of the linear fit made to the data. The lattice parameters were constant at 3.64 ± 0.02 Å with mechanical alloying for ~90 h (Figure 4.2), but the peak breadth did change noticeably. Since peak broadening could be caused by both grain size and strain, the Williamson-Hall (W-H) equation[25] was employed assuming the strain present in the material is uniform.

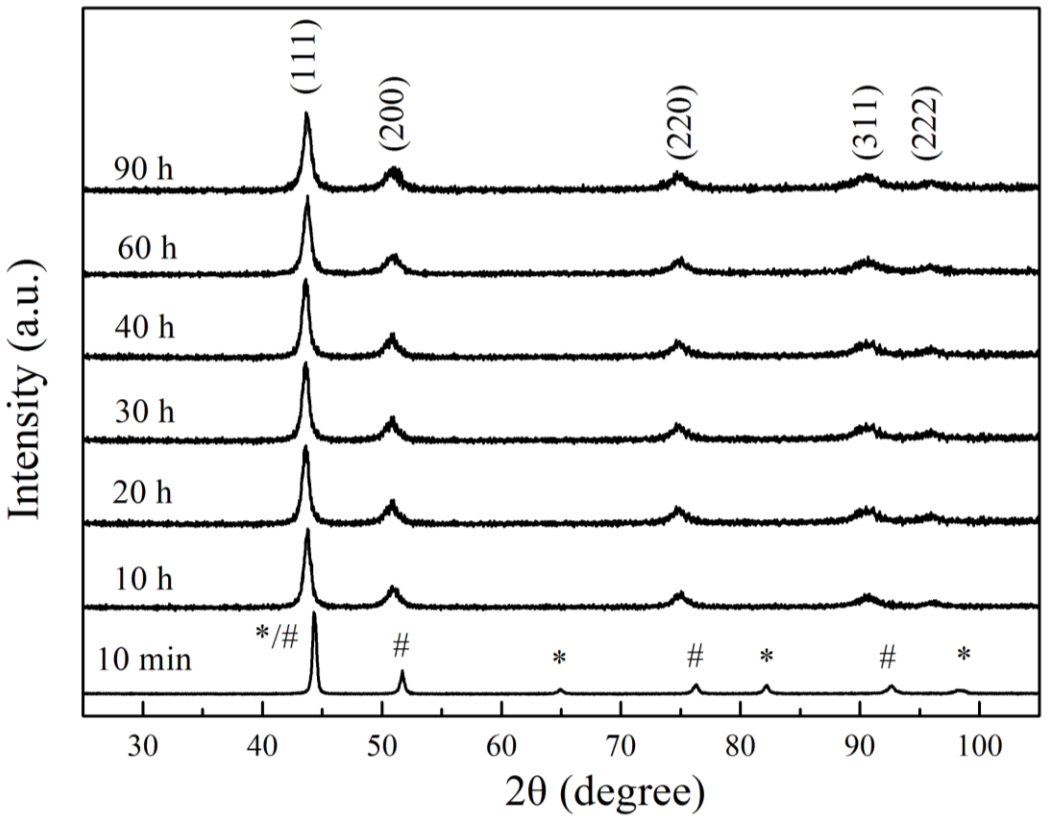

Figure 4.1 X-ray diffraction pattern for Fe-50 at.%Ni with different mechanical alloying time (*: BCC Fe phase; #: FCC Ni phase)

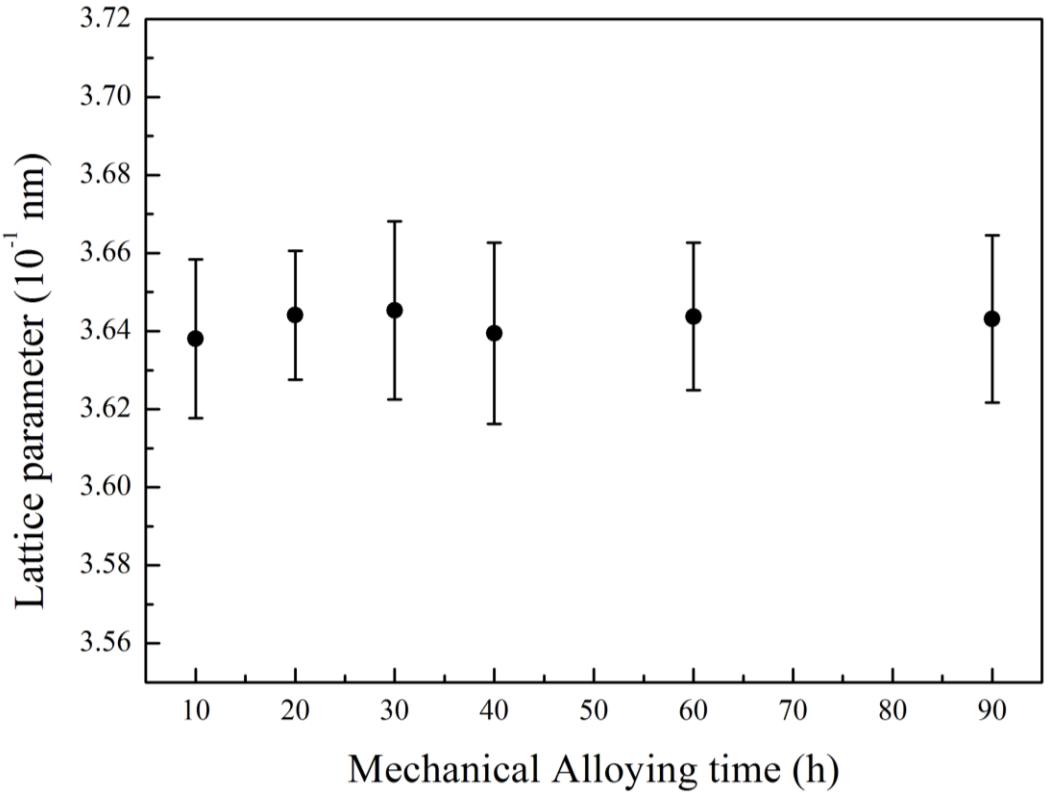

Figure 4.2 Lattice parameters for Fe-50 at.%Ni with different mechanical alloying time

The W-H equation for the total peak broadening is given by

$$B_r \cos\theta = \frac{k\lambda}{t} + \eta \sin\theta \qquad (4.1)$$

where k is a constant (usually 1), t is the crystallite size in nanometers, θ is the Bragg's angle, λ is the incident x-ray wavelength (in nm), and η is the strain within the material[26]. B_r is the instrument-corrected peak width (in radians) given as $B_r = (B_0^2 - B_i^2)^{1/2}$. In this equation, B_0 is the observed peak width and B_i is the broadening due to instrumental factors (both in radians). A plot is drawn by taking $sin\theta$ along the X-axis and $B_r cos\theta$ along the Y-axis as shown in Figure 4.3. The Williamson-Hall plot is for Fe-50 at.%Ni sample after high-energy mechanical alloying for 20 h. In the W-H plot, the strain present

in the material and crystallite size are, respectively, extracted from the slope and the intercept of the linear fit made to the data.

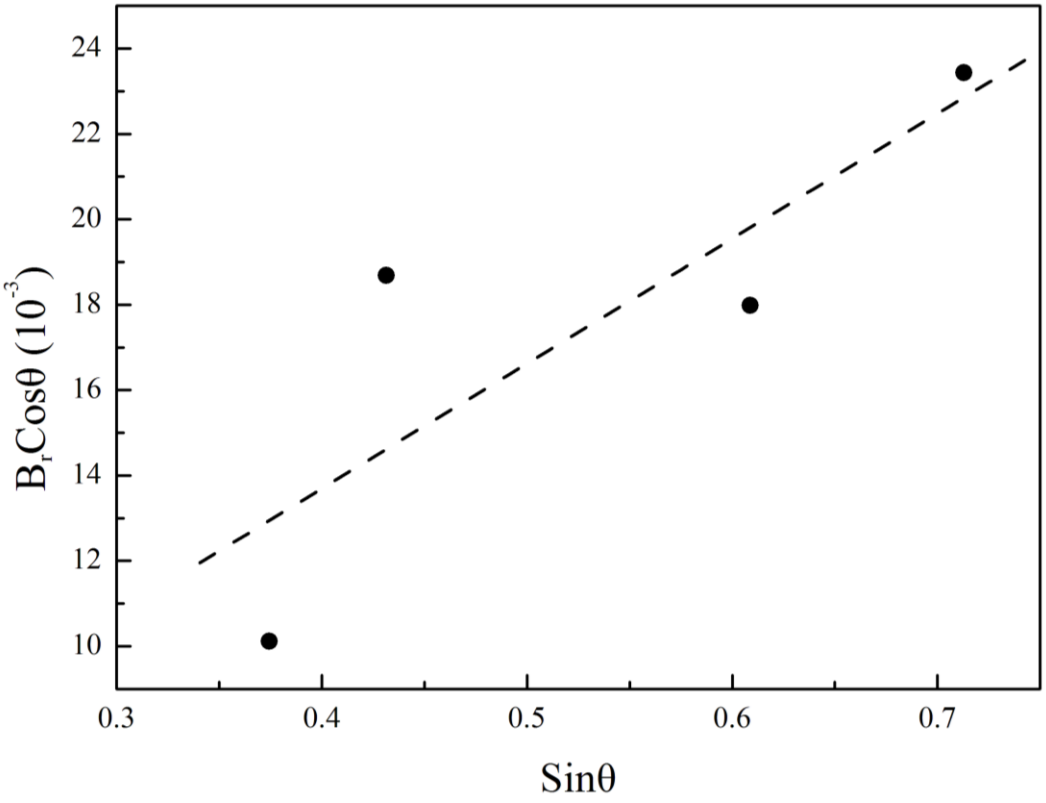

Figure 4.3 Williamson-Hall plot of Fe-50 at.%Ni after high-energy mechanical alloying for 20 h

Since the error for the grain size calculated from Williamson-Hall equation is too scattered, the Scherrer equation $d = \frac{k\lambda}{B_0 sin\theta}$ was utilized, which shows the same trend of the grain size as that calculated from Williamson-Hall equation. Thus, the grain sizes shown in Figure 4.4 is smaller than the actual grain sizes, considering the peak broadening caused by the internal strain. Reduction of grain size from 17 nm to 12 nm with mechanical alloying ~90 h was observed, which is due to the high degree of deformation experienced by powder particles. The deformation is introduced by the local

mechanical stresses of high intensity from the collision of high-speed balls. The effect of mechanical alloying on the internal strain was also shown in Figure 4.4. Interestingly, the initial increase in residual strain within the alloying time of 30 h was followed by gradual decrease with further alloying. This increase in strain when alloyed ~30 h could be due to mechanical deformation caused by fracturing of powder particles during high-energy mechanical alloying, which will introduce dislocations. With further alloying ~90 h, the strain was released and approached a steady-state value for long alloying times. The phenomenon of the initial increase followed by a subsequent decrease until steady-state value in internal strain was also found in other alloys such as $Fe_{30}Cu_{70}$ and $Fe_{90}Cu_{10}$[27]. It's been well known that grain boundaries can act as sources and sinks for dislocations[28]. Throughout the mechanical alloying process, a decrease in grain size is observed. This corresponds to an increase in the number of grain boundaries. Therefore, the strain peak observed at 30 h arises from a combination of first creating dislocations from mechanical deformation and then annihilation of these dislocations by grain boundary formation.

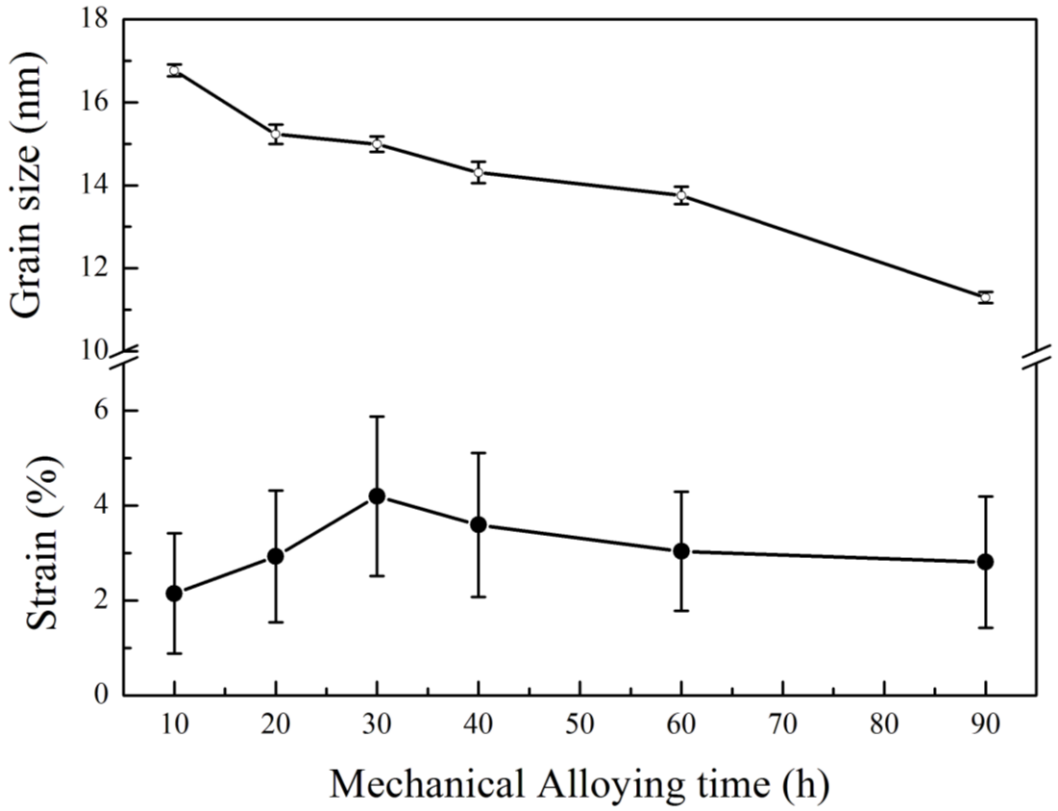

Figure 4.4 Effect of high-energy mechanical alloying on grain size and strain

4. 4 Net defect concentration determined by PAS

Further investigations on open-volume defects such as vacancies, vacancy agglomerates, dislocations, and free volume were done by DBPAS. Figure 4.5 shows the *S* parameters as a function of mechanical alloying time, where the *S* values at each alloying time were obtained by averaging respective *S* values over the energies from 30 to 70 keV since in this energy range annihilation mainly occurs in the bulk region of the sample, thus avoiding contributions from surface or near surface regions which can be affected by surface contamination like oxides. The data are normalized to the *S* value of the sample mechanically alloyed for 10 h (S_{10h}=0.417). As can be seen from Fig.5, the S

parameter decreased by nearly 1% from 10h to 90h of mechanical alloying, suggesting that there is a reduction in the concentration or the size of the open-volume defects during mechanical alloying. The rate of decrease in *S* appears to be higher between 10 h and 40 h, and then stabilizes upon further mechanical alloying. Considering the reduction in grain size (increase in the grain boundary area) and increase in dislocation, the decrease in open-volume defects could be the result of increasing internal homogeneity of the alloy[29], during which diffusion of Fe and Ni atoms could eliminate the vacancies, vacancy agglomerates and free volume formed from rewelding during mechanical alloying. Meanwhile, grain boundaries and dislocations could serve as sinks to vacancies during diffusion, which could also cause decreases in net defect concentrations.

The relationship between *S* and *W* provides information about the types of defects. In general, a linear set of (*S, W*) points is an indication that samples have the same kind of defects[30,31]. The Fig. 4.6 shows the graph of normalized valence annihilation parameters, *S* vs. the core annihilation parameter *W*, where *W* parameter is also normalized to corresponding values from the sample of 10h mechanical alloying time. As can be seen, the characteristic (*S, W*) is linear, indicating that all samples have the same type of defect(s). It also further suggests that mechanical alloying did not generate new types of defects at longer milling times, and that the concentration is reduced with mechanical alloying time.

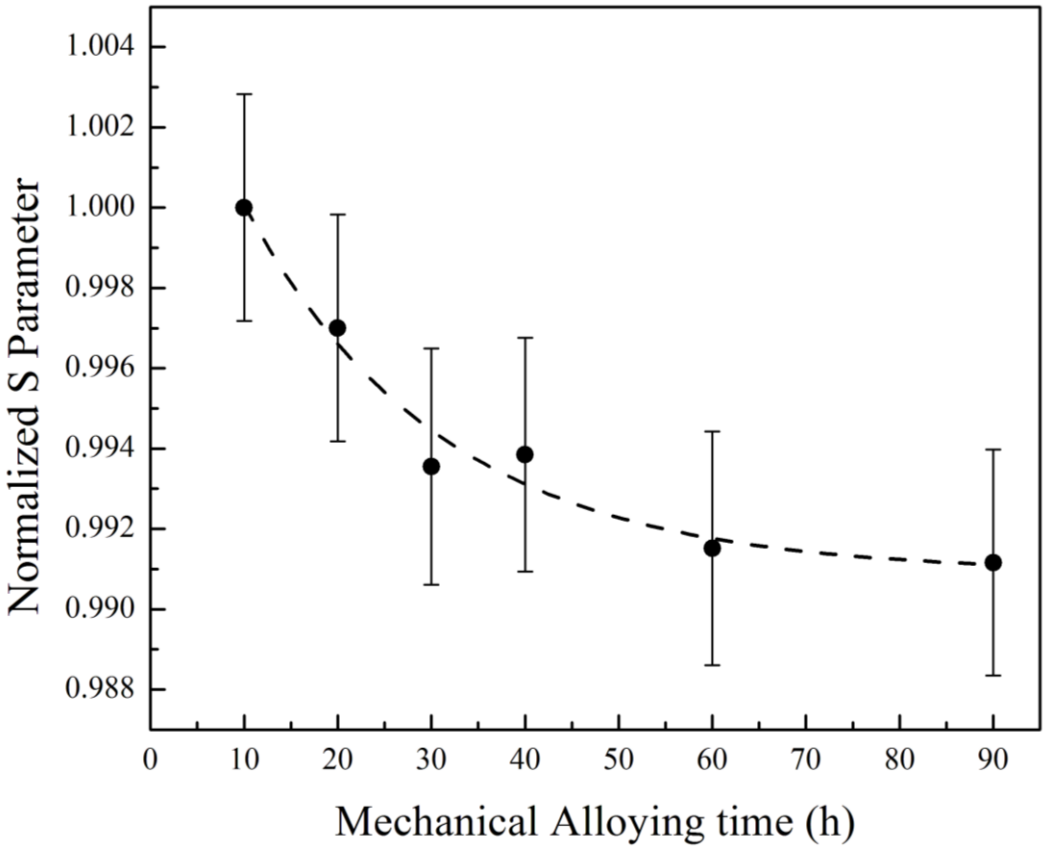

Figure 4.5 Normalized S parameters as a function of mechanical alloying time. The S parameters are normalized to the bulk S value of the sample with 10 h alloying time. The dashed line is exponential decay fit to the data points and for the purpose of guiding to the eye only

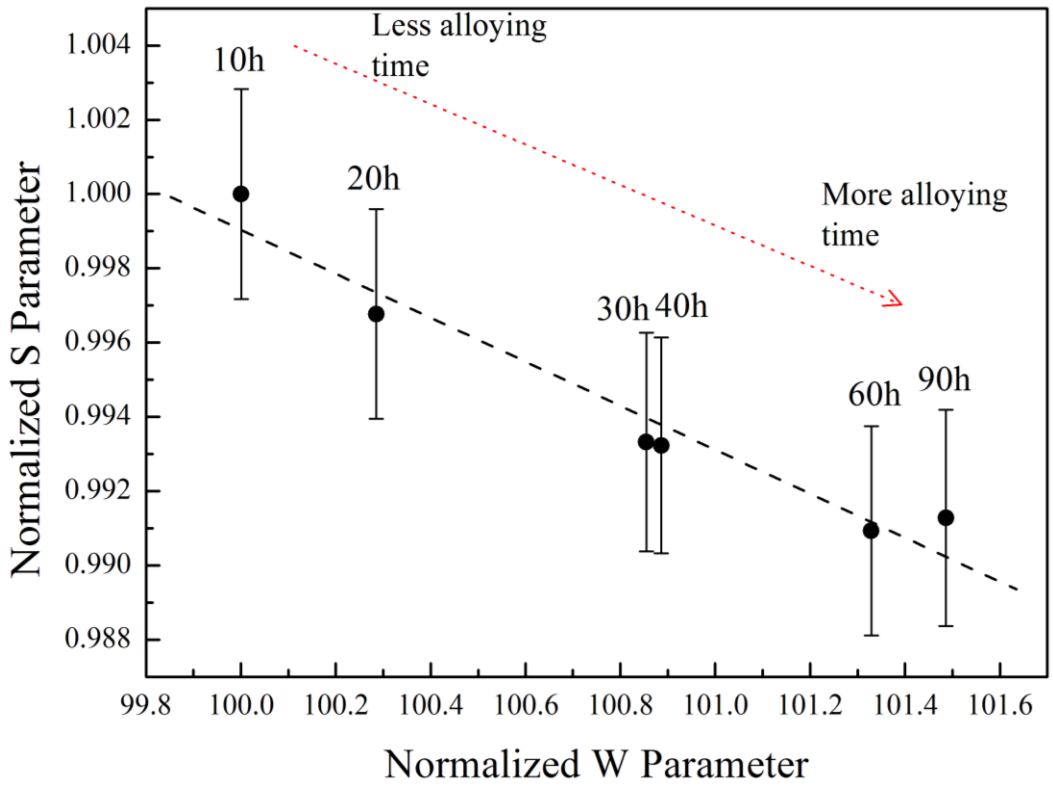

Figure 4.6 S-W map of characteristic (S, W) points of samples with varying alloying time. The S and W parameters are normalized to the bulk values of sample with 10 h alloying time. The dashed- line is a linear fit to the data points. The dotted arrow indicates the direction of changes of (S, W) points in the map.

4. 5 Effect of mechanical alloying on the magnetic properties

Hysteresis loops for the mechanically alloyed FeNi samples are shown in Figure 4.7. The magnetization curves show typical soft magnetic behavior with low coercivity, high permeability and moderate saturation magnetization. The phase is stable with increasing alloying time (as can be seen from XRD patterns), so constant M_s around 145 emu/g was as-expected. However, continuing decrease of relative permeability μ_r with internal strain was shown in Figure 4.8. μ_r decreased from around 1800 to 900 when

alloyed for ~20 h. With further alloying to 90 h, continuing decrease with lower decreasing rate was caused. μ_r is the maximum relative permeability calculated from ($\mu_r = B/H$) with applied field -20 to 20 kOe (as shown in the inset of Figure 4.8), showing the magnetic response function in magnetic materials. μ_r is sensitive to microstructure, and by extension, both strain and dislocation pinning. It has been shown that dislocation networks create periodic, localized stresses, which hinder the motion of the domain walls[32], causing an increase in coercive force and a decrease in relative permeability.

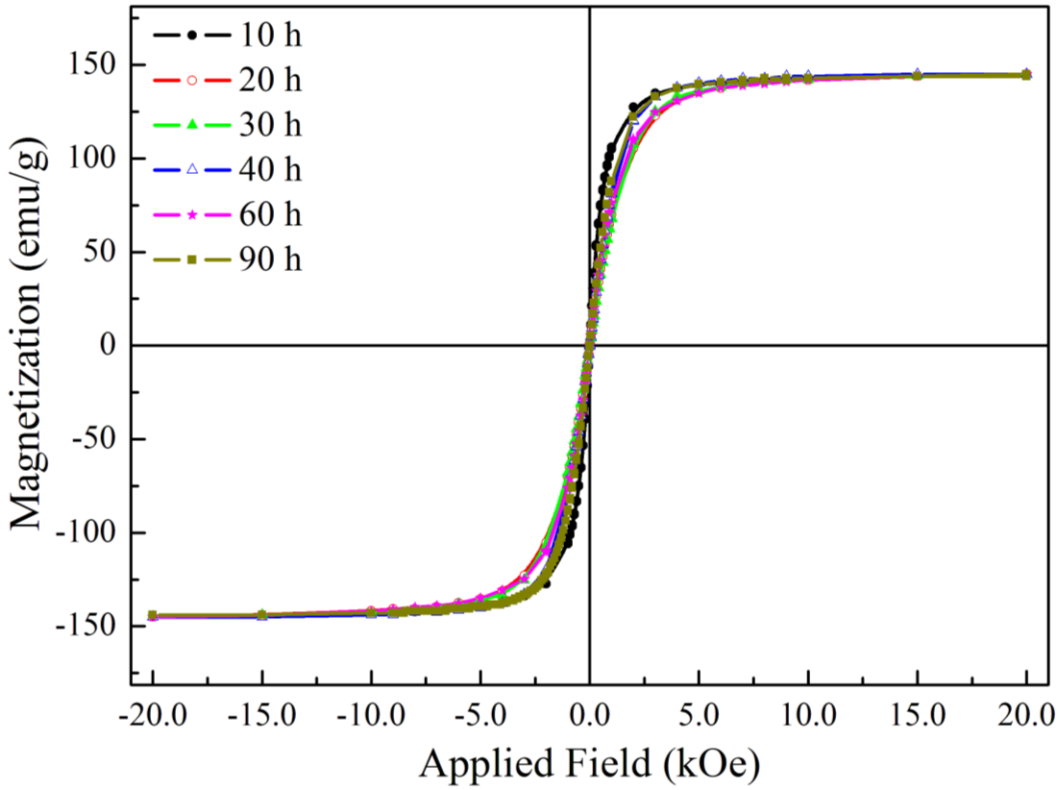

Figure 4.7 Hysteresis loop for FeNi mechanically alloyed for variable time

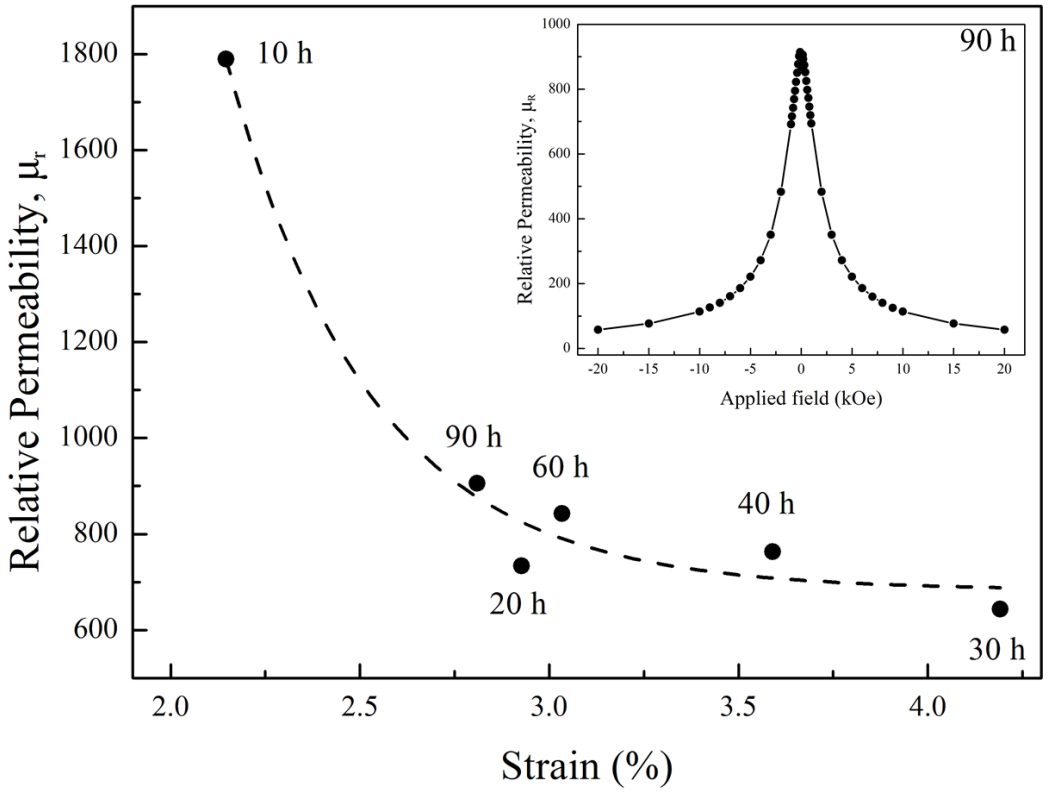

Figure 4.8 Relative permeability μ_r versus strain

4. 6 Conclusion

High-energy mechanical alloying was used to produce equiatomic Fe-Ni alloy. Complete alloying was achieved after 10 hrs of mechanical alloying. The grain size reduced from 17 nm to 12 nm as alloying time increased, but more grain boundaries were produced. An initial increase in internal strain followed by a decrease with further alloying was introduced by the combined effect of excessive plastic deformation during alloying and the annihilation of dislocations at increasing grain boundaries. Decrease of the net defect (possibly vacancy, vacancy agglomerates and free volume etc.) concentrations with mechanical alloying was revealed by Doppler broadening positron annihilation spectroscopy, which is due to enhancement of internal homogeneity in the

alloy. Thus, mechanical alloying could not be used to generate more vacancies in Fe-Ni alloy. Furthermore, effect of mechanical alloying on magnetic properties in FeNi alloy was investigated. A decrease of relative permeability was obtained with increasing internal strain due to the pinning effect of dislocations.

References

1 Albertsen, J., Knudsen, J. & Jensen, G. Structure of taenite in two iron meteorites. *Nature* **273**, 453 (1978).

2 Clarke, R. S. & Scott, E. R. Tetrataenite; ordered FeNi, a new mineral in meteorites. *American Mineralogist* **65**, 624-630 (1980).

3 Albertsen, J. Tetragonal lattice of tetrataenite (ordered Fe-Ni, 50-50) from 4 meteorites. *Physica Scripta* **23**, 301 (1981).

4 Néel, L., Pauleve, J., Pauthenet, R., Laugier, J. & Dautreppe, D. Magnetic Properties of an Iron—Nickel Single Crystal Ordered by Neutron Bombardment. *Journal of Applied Physics* **35**, 873-876 (1964).

5 Nagata, T. & Funaki, M. Tetrataenite phase in Antarctic meteorites. *Memoirs of National Institute of Polar Research. Special issue* **46**, 245-262 (1987).

6 Buchwald, V. F. *Handbook of iron meteorites: Their history, distribution, composition and structure*. Vol. 3 (University of California Press Berkeley, 1975).

7 Shima, T., Okamura, M., Mitani, S. & Takanashi, K. Structure and magnetic properties for L1< sub> 0</sub>-ordered FeNi films prepared by alternate monatomic layer deposition. *Journal of Magnetism and Magnetic Materials* **310**, 2213-2214 (2007).

8 Mizuguchi, M., Sekiya, S. & Takanashi, K. Characterization of Cu buffer layers for growth of L1 0-FeNi thin films. *Journal of Applied Physics* **107**, 09A716-709A716-713 (2010).

9 Mizuguchi, M., Kojima, T., Kotsugi, M., Koganezawa, T., Osaka, K. & Takanashi, K. Artificial fabrication and order parameter estimation of $L1_0$-ordered FeNi thin film grown on a AuNi buffer layer. *Journal of the Magnetics Society of Japan* **35**, 370-373 (2011).

10 Kojima, T., Mizuguchi, M. & Takanashi, K. in *Journal of Physics: Conference Series.* 012119 (IOP Publishing).

11 Kojima, T., Mizuguchi, M., Koganezawa, T., Osaka, K., Kotsugi, M. & Takanashi, K. Magnetic Anisotropy and Chemical Order of Artificially Synthesized $L1_0$-Ordered FeNi Films on Au–Cu–Ni Buffer Layers. *Japanese Journal of Applied Physics* **51**, 010204 (2012).

12 Was, G. S. *Fundamentals of radiation materials science*. (Springer, 2007).

13 Nagesha, K., Rajanish, M. & Shivappa, D. A Review On Mechanical Alloying. *change* **3** (2013).

14 Collins, G. S. & Sinha, P. in *Materials Science Forum.* 275-280 (Aedermannsdorf, Switzerland: Trans Tech Publications, 1984-).

15 Peng, L. S. & Collins, G. S. in *Materials Science Forum.* 537 (Aedermannsdorf, Switzerland: Trans Tech Publications, 1984-).

16 Coleman, P. G. *Positron beams and their applications*. (World Scientific, 2000).

17 Schaefer, H.-E., Würschum, R., Schwarz, R., Slobodin, D. & Wagner, S. Amorphous hydrogenated silicon studied by positron lifetime spectroscopy. *Applied Physics A* **40**, 145-149 (1986).

18 Nagel, C., Rätzke, K., Schmidtke, E., Faupel, F. & Ulfert, W. Positron-annihilation studies of free-volume changes in the bulk metallic glass Zr 65 Al 7.5 Ni 10 Cu 17.5 during structural relaxation and at the glass transition. *Physical Review B* **60**, 9212 (1999).

19 Nagel, C., Rätzke, K., Schmidtke, E., Wolff, J., Geyer, U. & Faupel, F. Free-volume changes in the bulk metallic glass Zr 46.7 Ti 8.3 Cu 7.5 Ni 10 Be 27.5 and the undercooled liquid. *Physical Review B* **57**, 10224 (1998).

20 Flores, K., Suh, D., Dauskardt, R., Asoka-Kumar, P., Sterne, P. & Howell, R. Characterization of free volume in a bulk metallic glass using positron annihilation spectroscopy. *Journal of Materials Research* **17**, 1153-1161 (2002).

21 Kanungo, B. P., Glade, S. C., Asoka-Kumar, P. & Flores, K. M. Characterization of free volume changes associated with shear band formation in Zr-and Cu-based bulk metallic glasses. *Intermetallics* **12**, 1073-1080 (2004).

22 Rehmet, A., Günther-Schade, K., Rätzke, K., Geyer, U. & Faupel, F. Quenching rate dependence of free volume in a Zr-Cu-Ni-Ti-Be glass as probed by positron annihilation lifetime spectroscopy. *physica status solidi (a)* **201**, 467-470 (2004).

23 Vallery, R., Liu, M., Gidley, D., Launey, M. & Kruzic, J. Characterization of fatigue-induced free volume changes in a bulk metallic glass using positron annihilation spectroscopy. *Applied Physics Letters* **91**, 261908-261908-261903 (2007).

24 Zhang, S., Schut, H., Brück, E., Van der Zwaag, S. & Van Dijk, N. in *Journal of Physics: Conference Series*. 012027 (IOP Publishing).

25 Williamson, G. & Hall, W. X-ray line broadening from filed aluminium and wolfram. *Acta Metallurgica* **1**, 22-31 (1953).

26 Wilson, A. X-ray optics, Methuen & Co. *Ltd., London* (1949).

27 Eckert, J., Holzer, J., Krill iII, C. & Johnson, W. Mechanically driven alloying and grain size changes in nanocrystalline Fe-Cu powders. *Journal of Applied Physics* **73**, 2794-2802 (1993).

28 Hirth, J. P. The influence of grain boundaries on mechanical properties. *Metallurgical transactions* **3**, 3047-3067 (1972).

29 Benjamin, J. & Volin, T. The mechanism of mechanical alloying. Uetall. *Trans.*~ **34** (1929).

30 Clement, M., De Nijs, J., Balk, P., Schut, H. & Van Veen, A. Analysis of positron beam data by the combined use of the shape-and wing-parameters. *Journal of Applied Physics* **79**, 9029-9036 (1996).

31 Liszkay, L., Corbel, C., Baroux, L., Hautojärvi, P., Bayhan, M., Brinkman, A. & Tatarenko, S. Positron trapping at divacancies in thin polycrystalline CdTe films deposited on glass. *Applied Physics Letters* **64**, 1380-1382 (1994).

32 Dubinko, S., Nedviga, A., Vishnevskii, V., Shaposhnikov, A., Yagupov, V., Nesteruk, A. & Prokopov, A. Features of the coercivity of strained epitaxial garnet ferrite films. *Technical Physics Letters* **31**, 979-981 (2005).

Chapter 5 High-Energy Mechanical Milling-induced Crystallization in $Fe_{32}Ni_{52}Zr_3B_{13}$

In this chapter, Zr and B elements are added in the FeNi alloy to form amorphous glass $Fe_{32}Ni_{52}Zr_3B_{13}$ through rapid solidification process, which has a higher defect concentration than crystalline materials. High-energy mechanical milling was then applied to generate even more defects. However, $Fe_{32}Ni_{52}Zr_3B_{13}$ undergoes crystallization during the milling process. The resulting structure consists of face-centered cubic (fcc) FeNi and $Zr_3Ni_{20}B_6$ nanocrystallites. Structural evolution and defect analysis of as-solidified $Fe_{32}Ni_{52}Zr_3B_{13}$ ribbons with different milling time is investigated. From the differential thermal analysis (DTA) curve of amorphous ribbons, exothermic peaks were observed at 415 ℃ and 475 ℃ corresponding to the crystallization of fcc $Zr_3Ni_{20}B_6$ phase and fcc FeNi phase, respectively. However, high-energy mechanical milling induces the formation of FeNi within the first 2 h of mechanical milling. Further milling induces the crystallization of $Zr_3Ni_{20}B_6$. Doppler broadening positron annihilation spectroscopy (DBPAS) was used to investigate vacancy-type defects. The milling-induced crystallization appears to be related to enhanced vacancy-type defect concentrations allowing growth of pre-existing Fe(Ni) nuclei. The milling and enhanced vacancy concentration also de-stabilizes the glass, leading to decreased crystallization temperatures for both phases, and ultimately eliminating the glass transition altogether.

5. 1 Introduction

Nanocrystalline materials are widely studied due to their large fraction of atoms residing at grain boundaries, large fractions of interfaces, and the resulting properties that often differ from those observed in bulk alloys[1]. Preparation and characterization of nanocrystalline materials continue to attract significant attention[2]. Mechanical milling is a well-known process for producing several different types of materials, including amorphous alloy powders, nanocrystalline powders, intermetallic compounds, composite and nanocomposite materials, and nanoparticles[3]. Excessive plastic deformation of the powder particles and cold welding between particles occurs during mechanical milling. These processes can be controlled by various milling parameters (e.g., the ratio of the mass of the balls to that of the starting material, hardness and dimension of the balls, milling intensity, milling time, or milling temperature)[4].

Crystallization of amorphous structures can be induced by heat treatment, irradiation, or other energy-transferring processes. Milling-induced crystallization was first reported by Trudeau, et al.[5-7] in a Fe-based amorphous alloy during high-energy mechanical milling. They explained that the milling-induced crystallization was due to a local increase in diffusion, enabled by the presence of nuclei in the materials. Also, the effect of mechanical milling on thermal crystallization kinetics in an amorphous FeMoSiB alloy was studied[5]. A decrease in the crystallization temperature and depression of activation energies compared to the as-solidified amorphous alloys was observed[8-11]. In the last two decades, milling-induced crystallization was reported in several other amorphous alloys[12-14]. However, the exact mechanism of milling-induced

crystallization is still controversial, with several mechanisms proposed. These include impurity incorporation during milling[15], creation of structural defects[15], deformation-induced processes[16], and local temperature excursions during milling[17]. α-Fe contamination was observed in the crystallization of $Fe_{64.5}Co_{18}Si_1B_{16}C_{0.5}$ under mechanical milling[18], while NiZr alloy formed as the result of the diffusion of Ti through dislocations and grain boundaries in α-Fe and by the migration of lattice and point defects generated by plastic deformation[15]. Local temperature excursions can enable an interdiffusion reaction during mechanical alloying of NiZr alloy[17], while a similar crystallization process and products ($Fe_{90}Zr_{10}$) under high-energy milling, low-energy milling, cryomilling and high-pressure torsion indicates the crystallization is induced by deformation[16]. Recently, the existence of quenched-in nuclei was proved to increase the rate of the crystallization process during mechanical milling[19-22]. In this chapter, amorphous $Fe_{32}Ni_{52}Zr_3B_{13}$, prepared by rapid solidification, was mechanically milled for different periods of time, with the structural and defect evolution studied to understand the milling-induced devitrification process[23].

5. 2 Experiment procedure

Alloy ingots were produced by arc melting high-purity (>99.97 %) Fe, Ni, Zr and B in an Ar atmosphere. $Fe_{32}Ni_{52}Zr_3B_{13}$ ribbons (~20 μm thick and ~2 mm wide) were prepared by rapid solidification in an Ar atmosphere through a single-roller melt spinner at a tangential wheel speed of 40 m/s. Differential thermal analysis (DTA) (Perkin Elmer DTA-7) at a heating rate of 5 ℃/min was utilized to determine thermal stability. Heat

treatment was conducted by sealing in quartz capsules after repeated evacuation/backfill cycles using UHP Ar. All heat treatment times were 24 h, followed by water quenching.

High-energy mechanical milling experiments were carried out with a SPEX 8000 Mixer/Mill for various periods of time. A cylindrical hardened steel vial and hardened steel balls of diameter 12.5 mm were used. The total mass of the balls was 35 g and the ball-to-sample weight ratio was kept (7~9):1. 5 g of ribbons were loaded into the vials and sealed in a nitrogen atmosphere glove box. 0.8 g powder was extracted after each milling and number of balls were changed so that the ball-to-sample weight ratio was in the range of 7~9. To reduce heating, the milling was done on an intermittent basis, with 5 minutes of milling followed by 5 minutes off. Total milling time was up to 16 h. X-ray diffraction was utilized to determine the phase evolution and was conducted using a Rigaku Multiflex using Cu-Kα radiation. Transmission electron microscopy samples were made by ion milling at 4.5 keV using a Precision Ion Polishing System from Gatan. An FEI Osiris operating at 200 kV was utilized for transmission electron microscopy.

Further structural information was obtained with Doppler broadening positron annihilation spectroscopy (DBPAS), in which monoenergetic positron beams with energies from several eV to 70 keV were implanted on samples. The mean implantation depth is a function of positron energy and density, where an implantation of positrons at 70 keV translates to ~4.4 μm in $Fe_{32}Ni_{52}Zr_3B_{13}$ samples. Annihilations of positrons with electrons release two γ rays with energies of 511 keV in opposite directions which were then detected by high purity Ge detectors with a resolution of 1.4 keV at 511 keV. The momentum component of the annihilating electron–positron pair parallel to the direction of the detected photon causes measurable Doppler shifts away from 511 keV and the sum

of many annihilation detections average out to a broadening of the annihilation line. Over one million counts were recorded at each energy step. The shape of the annihilation spectrum can be analyzed by line shape parameters *S* and *W*, where *S* is defined as the ratio of counts in the peak region of the spectrum to the total counts, whereas the *W* parameter is the ratio of counts in the wing (tail) region to the total counts. The *S* parameter represents the fraction of positrons annihilated mainly with the valance electrons and the *W* parameter represents the fraction of annihilations with core electrons with a large momentum component. When positrons annihilate after being trapped at vacancy-type defect sites, annihilation occurs predominantly with lower momentum electrons as opposed to the annihilation events occurred in the defect-free region where annihilation mostly comes from higher momentum electrons. As a result, open-volume defects produce higher *S* values compared to defect-free regions of the sample. The measured value of the *S* parameter is directly related to the size or concentration (or mix of both) of open-volume defects. A larger *S* value corresponds to a larger open-volume or higher vacancy-type defect concentration. The *W* parameter is mainly associated with the chemical environment of annihilation sites[24,25].

5. 3 Phase transformation under heat treatment

Fig. 5.1 shows X-ray diffraction patterns for the as-solidified amorphous $Fe_{32}Ni_{52}Zr_3B_{13}$ alloy. The as-solidified sample exhibits a diffuse X-ray diffraction peak characteristic of an amorphous phase; there is, however, a small peak at ~44 °shown from the peak deconvolution (inset of Fig. 5.1). The peak corresponds to the (111) peak for fcc FeNi and presumably arises from a small fraction of crystalline material that formed

during rapid solidification. This is corroborated by transmission electron microscopy, which revealed the coexistence of crystalline and amorphous phases (Fig. 5.2). The selected area electron diffraction pattern (inset of Fig. 5.2) reveals the diffuse diffraction rings typical of the diffraction pattern for amorphous phase, with the sharp reflections due to the crystalline phase. High resolution images revealed that the crystalline phase is the fcc FeNi phase (Fig. 5.2), as the Fast Fourier Transformation (FFT) was indexed to the [011] zone axis of the fcc FeNi structure.

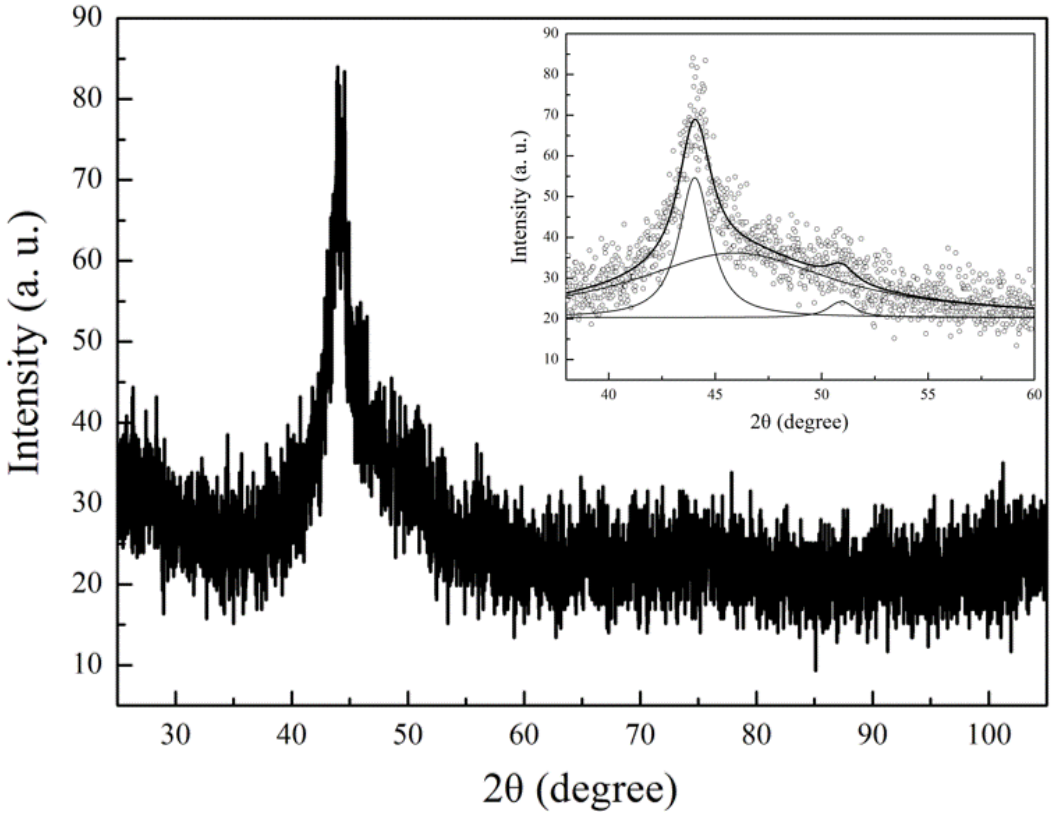

Figure 5.1 X-ray diffraction pattern for as-solidified $Fe_{32}Ni_{52}Zr_3B_{13}$

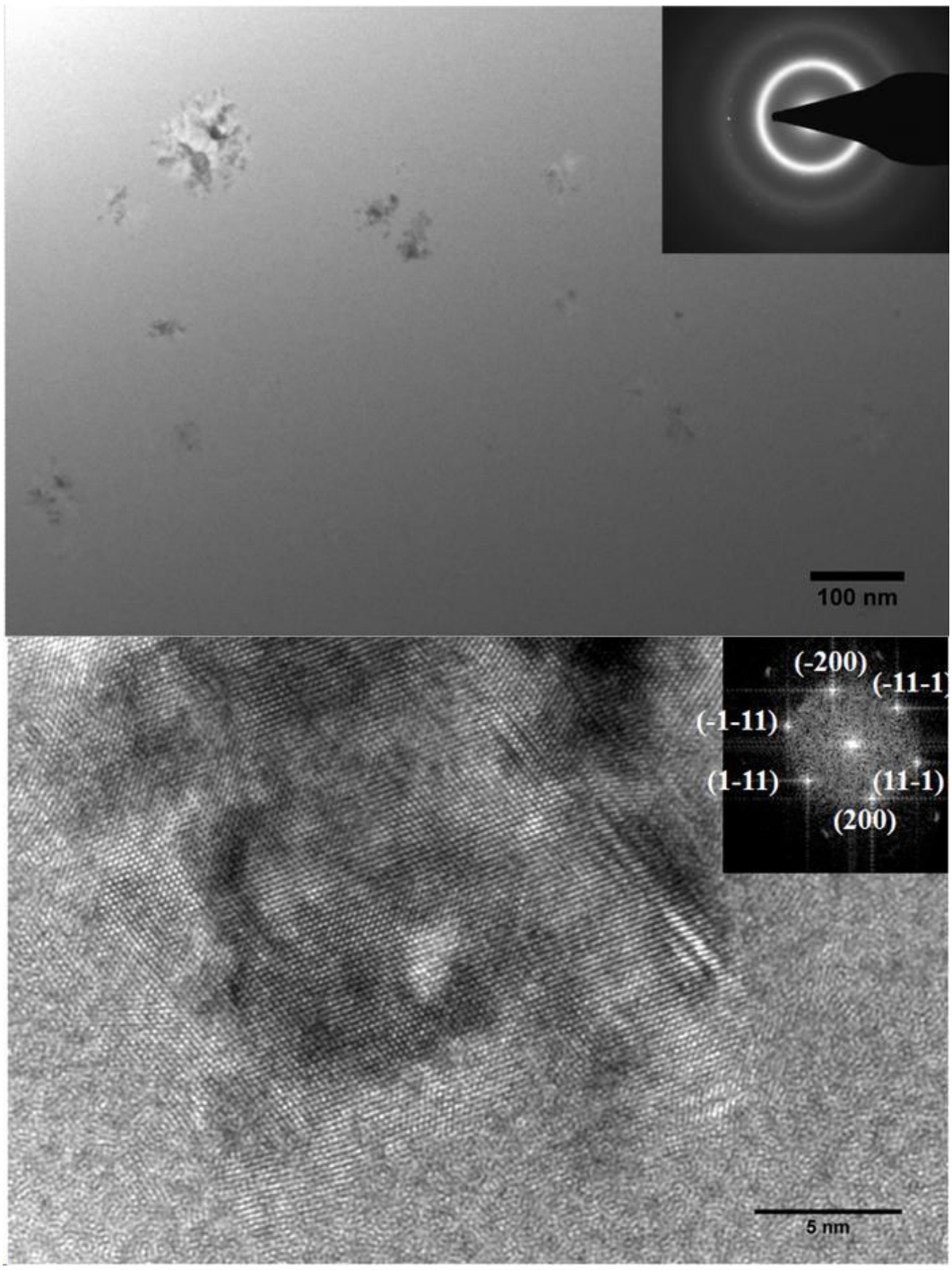

Figure 5.2 Transmission electron micrograph of as-solidified $Fe_{32}Ni_{52}Zr_3B_{13}$

The DTA thermogram for the as-solidified ribbon revealed two exothermic peaks at 415 ℃ and 475 ℃, respectively (Figure 5.3). In order to determine the crystallization

products corresponding to the DTA thermal events, isothermal heat treatment was carried out on as-solidified ribbons at temperatures just around the onset temperatures of the two peaks for 24 h. A face-centered cubic $Zr_3Ni_{20}B_6$ phase was observed after annealing at 420 ℃ for 24 h, while an additional face-centered cubic FeNi phase was observed after annealing at 470 ℃ for 24 h (Figure 5.4). Thus, the first exothermic peak corresponds to the crystallization of the $Zr_3Ni_{20}B_6$ phase, while the second peak corresponds to the crystallization of fcc FeNi. Grain growth of fcc FeNi phase during heat treatment at 420 ℃ was expected since the increase of nuclei during pre-anneal treatment was observed in amorphous Ni-P alloys [10]. The ratio of (111) peak intensity of the FeNi phase to (511) peak intensity of $Zr_3Ni_{20}B_6$ was calculated after peak deconvolution was applied (inset of Fig. 5.4 I and II). An increase from 0.62 to 1.09 was observed, confirming the fcc FeNi phase formation during heat treatment at 470 ℃. The position of (111) peak of fcc FeNi phase changes from 44.04 °in as-solidified alloy to 43.81 °after heat treatment at 420 ℃, which indicates the composition changes of fcc FeNi phase. Constant position of (111) peak from fcc FeNi phase after heat treatment at 470 ℃ shows the same composition from that of as-solidified alloy.

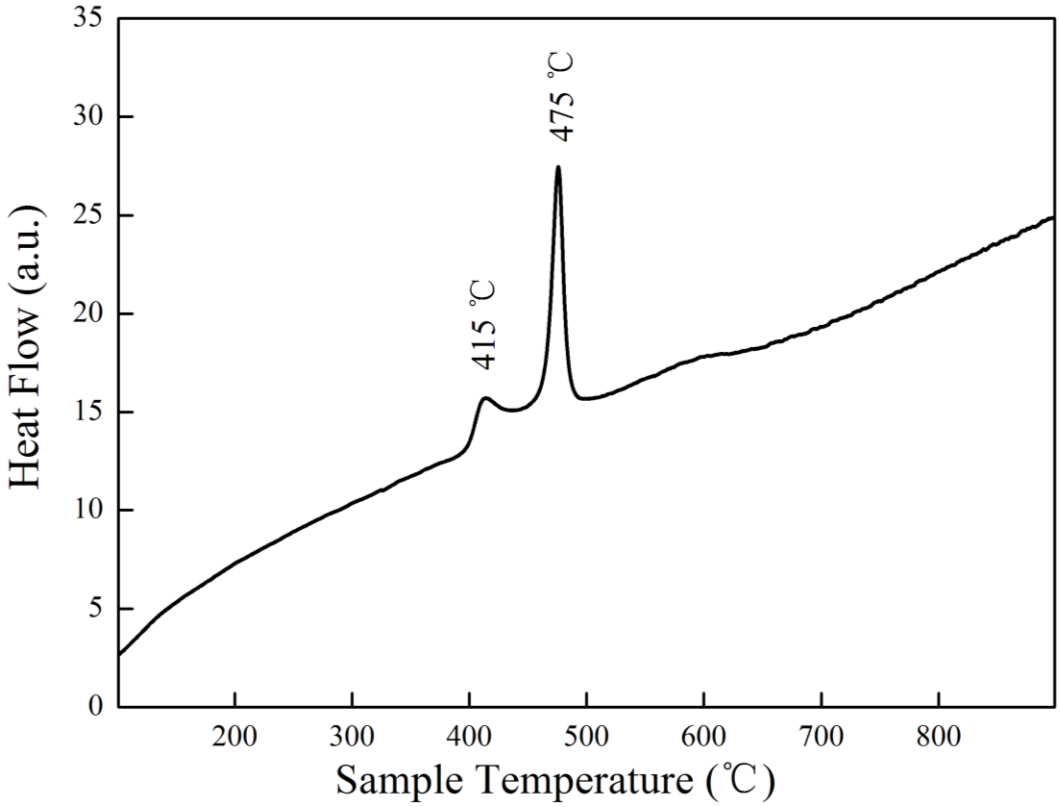

Figure 5.3 DTA thermogram for as-solidified $Fe_{32}Ni_{52}Zr_3B_{13}$ alloy

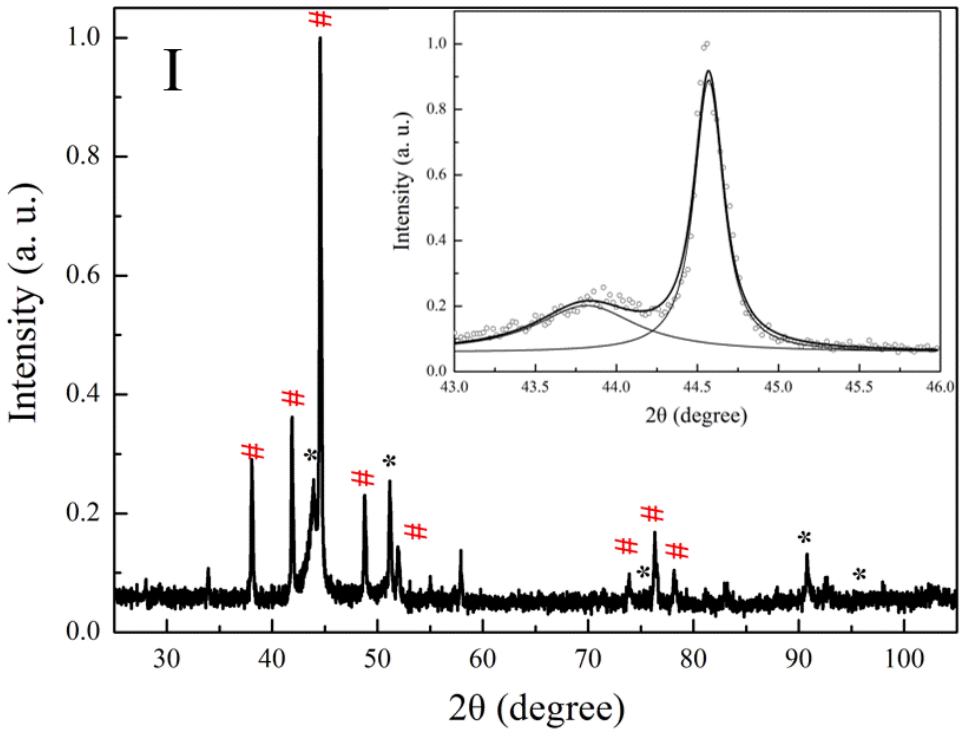

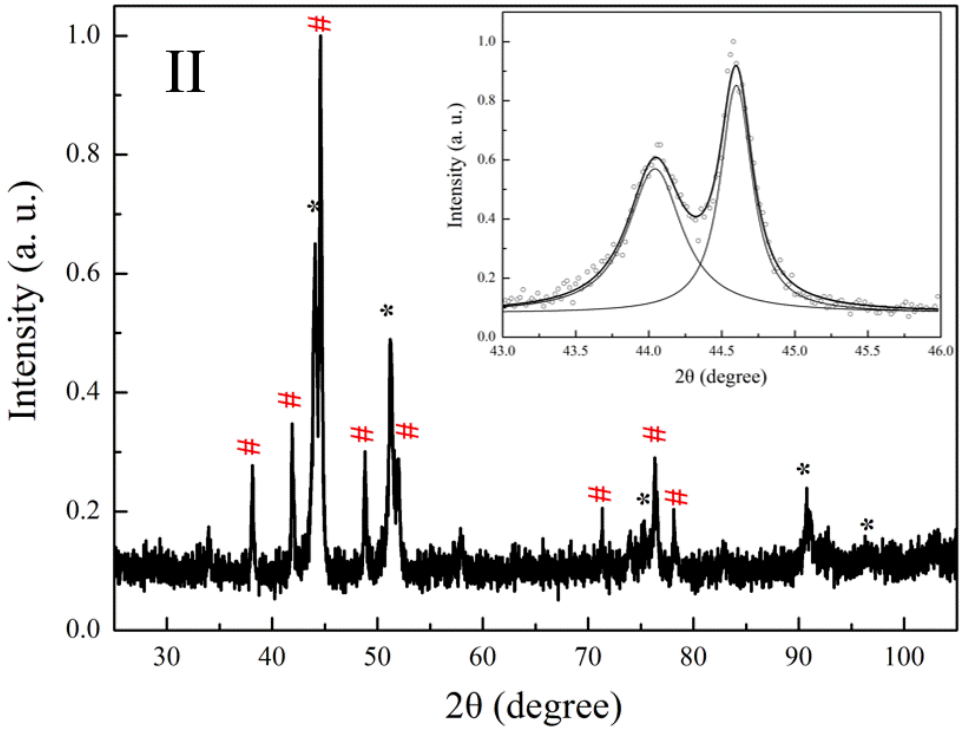

Figure 5.4 X-ray diffraction pattern for I: heat treated $Fe_{32}Ni_{52}Zr_3B_{13}$ at 420 ℃ for 24 h; II: heat treated $Fe_{32}Ni_{52}Zr_3B_{13}$ at 470 ℃ for 24 h (#: $Zr_3Ni_{20}B_6$; *: FeNi)

5. 4 Phase transformation under mechanical milling

Mechanical milling was shown to significantly affect the crystallization process, as shown by the changes in the DTA thermograms as a function of milling time (Figure 5.5). After 30 min of milling, the high-temperature tail of the first crystallization peak has merged with the second crystallization peak, while the intensity (enthalpy) of the second peak has decreased. After 1 h of milling, the first peak has increased dramatically in intensity, but the onset is approximately the same. The second peak is evident but very weak. After 2 h of milling, the second peak is absent and the first peak has shifted to a lower temperature. With further milling to 4 h, the exothermic peak decreases in both intensity and onset temperature. After 8 h of milling, no exothermic peak exists.

The x-ray diffraction results with milling time mirror the DTA results. The diffraction peaks corresponding to the fcc FeNi phase become sharper as milling time increases, and after milling for 4 h peaks associated with the fcc $Zr_3Ni_{20}B_6$ phase become evident (Figure 5.6). With further milling diffraction peaks for both phases become more apparent. Thus, the final phase mixture is similar to that observed after heat treatment, but the peak widths after milling-induced crystallization are much broader, reflecting the strain induced by mechanical milling.

The milling-induced crystallization process is much different than the thermally induced crystallization process. With thermal crystallization, the fcc $Zr_3Ni_{20}B_6$ was the first to crystallize, followed by the fcc FeNi. During mechanical milling, the FeNi phase crystallized first, as evidenced by the decreasing intensity, and then disappearance, of the second (higher temperature) exothermic peak that was associated with the fcc FeNi formation, as well as the increasing intensity of the FeNi x-ray peaks. The final phase to crystallize during milling was the $Zr_3Ni_{20}B_6$, as shown in Figure 5.6. Additionally, a sample milled for 4 h, the time corresponding to the disappearance of the higher-temperature exotherm, was heat treated just above the remaining exotherm. This resulted in the formation of the $Zr_3Ni_{20}B_6$ phase as shown in Figure. 5.7.

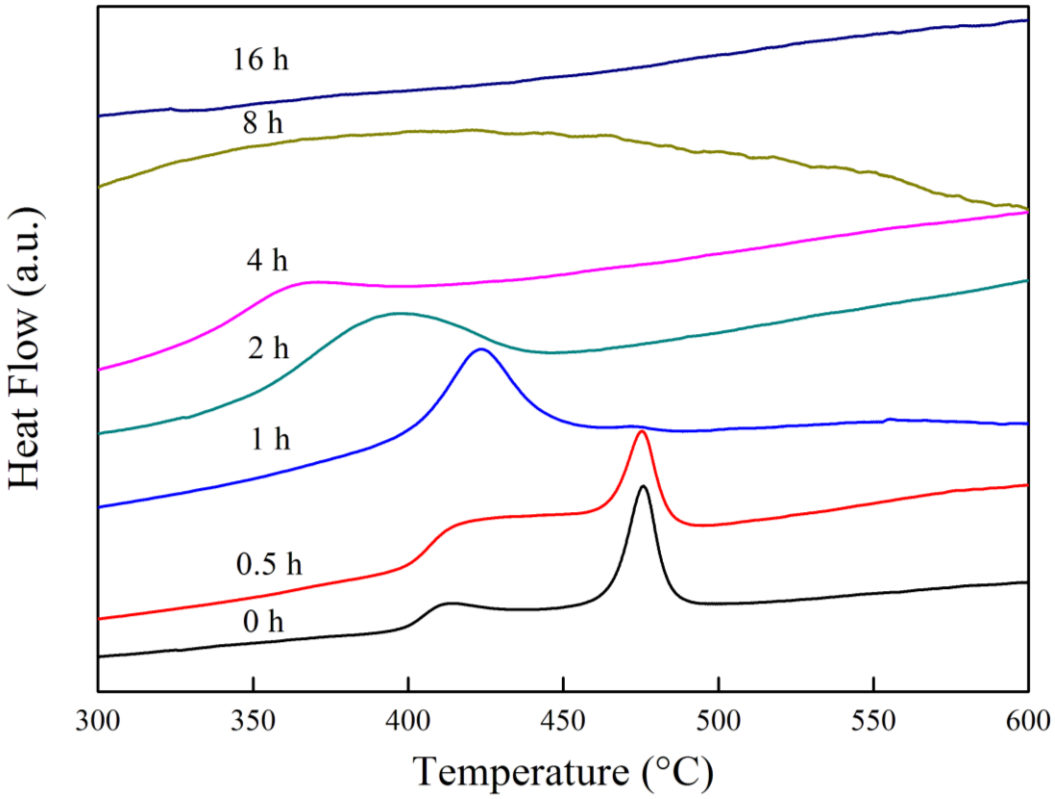

Figure 5.5 DTA curves for $Fe_{32}Ni_{52}Zr_3B_{13}$ alloy after mechanical milling for different periods of time

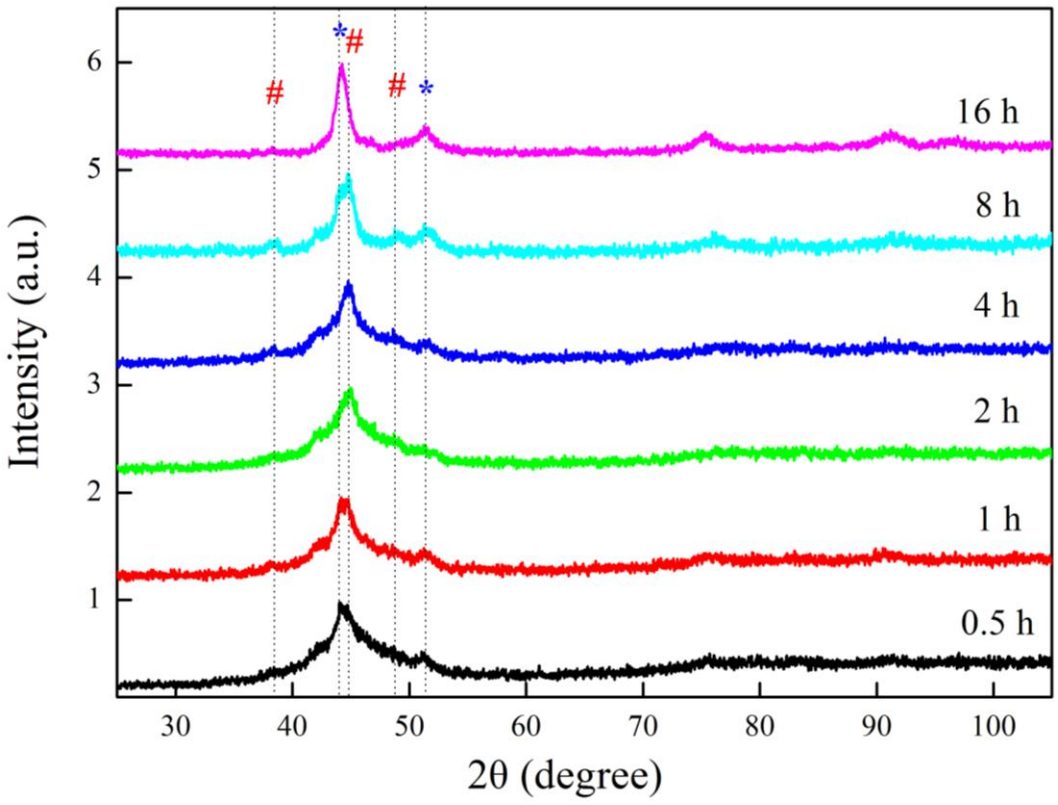

Figure 5.6 X-ray diffraction patterns for $Fe_{32}Ni_{52}Zr_3B_{13}$ with different milling time from 0.5 h to 16 h (# are (422), (511) and (440) peaks from face-centered cubic $Zr_3Ni_{20}B_6$; * are (111) and (200) peaks from face-centered cubic FeNi)

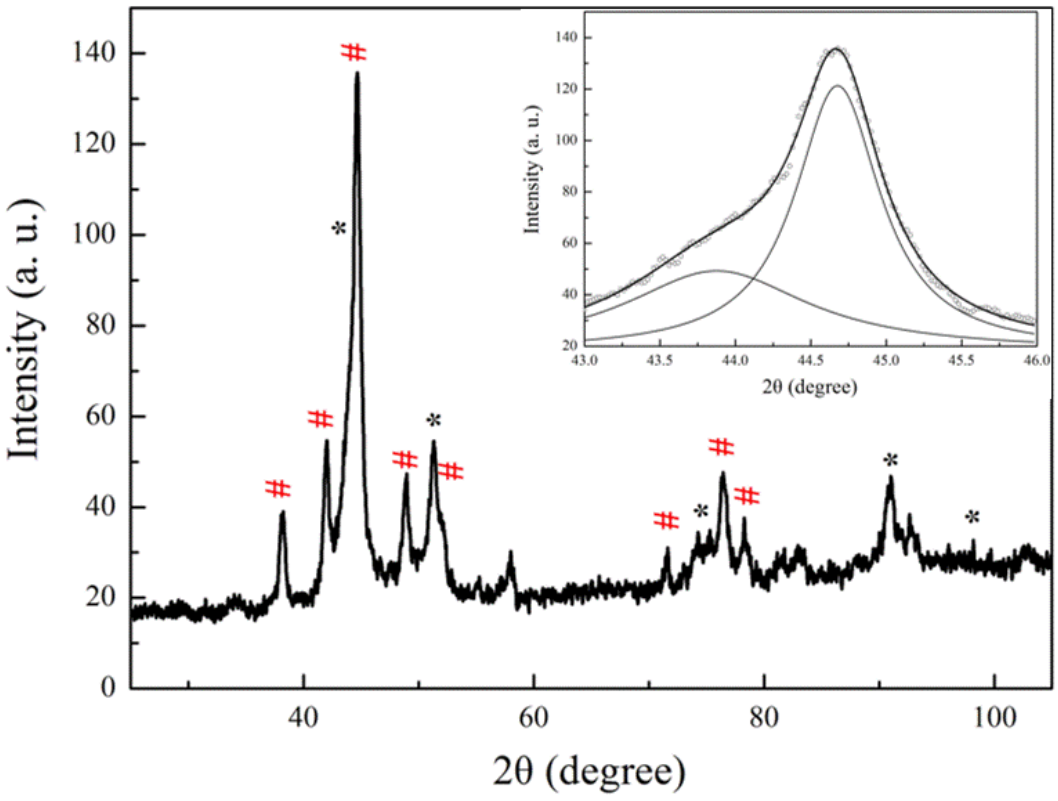

Figure 5.7 X-ray diffraction patterns for $Fe_{32}Ni_{52}Zr_3B_{13}$ after mechanical milling for 4 h and then heat treatment at 360 ℃ for 24 h

5. 5 Defects investigation using Positron Annihilation Spectroscopy

Earlier work suggested that milling-induced defects such as dislocations and grain boundaries create high-diffusivity paths, enabling crystallization[25]. Here, the defects were investigated by PAS. The Fig. 5.8 shows the *S* parameters with error bars as a function of milling time where the *S* values at each milling time were obtained by averaging out respective *S* values over the energies from 30 keV to 70 keV. , the data is normalized to the *S* value of the sample with 0.5 h milling time, where $S_{0.5h} = 0.4189$.

One can see that no change in *S* is observed from sample with 0.5h milling to 1h milling time indicating these two samples have nearly similar open-volume concentration. An increase of 0.5h in milling time didn't produce noticeable changes in open-volumes. When milling time was increased from 1h to 2h, there is nearly 1% increase in *S* value indicating open-volume defects were induced. Furthermore, when the milling time gradually increased from 2h to 16h, the *S* parameter appears to be increasing linearly with milling time. There are ~2% and ~4% increase in *S* from 0.5h milling time to 8 h and 16 h milling time, respectively. This observation can be explained by assuming that open-volume defects were created by high energy milling of more than 1 hour duration and the concentration of the defects is linearly increased by increased milling time.

The nature of the open-volume defects induced by varying the milling time was further studied by investigating the relationship between *S* and *W* parameters. In general, if the characteristic (*S, W*) points of samples fits to a straight line, it is indication that samples have the same kind of defects[26,27]. The Fig. 5.9 shows the valence annihilation parameter, *S*, as a function of the core annihilation parameter, *W*. As it can be seen, the characteristic (*S, W*) points of samples with varying milling time follow a straight line trend. The only imperfection is the (*S, W*) point of sample with 0.5h milling time, which is a little bit off from the best fit line. However, the data points for samples from 1h to 16h fit to a straight line indicating high energy milling induced same kind of open-volume defects and the concentration increases with milling time. This increased open-volume defect concentration enables the diffusion process. The fcc FeNi phase may preferably form via this mechanism because it is simpler in structure than is the $Zr_3Ni_{20}B_6$ phase. Similar results were observed in other systems when comparing the crystallization

process and products under high-energy milling, low-energy milling, cryomilling and high pressure torsion[16]. The increased vacancy concentration in $Zr_3Ni_{20}B_6$ results in the decrease of its crystallization onset temperatures observed in the DTA thermograms.

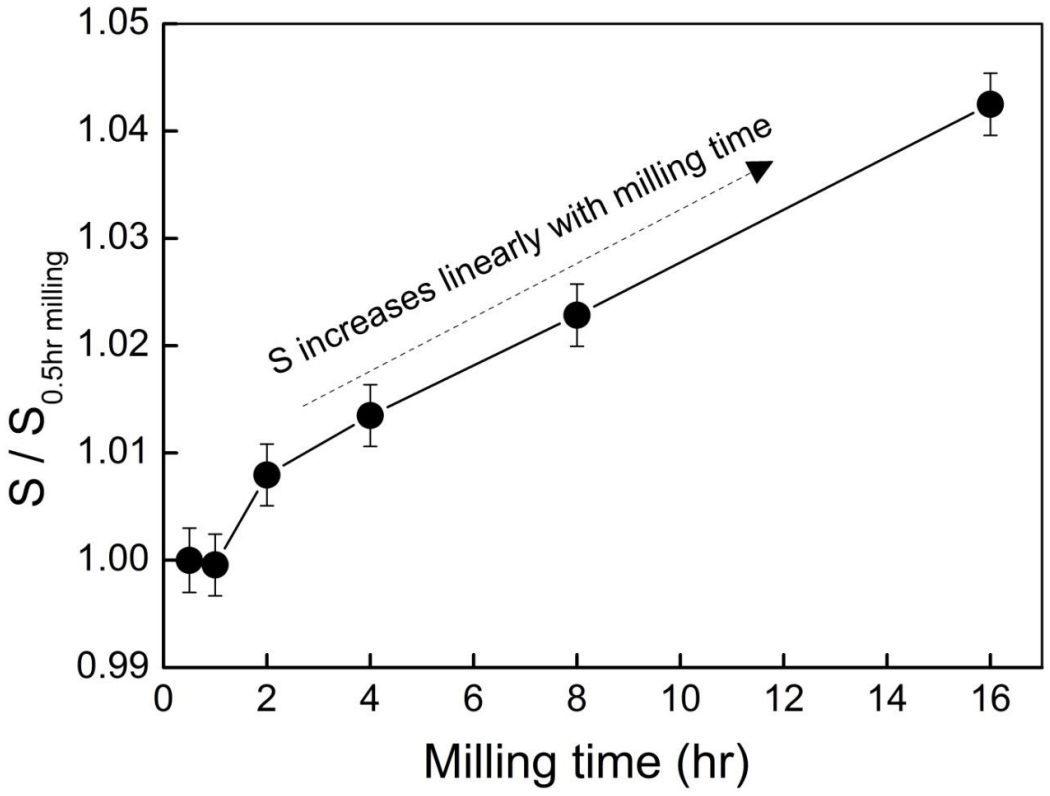

Figure 5.8 The *S* parameters of samples as a function of milling time. The *S* parameters are normalized to the bulk *S* value of the sample with 0.5h milling time. The solid lines between data points are guides to the eye. The dashed line indicates the direction of the changes in *S* as the milling time increased.

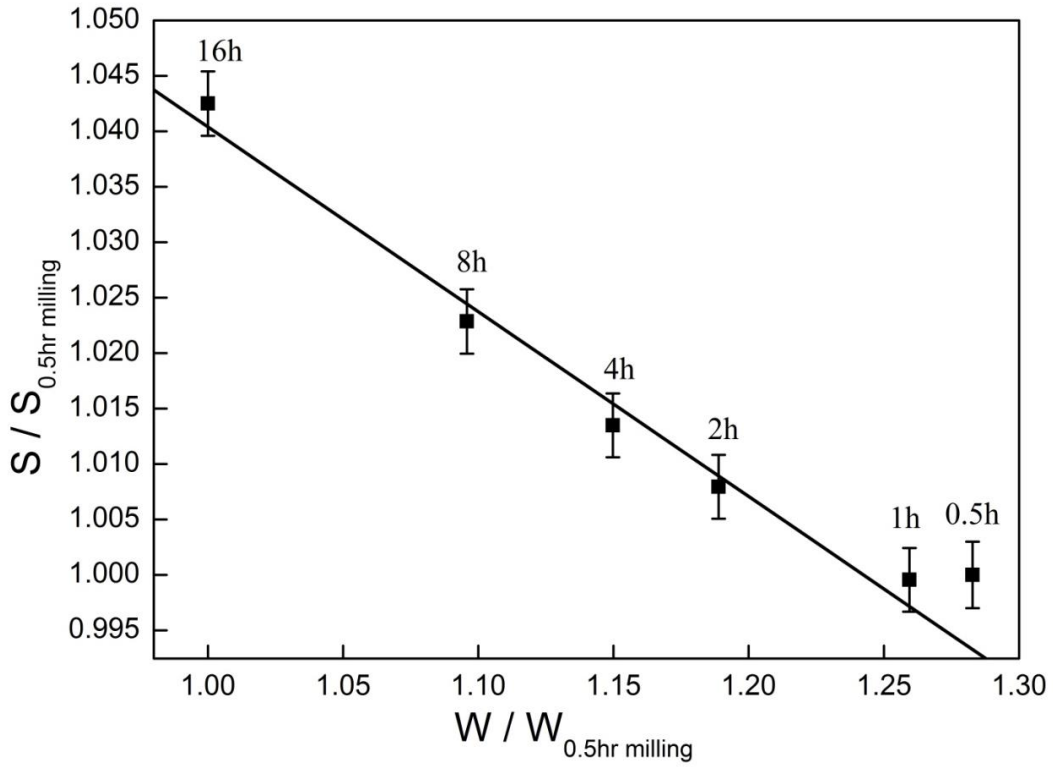

Figure 5.9 Normalized *S*-*W* parameter plots for varying milling time. The solid line is best fit line to data points.

5. 6 Conclusion

Crystallization of amorphous alloys normally follows the order of activation energy (crystallization temperature). However, during high-energy mechanical milling, FeNi phase with higher crystallization temperature crystallized earlier than $Zr_3Ni_{20}B_6$ phase with lower crystallization temperature, indicating milling-induced crystallization is a temperature-independent process. Meanwhile decrease of crystallization onset temperatures was observed due to pre-existed FeNi phase and increase of defects, which will reduce the thermal stability of the residual amorphous phase and increase the diffusion rate during heat treatment. It is also observed that high energy milling creates

open-volume defects in this material and their concentration increase linearly with milling time.

References

1 Suryanarayana, C. Nanocrystalline materials. *International Materials Reviews* **40**, 41-64 (1995).

2 Chakravorty, D., Giri, A. & Rao, C. Chemistry of advanced materials. *Ed. Rao, CNR Boca Raton, FL: Blackwell Scientific Publication* (1993).

3 Zhang, D. Processing of advanced materials using high-energy mechanical milling. *Progress in Materials Science* **49**, 537-560 (2004).

4 Giri, A. K. Nanocrystalline materials prepared through crystallization by ball milling. *Adv Mater* **9**, 163-166 (1997).

5 Trudeau, M., Schulz, R., Dussault, D. & Van Neste, A. Structural changes during high-energy ball milling of iron-based amorphous alloys: Is high-energy ball milling equivalent to a thermal process? *Physical Review Letters* **64**, 99 (1990).

6 Trudeau, M., Huot, J., Schulz, R., Dussault, D., Van Neste, A. & L'Espérance, G. Nanocrystalline Fe-(Co, Ni)-Si-B: The mechanical crystallization of amorphous alloys and the effects on electrocatalytic reactions. *Physical Review B* **45**, 4626 (1992).

7 Trudeau, M. Deformation induced crystallization due to instability in amorphous FeZr alloys. *Applied Physics Letters* **64**, 3661-3663 (1994).

8 Guo, F. & Lu, K. Ball-milling-induced crystallization and ball-milling effect on thermal crystallization kinetics in an amorphous FeMoSiB alloy. *Metallurgical and Materials Transactions A* **28**, 1123-1131 (1997).

9 Lu, K. & Wang, J. Activation energies for crystal nucleation and growth in amorphous alloys. *Materials Science and Engineering: A* **133**, 500-503 (1991).

10 Lu, K. & Wang, J. Relationship between crystallization temperature and pre-existing nuclei in amorphous Ni P alloys. *Materials Science and Engineering* **97**, 399-402 (1988).

11 Yao, B., Liu, S.-E., Liu, L., Si, L., Su, W.-H. & Li, Y. Mechanism of mechanical crystallization of amorphous Fe–Mo–Si–B alloy. *Journal of Applied Physics* **90**, 1650-1654 (2001).

12 Giri, A. K., Gonzalez, J. & Gonzalez, J. Crystallization by ball milling: a way to produce soft magnetic materials in powdered form. *Magnetics, IEEE Transactions on* **31**, 3904-3906 (1995).

13 Oleszak, D. & Shingu, P. H. Nanocrystalline metals prepared by low energy ball milling. *Journal of Applied Physics* **79**, 2975-2980 (1996).

14 Nowroozi, M. & Shokrollahi, H. The effects of milling time and heat treatment on the micro-structural and magnetic behavior of Fe42Ni28Zr8Ta2B10C10 synthesized by mechanical alloying. *Journal of Magnetism and Magnetic Materials* **335**, 53-58 (2013).

15 Schwarz, R., Petrich, R. & Saw, C. The synthesis of amorphous Ni Ti alloy powders by mechanical alloying. *Journal of Non-Crystalline Solids* **76**, 281-302 (1985).

16 Kwon, Y.-S. & Lee, H.-S. in *Strategic Technologies, 2008. IFOST 2008. Third International Forum on.* 153-156 (IEEE).

17 Eckert, J., Schultz, L. & Urban, K. Glass-forming ranges in transition metal-Zr alloys prepared by mechanical alloying. *Journal of the Less Common Metals* **145**, 283-291 (1988).

18 Bansal, C., Fultz, B. & Johnson, W. Crystallization of Fe B Si metallic glass during ball milling. *Nanostructured materials* **4**, 919-925 (1994).

19 Ipus, J., Bl ázquez, J., Franco, V. & Conde, A. Ball milling of Fe< sub> 83</sub> Zr< sub> 6</sub> B< sub> 10</sub> Cu< sub> 1</sub> amorphous alloy containing quenched in crystals. *Intermetallics* **15**, 1132-1138 (2007).

20 Ohkubo, T., Kai, H., Ping, D., Hono, K. & Hirotsu, Y. Mechanism of heterogeneous nucleation of α-Fe nanocrystals from Fe< sub> 89</sub> Zr< sub> 7</sub> B< sub> 3</sub> Cu< sub> 1</sub> amorphous alloy. *Scripta Materialia* **44**, 971-976 (2001).

21 Bl ázquez, J., Franco, V. & Conde, A. The influence of Cu addition on the crystallization and magnetic properties of FeCoNbB alloys. *Journal of Physics: Condensed Matter* **14**, 11717 (2002).

22 Sparchez, Z., Chicinas, I., Isnard, O., Pop, V. & Popa, F. Mechanical alloying of Ni< sub> 3</sub> Fe in the presence of Ni< sub> 3</sub> Fe nanocrystalline germs. *Journal of Alloys and Compounds* **434**, 485-488 (2007).

23 Geng, Y., Ablekim, T., Mukherjee, P., Weber, M., Lynn, K. & Shield, J. E. High-energy mechanical milling-induced crystallization in Fe< sub> 32</sub> Ni< sub>

52</sub> Zr< sub> 3</sub> B< sub> 13</sub>. *Journal of Non-Crystalline Solids* **404**, 140-144 (2014).

24 Schultz, P. J. & Lynn, K. G. Interaction of positron beams with surfaces, thin films, and interfaces. *Reviews of Modern Physics* **60**, 701 (1988).

25 Zhang, S., Schut, H., Brück, E., Van der Zwaag, S. & Van Dijk, N. in *Journal of Physics: Conference Series*. 012027 (IOP Publishing).

26 Clement, M., De Nijs, J., Balk, P., Schut, H. & Van Veen, A. Analysis of positron beam data by the combined use of the shape-and wing-parameters. *Journal of Applied Physics* **79**, 9029-9036 (1996).

27 Liszkay, L., Corbel, C., Baroux, L., Hautojärvi, P., Bayhan, M., Brinkman, A. & Tatarenko, S. Positron trapping at divacancies in thin polycrystalline CdTe films deposited on glass. *Applied Physics Letters* **64**, 1380-1382 (1994).

Chapter 6 Phase transformation and magnetic properties of rapidly solidified MnAl alloys modified with Zr, Hf and C addition

Near-equiatomic $L1_0$-type MnAl and structurally stabilized MnAlC compounds containing interstitial carbon hold promise as an advanced permanent magnet due to their high coercivity values, moderately high energy product, large corrosion resistivity, and low cost[1]. In this chapter, optimization of magnetic properties in MnAl alloys by composition modification and microstructure control would be conducted.

As discussed in Chapter 2, intrinsic properties, including magnetocrystalline anisotropy constant, saturation magnetization, Curie temperature etc., could be adjusted through different alloying elements, composition, and crystal structure. Meanwhile, extrinsic properties, notably coercivity and remanence, could be enhanced by microstructure modification through different processing techniques. In this chapter, the Zr, Hf and C modified Mn-Al-C alloys were produced through melt-spinning followed by subsequent heat treatment. The changes of saturation magnetization and coercivity based on different composition will be covered.

6. 1 Introduction

Mn-Al-based permanent magnets, free from rare-earth elements, exhibit an excellent combination of magnetic and mechanical properties[1,2]. Due to the presence of

the intermetallic tetragonal phase (τ phase), it shows strong, uniaxial magnetocrystalline anisotropy energy with an "easy" c-axis. The τ phase is typically formed by quenching the high-temperature antiferromagnetic ε phase (hcp) followed by heat treatment at 450–600 ℃[3-5]. Since the τ phase is metastable, prolonged annealing at elevated temperatures can lead to the transformation of τ phase to the stable but nonmagnetic γ (Al_8Mn_5) and β (Mn) phases[6]. The addition of a small amount of carbon into the MnAl alloy can stabilize the τ phase and inhibits the decomposition of the τ phase[7,8]. In C-doping Mn-Al alloy, the highest coercivity was obtained for carbon content just above the solubility limit of carbon atoms[9-11]. Thus, the composition of $Mn_{54}Al_{43}C_3$ was used as reference composition in this research.

One shortfall of the τ- phase MnAl is its lower saturation magnetization, especially compared to Fe- or Co-based permanent magnets. While the Al layer in the $L1_0$ structure effectively increases the Mn-Mn distances, resulting in ferromagnetic coupling, its presence dilutes the magnetization. Further, the $L1_0$ phase in this system is hyperstoichiometric relative to Mn, as the minimum Mn content is governed by the composition of the ε phase from which τ forms. In τ phase $Mn_{54}Al_{46}$, 4% of the Mn atoms occupy Al sites, which couple antiferromagnetically with the Mn layers, resulting in a decrease in the saturation magnetization over stoichiometrically perfect $L1_0$[1]. Therefore, one approach to substitutional alloying is to target the Mn atoms in the Al layer, as replacing them with non-magnetic atoms would effectively increase the magnetization. Alloying effects of several elements including Ti, Ni, Zn, Cu, B, Dy and Pr in Mn-Al alloy have been studied[12-15]. A decrease in magnetization and constant coercivity was observed with a Ni addition[12]; an enhancement of coercivity from 1 kOe to 3 kOe and

reduction in magnetization was caused by the addition of B[12]; the phase transformation to τ was depressed by addition of Ti[12]; and Cu showed no influence on the magnetic properties of Mn-Al alloys[12]. A Mn-Al-Zn alloys, prepared by water quenching the induction-melted alloy followed by heat treatment at 420℃ for 1 hr, showed an initial increase in magnetization at low Zn content, and then a decrease at Zn additions more than 1.6 at.%. However, the overal magnetization of these Mn-Al alloys was as low as ~15 emu/g, compared to ~100 emu/g produced with other processing[1]. Substitution of rare-earth elements Pr and Dy slightly improved the magnetic properties, and the anisotropy constant enhancement was attributed to either the 3d–4f electron interactions or simply the increase in atomic distance between Mn atoms. However, the alloying effect of Zr element in MnAl system has never been studied. Therefore, introduction of Zr element into $Mn_{54}Al_{43}C_3$ was investigated in this research.

6. 2 Experiments Procedure

All ingots were prepared by arc melting high-purity (>99.97%) Mn, Al, C, Hf and Zr elements in an Ar atmosphere. Melt spun ribbons with composition $Mn_{54-x}Al_{43}C_3Zr_x$ (x=0,1, 3), $Mn_{54-y}Al_{43}C_3Hf_y$ (y=0,1, 3) and $(Mn_{53}Al_{43}C_3Zr_1)_{100-z}C_z$ (with z=1, 3, 5, 7) were obtained by rapid solidification through a single-roller melt spinner at a tangential wheel speed of 40 m/s. To ensure homogeneity during further processing and measurement, the as-solidified ribbons were hand-grinded in a mortar and pestle into powders. Heat treatment was conducted at 500 ℃ by sealing in quartz capsules after repeated evacuation/backfill cycles using UHP Ar followed by water quenching to retain

the τ phase. In order to follow the kinetics of the τ-phase formation and decomposition, each sample was annealed for a series of time increased from 10 min to 60 min.

Microstructural characterization was performed by X-ray diffraction (XRD) (Rigaku Multiflex with Cu-Kα radiation) while the data collection for Retrieve Refinement was conducted on Rigaku D Max B with Co (λ=1.78897 Å) radiation. To minimize background, an off-cut single-crystal Si slide was used as a sample holder. The lattice parameters were determined from the retrieve refinement of the XRD data using TOPAS (Total Pattern Analysis Solution, Bruker AXS). To determine the magnetic properties, the powders were embedded in epoxy resin and measured at room temperature using a Quantum Design Magnetic Property Measurement System (MPMS) superconducting quantum interference device magnetometer (SQUID) under a field of 7 T. No demagnetization correction was made for the magnetic measurements.

6. 3 Structural and magnetic properties of $Mn_{54}Al_{43}C_3$ alloys modified by Zr and Hf addition

6. 3. 1 Phase transformation in Zr-modified $Mn_{54}Al_{43}C_3$ alloys

XRD patterns for the as-solidified $Mn_{54-x}Al_{43}C_3Zr_x$ (x=0, 1, 3) samples were indexed to mainly the ε phase (Fig. 6.1). A diffuse peak in the vicinity of 56° (2θ) indicates the presence of a second minor phase in the $Mn_{54-x}Al_{43}C_3(Zr)_x$ samples. Heat treatment at 500 ℃ was applied to all the as-solidified samples for 10 min, which, for $Mn_{54}Al_{43}C_3$, results in the formation of the τ phase[16]. XRD patterns for the annealed $Mn_{54-x}Al_{43}C_3Zr_x$ (x=0, 1, 3) revealed that the τ phase is the primary phase, while a small

fraction of ε and γ_2 phases were also observed (Fig. 6.2). The lattice parameters were calculated a=3.9122 Å, c=3.5975 Å. Compared to the lattice parameters for τ phase $Mn_{54}Al_{43}C_3$ (a=3.9014 Å, c=3.6337 Å), the c/a ratio decreased from 0.9314 to 0.9196. Transmission electron microscopy result showed a grain size of ~600 nm (Fig. 6.3). When the Zr content was increased to 3 at.%, formation of τ phase was suppressed. Instead, ε, γ_2 and β phases were observed. This could be due to that formation of τ phase is sensitive to the stoichiometric composition of Mn and Al and their chemical circumstances. Excessive Zr additions (>=3 at.%) would suppress the formation of the τ phase, leading to the transformation of the ε phase to the equilibrium phases.

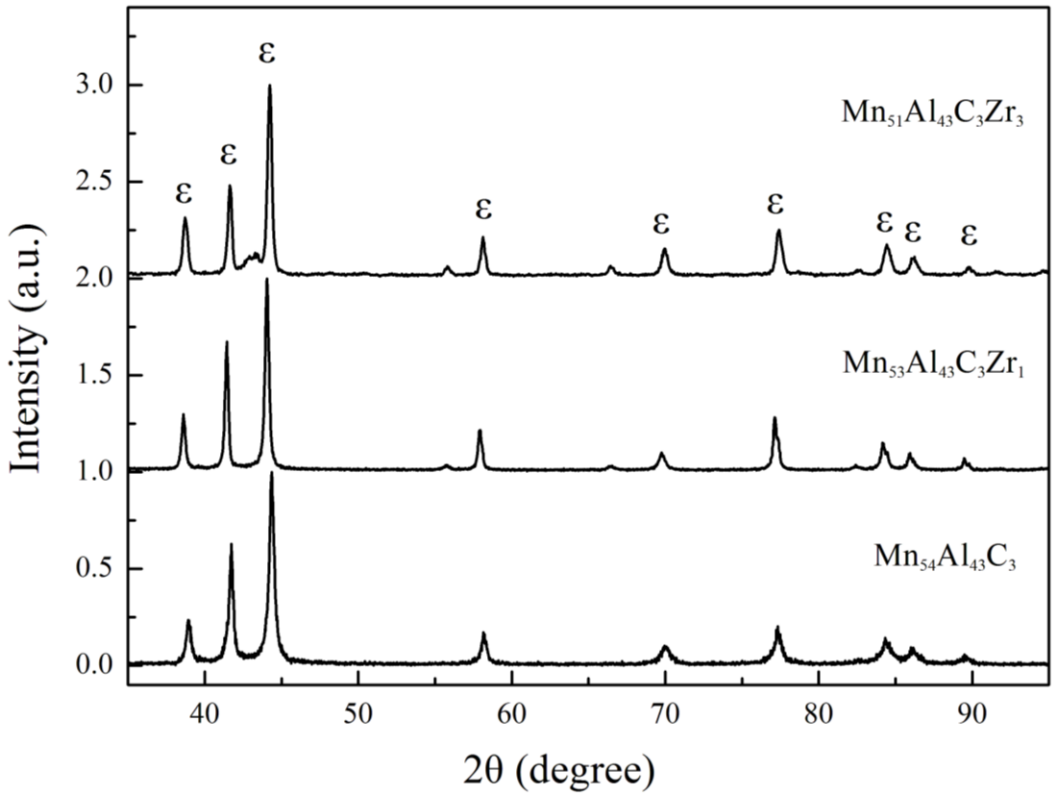

Figure 6.1 XRD pattern for as-solidified $Mn_{54-x}Al_{43}C_3Zr_x$ (x=0, 1, 3)

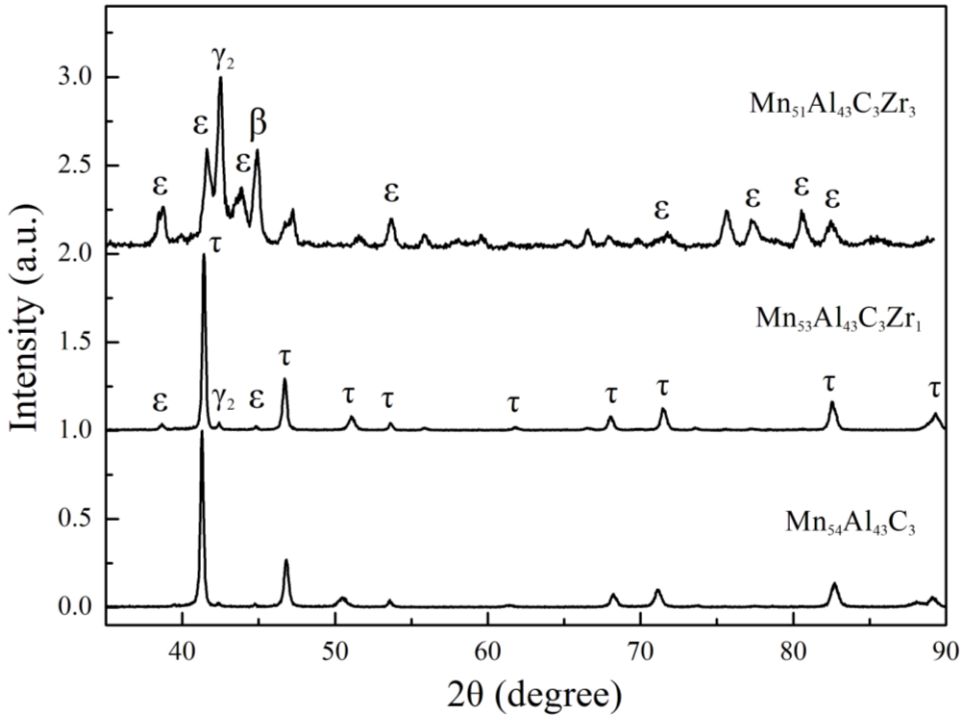

Figure 6.2 XRD pattern for $Mn_{54-x}Al_{43}C_3Zr_x$ (x=0, 1, 3) heat treated at 500 ℃ for 10 min.

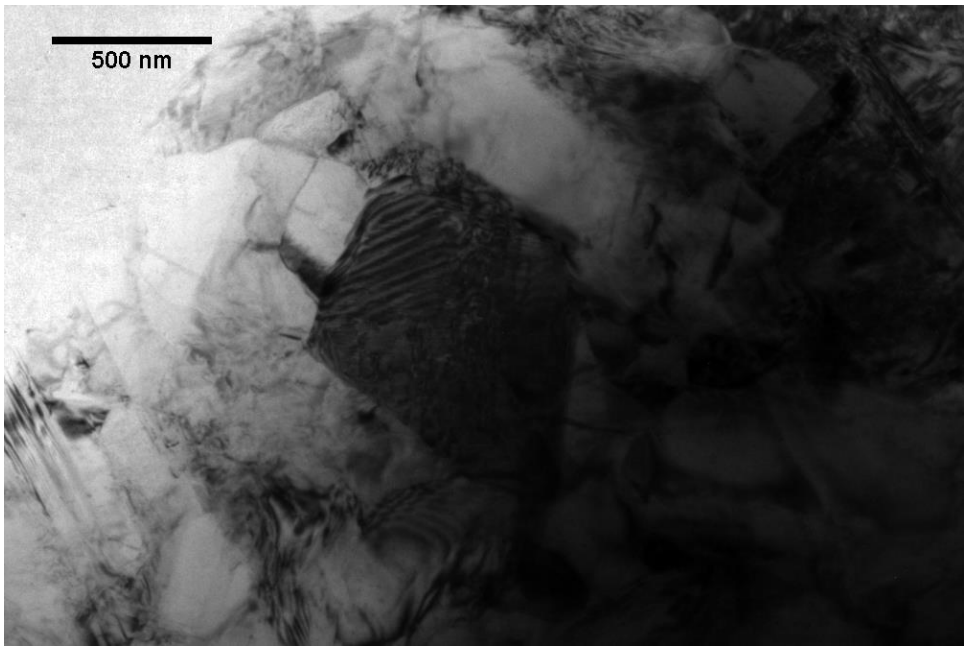

Figure 6.3 Transmission electron microscopy of annealed $Mn_{53}Al_{43}C_3Zr_1$

In order to perform a detailed structural investigation, full profile analysis of the powder diffractograms were carried out using Rietveld analysis technique [Bruker AXS,

TOPAS] on selected samples with nominal compositions of $Mn_{54}Al_{43}C_3$ and $Mn_{53}Al_{43}Zr_1C_3$. Both samples are formed with the desired τ phase, however, traces impurities Mn_5Al_8 and ZrO phases are found to be present in the case of $Mn_{53}Al_{43}Zr_1C_3$ sample. $Mn_{54}Al_{43}C_3$ was found to be single phase. The data was modeled based on the MnAl base structure with *P4/mmm* space group, Al atoms occupying 1a and 1c sites and Mn atoms occupying 2e sites to start with. Carbon atoms were envisaged as occupying the interstitial sites and were excluded in the refinement. Partial occupation of the Mn atoms at the Al sites was considered, the fits suggest that Mn are found to replace Al mostly in the 1c sites. Figure 6.4a depicts the experimental data, fit from Rietveld analysis and the different patterns for the sample $Mn_{54}Al_{43}C_3$. The value of R_{Bragg} obtained after the final refinement is 5.08%. The composition obtained from Rietveld analysis is close to $Mn_{54}Al_{46}$.

Starting from a similar model for the case of $Mn_{53}Al_{43}Zr_1C_3$, the Zr atoms were introduced at 1c site. The experimental data, fit result from refinement and the difference pattern are shown in Figure 6.4b. The refinement yielded nearly 87.6 wt. % of $Mn_{53}Al_{43}Zr_1C_3$, 10.4 wt.% of Mn_5Al_8 phase and 2 wt.% of ZrO. The average composition from refinement is $Mn_{53}Al_{46}Zr_1$. The value of R_{Bragg} after the final refinement is 2.6 %. A summary of the Rietveld analysis is given in Table 6.1.

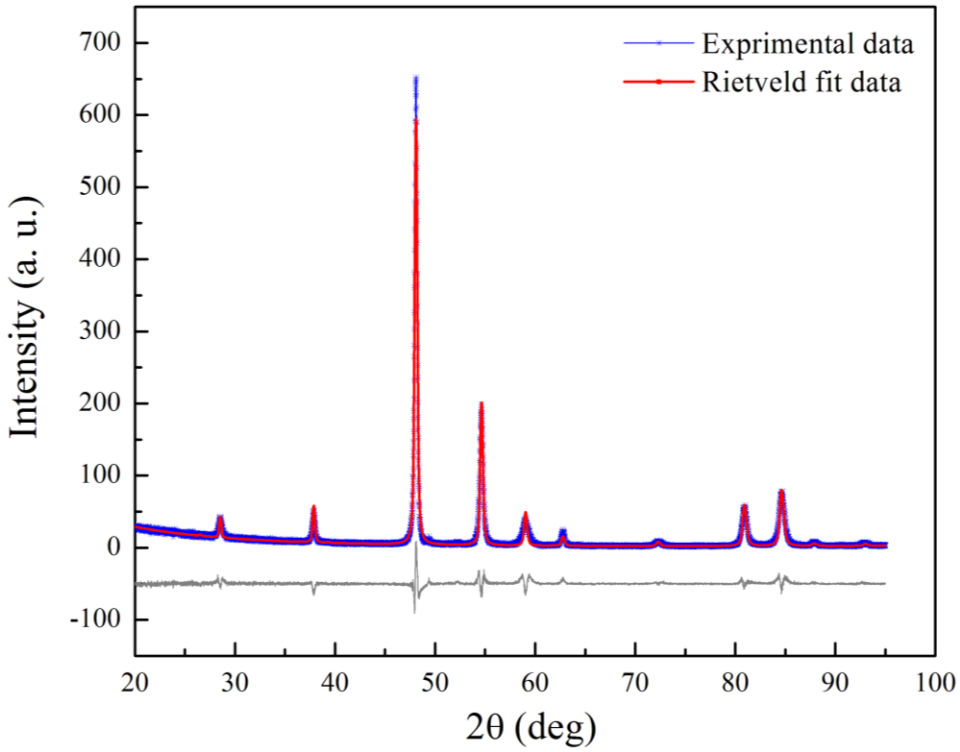

Figure 6.4a. The experimental, fit and the difference x-ray diffraction patterns of $Mn_{54}Al_{43}C_3$.

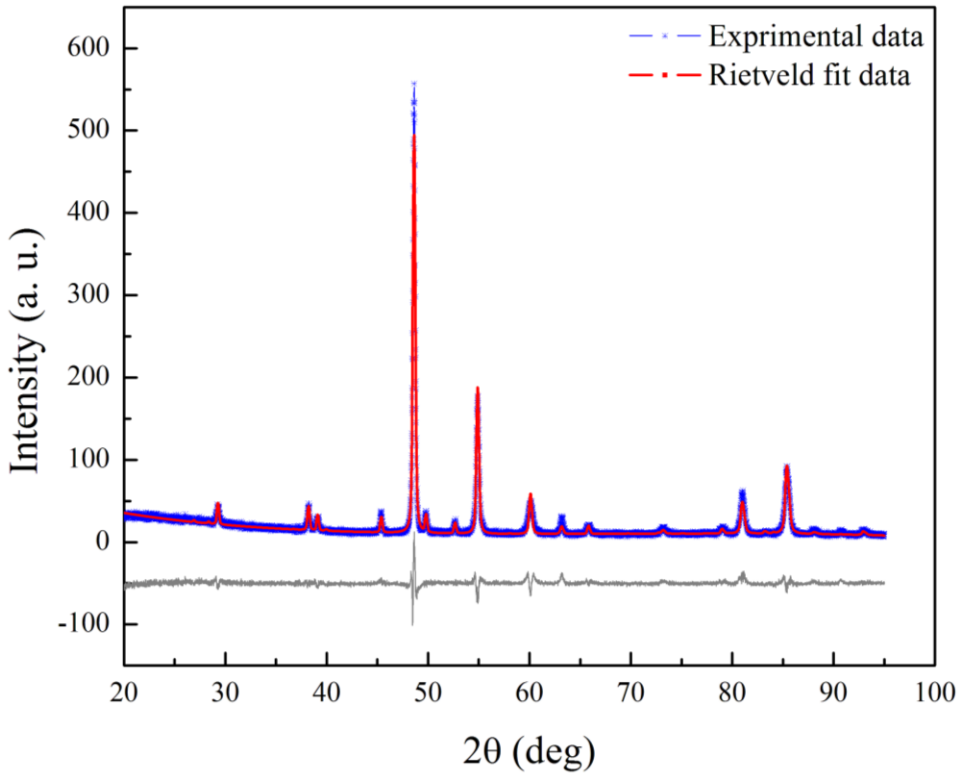

Figure 6.4b The experimental, fit and the difference x-ray diffraction patterns of $Mn_{53}Al_{43}Zr_1C_3$.

Table 6.1Phase composition, lattice parameters and accuracies estimated by the Rietveld analysis

Compound	A (Å)	C (Å)	Wt. % of phases			R_{Bragg}
			τ	γ	ZrO	
$Mn_{54}Al_{43}C_3$	3.9014	3.6337	100	Not detectable	absent	5.1
$Mn_{53}Al_{43}Zr_1C_3$	3.9122	3.5975	87.6	10.4	2	2.64

6. 3. 2 Phase transformation in Hf-modified $Mn_{54}Al_{43}C_3$ alloys

Similar phase transformations were found in the as-solidified and as-annealed $Mn_{54-y}Al_{43}C_3Hf_y$ (y=1, 3) as shown in Fig. 6.5 and Fig. 6.6. ε phase was determined to be the main phase in the as-solidified samples with minor ZrO phase having peaks at 39.08 °,

56.52° and 67.4° (2θ). After heat treatment at 500 ℃ for 10 min, τ phase was observed to be the primary phase in $Mn_{53}Al_{43}C_3Hf_1$, while the ε, γ_2, β phases were found as minor phases. Comparing the $Mn_{53}Al_{43}C_3Hf_1$ with the $Mn_{53}Al_{43}C_3Zr_1$, the relative percentage of ε was higher in $Mn_{53}Al_{43}C_3Hf_1$ than in annealed $Mn_{53}Al_{43}C_3Zr_1$, as indicated by the ratio of ε-to- τ peak intensities in the two x-ray diffraction patterns. In the as-annealed $Mn_{51}Al_{43}C_3Hf_3$ samples, ε, γ_2, β phases were observed to be the predominant phases. Thus, excessive Hf additions also suppress the transformation from ε phase to τ phase.

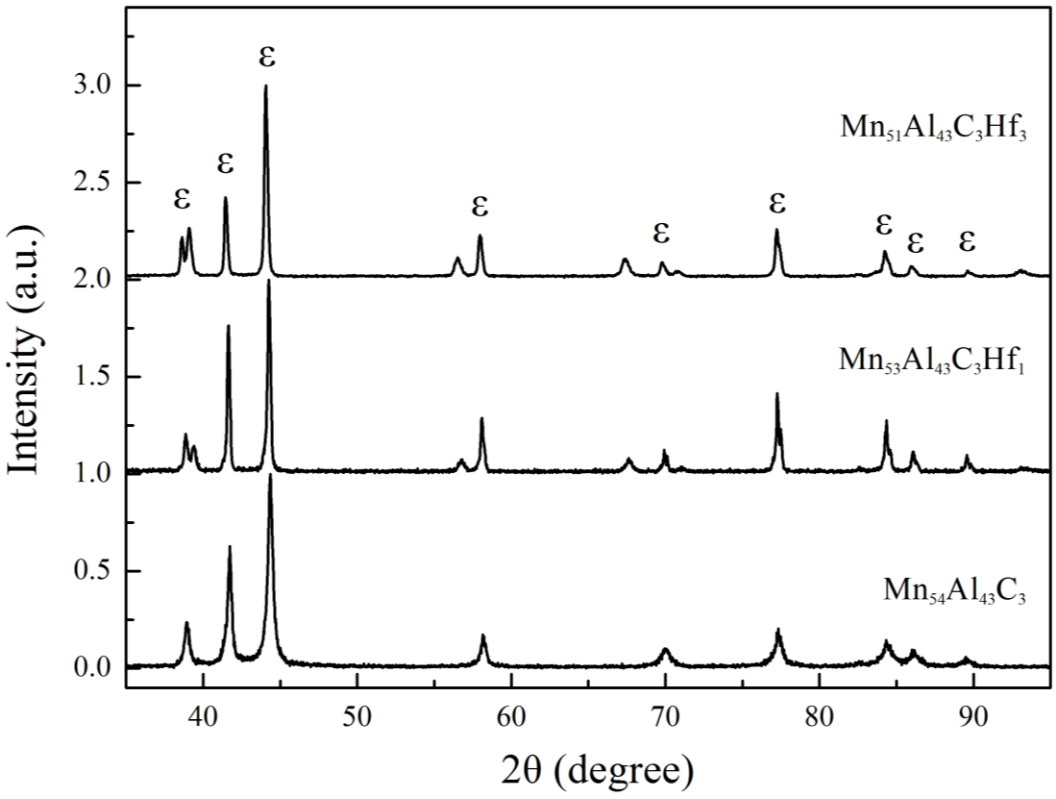

Figure 6.5 X-ray diffraction pattern for as-solidified $Mn_{54-y}Al_{43}C_3Hf_y$ (y=0, 1, 3)

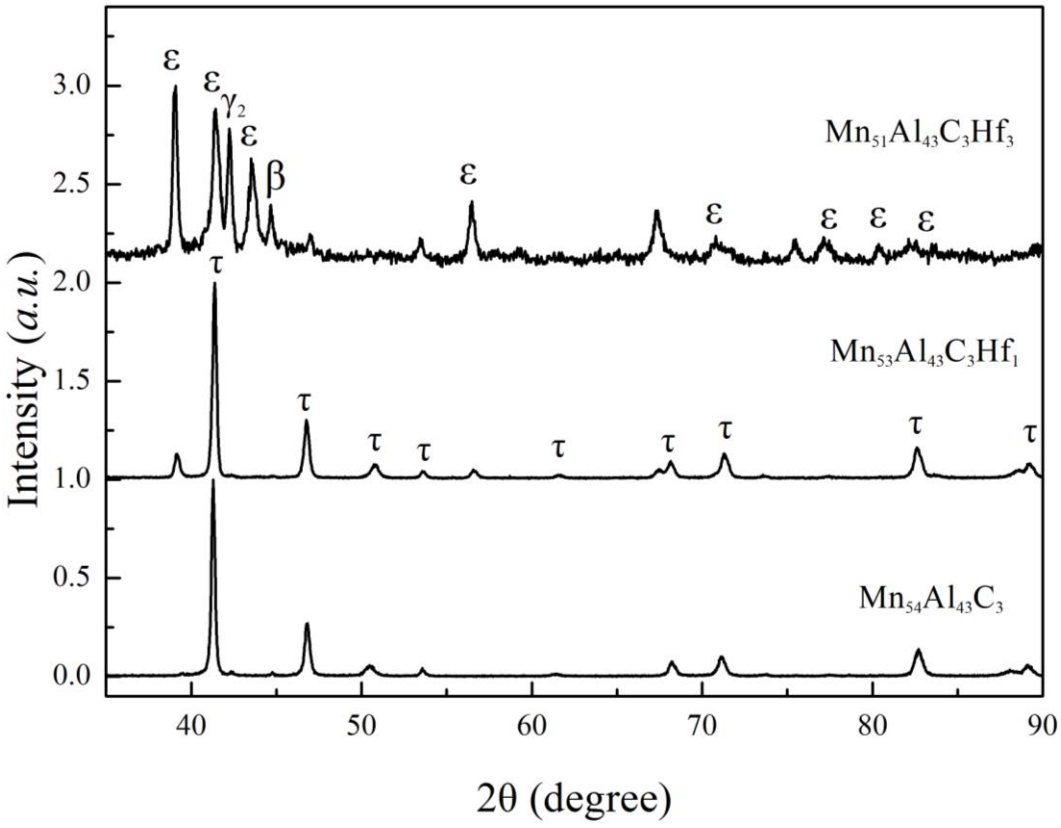

Figure 6.6 X-ray diffraction pattern for as-annealed $Mn_{54-y}Al_{43}C_3Hf_y$ (y=0, 1, 3)

6. 3. 3 Saturation magnetization enhancement in Zr- and Hf-modified $Mn_{54}Al_{43}C_3$ alloys

Hysteresis loop for the $L1_0$-structured $Mn_{53}Al_{43}C_3Zr_1$ and $Mn_{53}Al_{43}C_3Hf_1$ alloy is shown in Figure 6.7. The saturation magnetization (M_s) is determined by plotting M (magnetization) as a function of 1/H (H represents applied field) for H>20 kOe and extrapolating the linear regression fit to 1/H=0. The M_s and H_c for $L1_0$-structured $Mn_{54}Al_{43}C_3$ were reported 115 emu/g and 1.25 separately[16]. Even the weight of Mn_5Al_8 phase and ZrO phase is included, M_s could be as high as 128.0 ±1 emu/g. It could be due to the substitution of Zr to Mn in Al sites, which could suppress the antiferromagnetic

coupling and thus increase the net magnetization. Meanwhile, decrease of c/a ratio in $Mn_{53}Al_{43}C_3Zr_1$ might also contribute to the increase of saturation magnetization according to the Bethe-Slater curve. The M_s decreased with Hf addition, due to the existence of higher amounts of ε, γ_2, β phases. The H_c increased to 2.08 kOe with addition of 1 at.%Zr while it decreased to 1.53 kOe with the addition of Hf.. Since the parameter of coercivity is very sensitive to microstructures, the slight changes with addition of Zr could be due to microstructure, notably grain size, and defects introduced during the formation of τ phase.

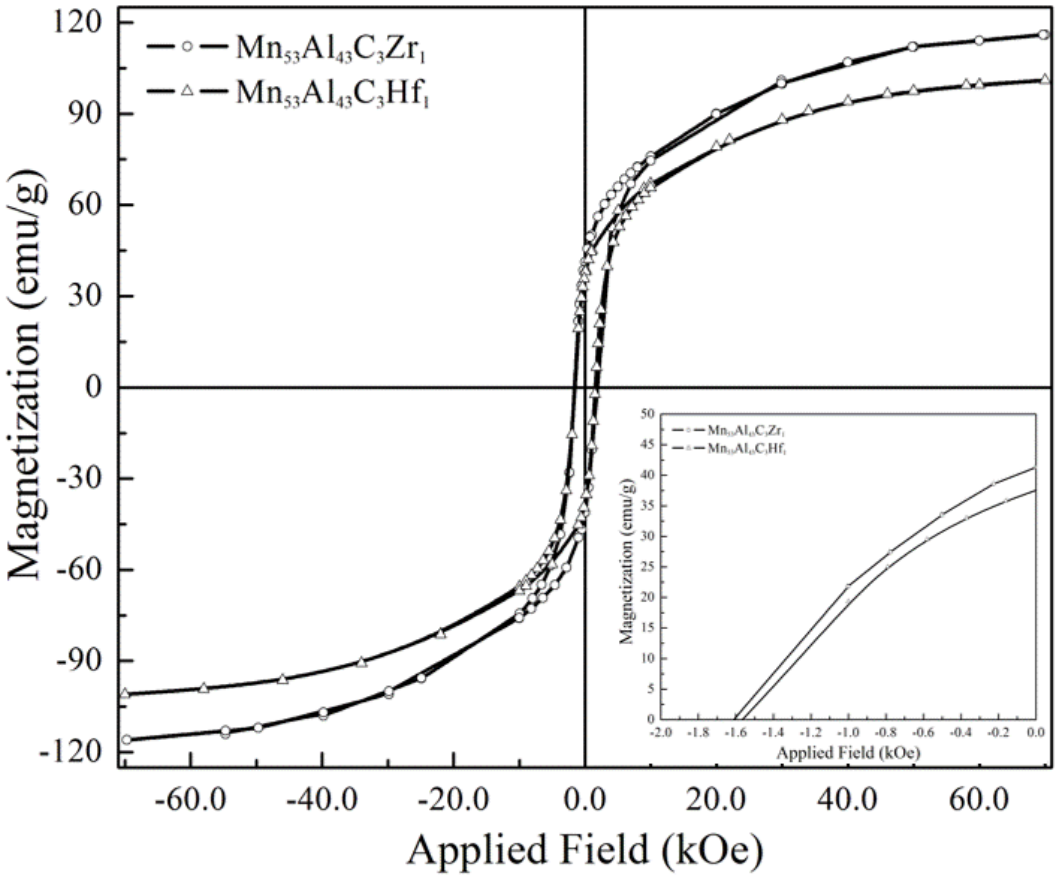

Figure 6.7 Hysteresis loop for as-annealed $Mn_{53}Al_{43}C_3Zr_1$ and $Mn_{53}Al_{43}C_3Hf_1$

6. 4 Structural and magnetic properties of $Mn_{53}Al_{43}C_3Zr_1$ alloys controlled by C addition

6. 4. 1 Phase transformation in $Mn_{53}Al_{43}C_3Zr_1$ alloys with excessive C additions

In order to maximize the energy product of $Mn_{53}Al_{43}C_3Zr_1$, enhancement of only saturation magnetization could not be enough. Therefore, further improvement of coercivity was conducted through microstructure modification. In magnetic materials, the microstructure, particularly the grain size, plays a critical role in maximizing the extrinsic magnetic property, namely coercivity[11,17]. Recent work on the grain refinement show that grain refinement can be facilitated by two factors: number and potency of the nucleant particles, and solute elements present in the melt[18-20]. Addition of solute elements could generate constitutional undercooling in the diffusion layer ahead of advancing solid/liquid interface, which may restrict grain growth since the slow diffusion of the solute limits the rate of grain growth[20]. Carbon addition would drive the formation of nucleant particles, like Al_4C_3, which may act as potent nucleation sites. Meanwhile, C has a strong tendency for segregation, which could greatly affect the constitutional undercooling and consequently restrict grain growth during the solidification process. Therefore, variable amounts of C (1%, 3%, 5% and 7%) were added to the $Mn_{53}Al_{43}C_3Zr_1$ alloys.

XRD patterns for as-solidified $(Mn_{53}Al_{43}C_3Zr_1)_{100-z}C_z$ (with z=0, 1, 3, 5, 7) were indexed to the ε phase. In contrast to the Zr-free alloys and the alloys without excess C

where conversion from ε to τ occurred readily after heat treatment at 500 ℃ for 10 minutes, excess C appeared to alter the decomposition kinetics. In as-solidified $(Mn_{53}Al_{43}C_3Zr_1)_{95}C_5$, it was observed that the ε phase was retained until heat treatment for 30 min when a large fraction of τ phase and a small amount of ε phase was observed (Fig. 6.8). Further heat treatment to 40 min didn't change the phase composition, as can be seen from the ratio of ε phase to τ phase, but it did cause a reduction in peak width, showing grain growth with elongated annealing time. With annealing for 60 min, transformation of τ phase to ε, γ_2, β phases occurred. To obtain a large fraction of the τ phase and smaller grain size, the optimum heat treatment time at 500 ℃ for each sample have been determined as shown in Fig. 6.9. When the amount of C was increased from z=1 to 7, the heat treatment time to complete the transformation to τ is extended from 10 min to 60 min. XRD patterns for annealed $(Mn_{53}Al_{43}C_3Zr_1)_{100-z}C_z$ (z=0, 1, 3, 5, 7) were shown in Fig. 6.10. The τ phase was determined to be the primary phase in annealed $(Mn_{53}Al_{43}C_3Zr_1)_{100-z}C_z$ (z=0, 1, 3, 5, 7) samples, while ε, γ_2, β phases were found as minor phases. On the other hand, annealing the $(Mn_{53}Al_{43}C_3Zr_1)_{93}C_7$ at 500 ℃ for 60 min produced primarily τ phase with small amounts of ε, γ_2, β phases; the τ phase was much more stable than in the case of $(Mn_{53}Al_{43}C_3Zr_1)_{95}C_5$. Excessive C could suppress the phase transformation process from ε phase to τ phase and stabilize the τ phase.

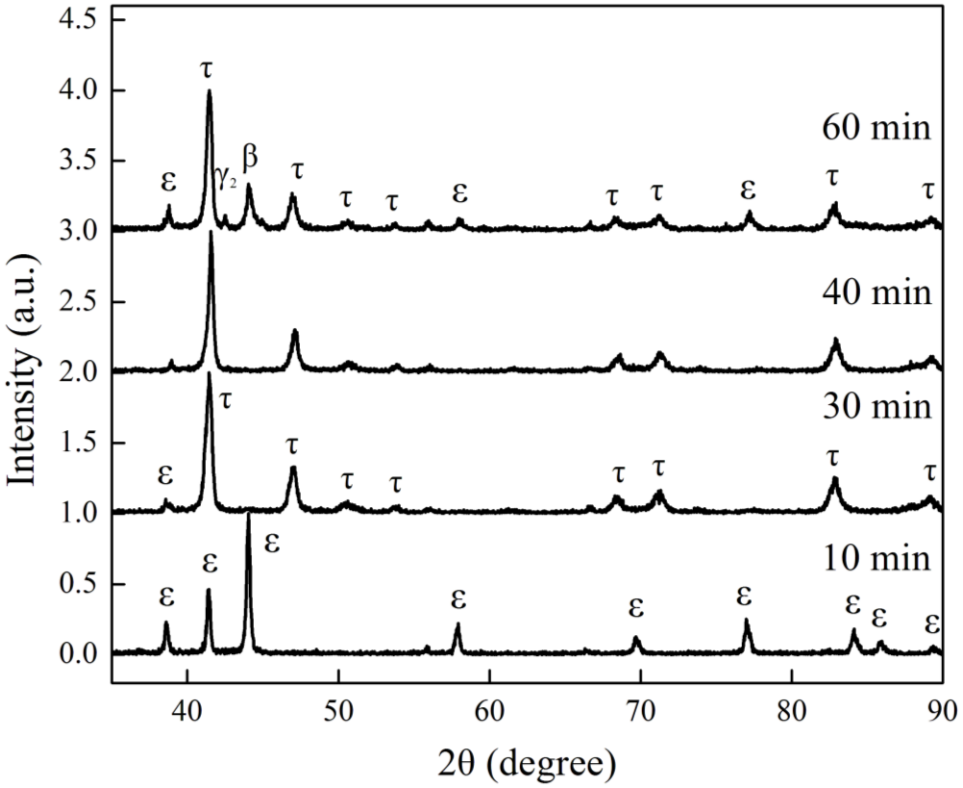

Figure 6.8 XRD patterns for $(Mn_{53}Al_{43}C_3Zr_1)_{95}C_5$ with variable annealing time (t=10, 30, 40, 60 min)

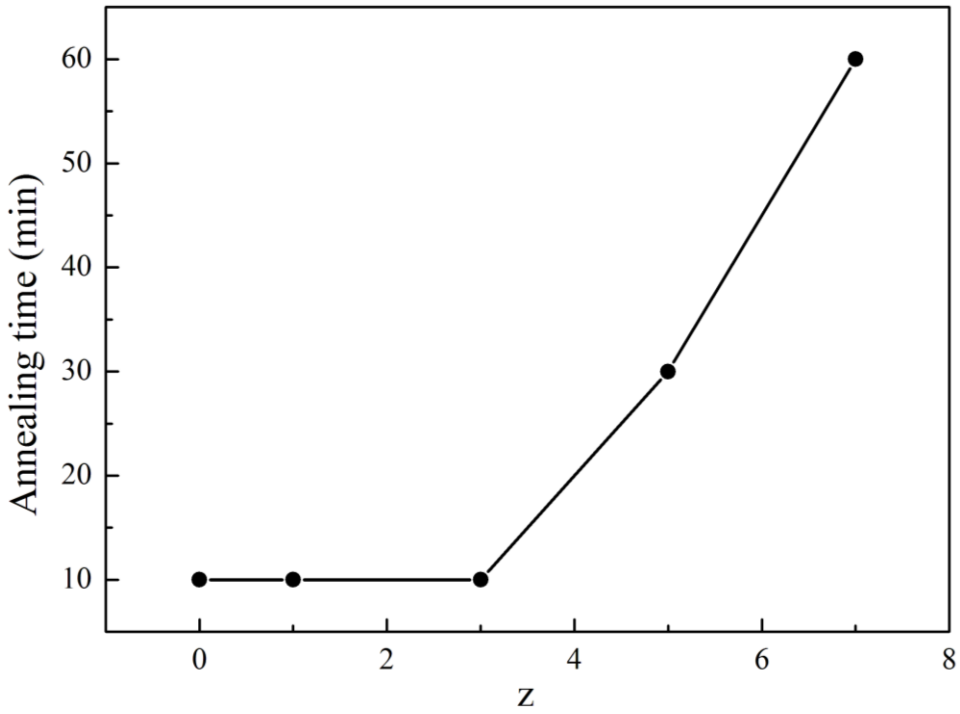

Figure 6.9 Optimum annealing time for samples $(Mn_{53}Al_{43}C_3Zr_1)_{100-z}C_z$ (with z=0, 1, 3, 5, 7)

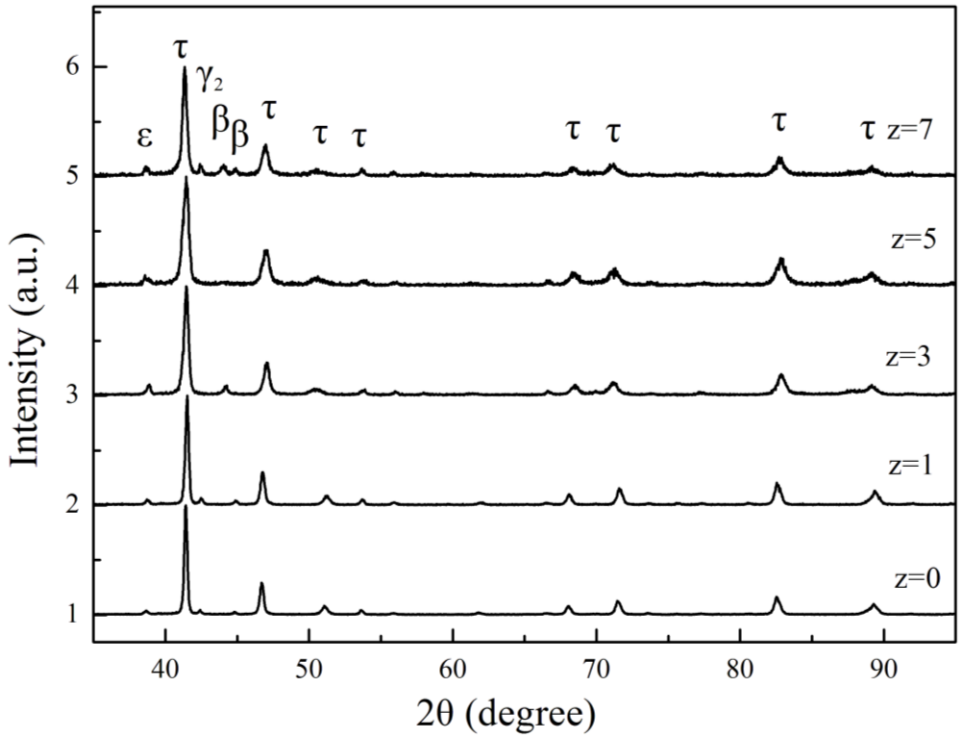

Figure 6.10 XRD patterns for annealed $(Mn_{53}Al_{43}C_3Zr_1)_{100-z}C_z$ (z=0, 1, 3, 5, 7)

The effect of C content on grain size was then investigated based on the XRD patterns. Since peak broadening could be caused by both grain size reduction and strain, Williamson-Hall equation[21] was employed to isolate the grain size effect. The W-H equation for the total peak broadening is given by

$$B_r \cos\theta = \frac{k\lambda}{t} + \eta \sin\theta \tag{6.1}$$

where $B_r = (B_0^2 - B_i^2)^{1/2}$, is instrumental corrected broadening; B_0 the observed peak broadening; B_i the broadening due to instrumental factors in radians; k a constant, usually taken as 1; t the crystallite size in nanometers; θ the Bragg's angle; λ is the wavelength of incident X-ray beam in nm; η the strain distribution within the material. The plot of $B_r\cos\theta$ versus sinθ gives a straight line with slope equal to η and the intercept

along the abscissa as kλ/t. The crystallite size t can be calculated from the intercept. The Williamson-Hall plot for $(Mn_{53}Al_{43}C_3Zr_1)_{97}C_3$ is shown in Fig. 6.11. The reciprocal of the intercept along the abscissa at sinθ=0 gives the grain size in each case. The dependence of grain size on C content in $(Mn_{53}Al_{43}C_3Zr_1)_{100-z}C_z$ (z=0, 1, 3, 5, 7) is shown in Fig. 6.12. A decrease in grain size from 550 nm to 50 nm with excess C addition up to 3% (z=3) was observed. However, the grain size remained relatively constant with further C addition, which might be caused by elongated annealing time.

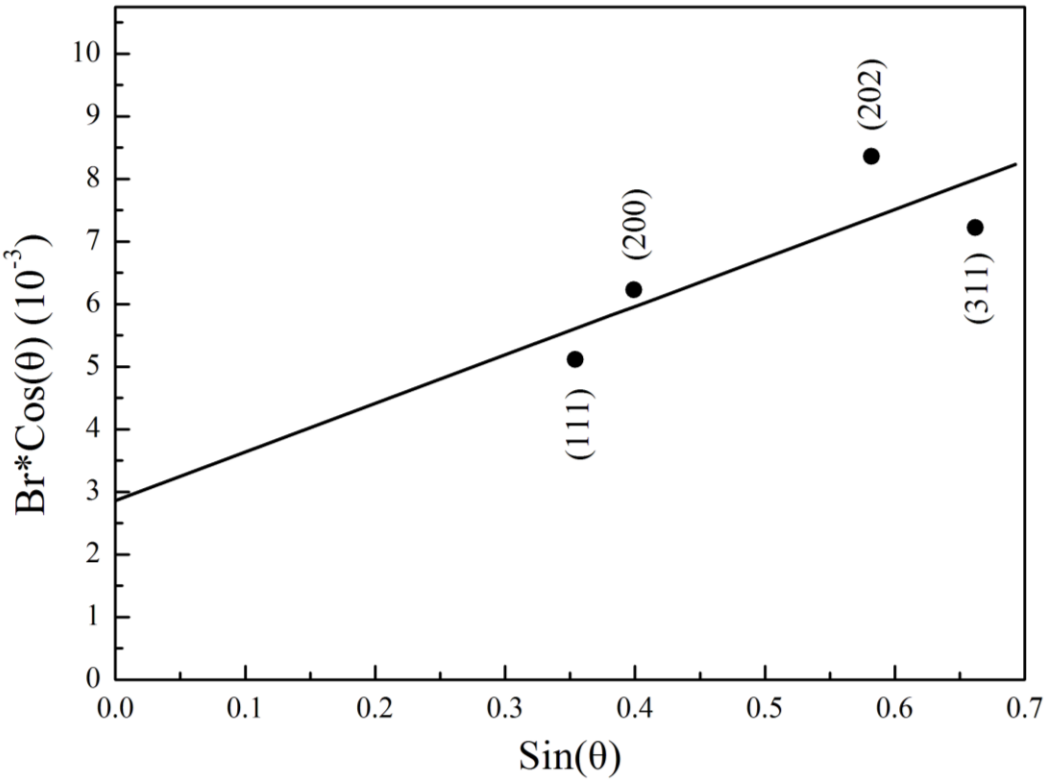

Figure 6.11 Williamson-Hall plot of as-annealed $(Mn_{53}Al_{43}C_3Zr_1)_{97}C_3$

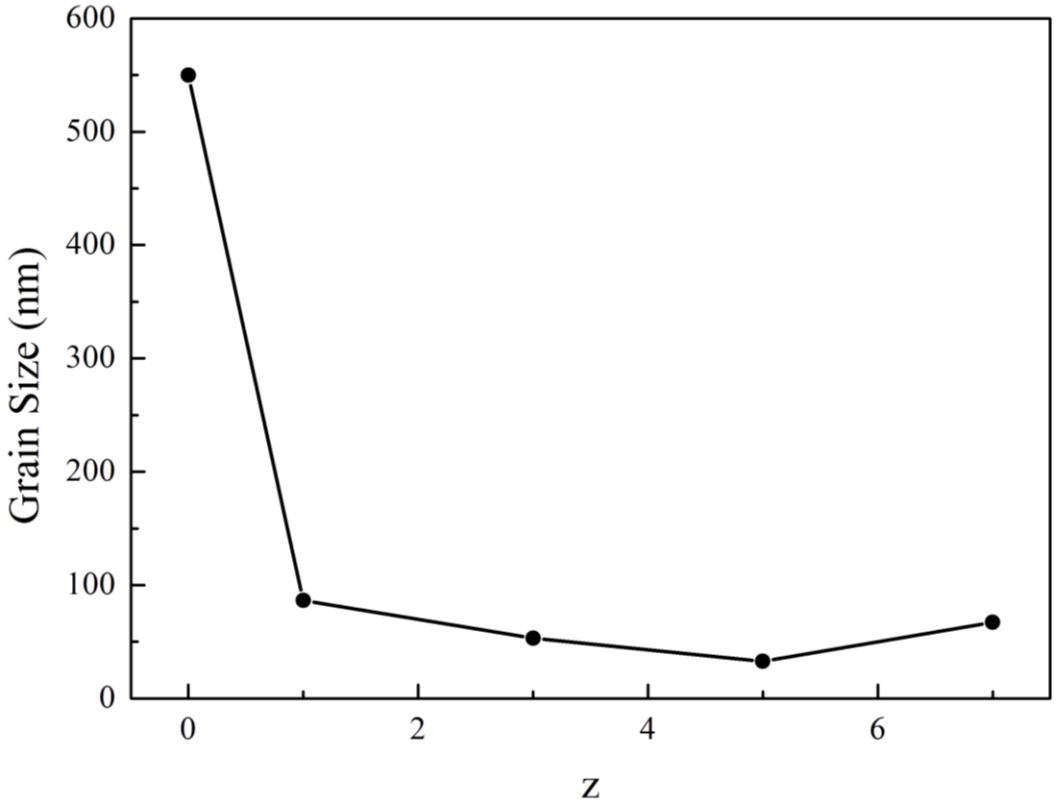

Figure 6.12 Dependence of grain size in $(Mn_{53}Al_{43}C_3Zr_1)_{100-z}C_z$ (z=0, 1, 3, 5, 7) on C content

6. 4. 2 Magnetic properties in $Mn_{53}Al_{43}C_3Zr_1$ alloys with excessive C additions

Influence of C addition in $(Mn_{53}Al_{43}C_3Zr_1)_{100-z}C_z$ (z=0, 1, 3, 5, 7) on the magnetic properties including coercivity (H_c), and saturation magnetization (M_s) is shown in Fig. 6.13 and Fig. 6.14. The influence of C content on M_s is clearly evident. τ phase is the only ferromagnetic phase in the MnAl system, so the M_s is proportional to the percentage of τ phase in the alloys. Transformation from τ phase to ε, γ_2, and β phases involves the nucleation and grain growth process, which is a diffusion-controlled process. The increase in stability with C content occurs because the excessive C atoms in grain

boundary inhibit the diffusion of the Mn and Al atoms. Meanwhile, carbide precipitates will form at higher C concentrations and act as nucleation sites for the equilibrium phases when the C addition exceeds the solubility limit (~3 at. %). Excessive C enhanced the formation of nonmagnetic ε, γ_2, and β phases and decreased the saturation magnetization.

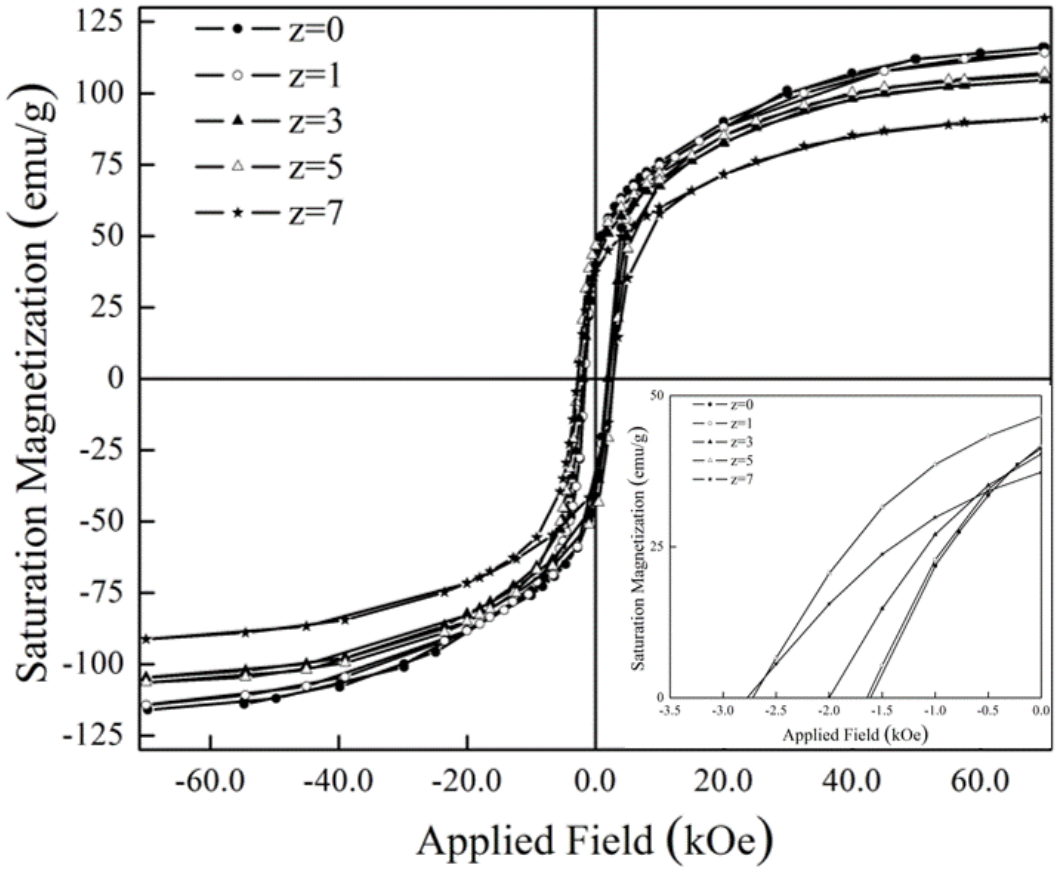

Figure 6.13 Hysteresis loop for as-annealed $(Mn_{53}Al_{43}C_3Zr_1)_{100-z}C_z$ (z=0, 1, 3, 5, 7)

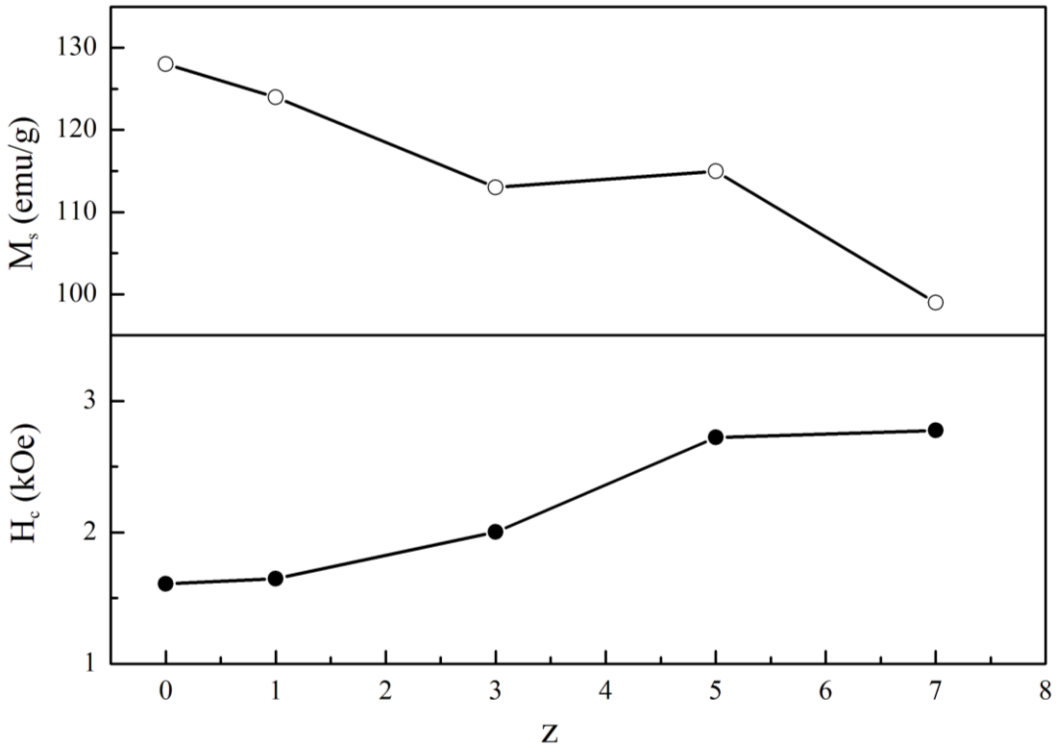

Figure 6.14 Dependence of Coercivity (H_c) and saturation magnetization (M_s) on Carbon content in $(Mn_{53}Al_{43}C_3Zr_1)_{100-z}C_z$ (z=0, 1, 3, 5, 7)

The coercivity shows an opposite trend with C addition as the saturation magnetization. This may be explained by the lower dependence of H_c on the amounts of τ phase, and more on the τ phase microstructure. The coercivity will increase when the grain size gets closer to the single domain size. The single domain size for the MnAl permanent alloy is approximately tens of nanometers, so the decrease in grain size from 550 nm to 50 nm will contribute to the increased coercivity. Furthermore, when the grain size becomes constant with further addition of C ~5 at. %, an increase of coercivity is observed. This could be due to existence of ε, γ_2, and β phases, which would decouple the exchange interactions between different MnAl grains. The maximum H_c (3.1 kOe) was obtained in $(Mn_{53}Al_{43}C_3Zr_1)_{93}C_7$.

6. 5 Conclusion

As-quenched $Mn_{53}Al_{44}C_3$ alloys with 1 at.% Zr doping exhibits a single phase structure consisting of the ε phase. After heat treatment at 500 ℃ for 10 min, transformation from ε to τ phase is achieved with higher saturation magnetization 128.0 ±1 emu/g. Further enhancement of coercivity in $Mn_{53}Al_{43}C_3Zr_1$ is possible through the addition of C, which reduced the grain size from ~600 nm to around 50 nm. Meanwhile, formation of ε, γ_2, and β phases, caused by excess C addition, decoupled the exchange interactions between different Mn-Al-C domains. It improved the coercivity even though the grain size stopped increasing with C addition ~ 5 at.%, A decrease of saturation magnetization was as-expected because τ phase is the only ferromagnetic phase.

References

1 Park, J., Hong, Y., Bae, S., Lee, J., Jalli, J., Abo, G., Neveu, N., Kim, S., Choi, C. & Lee, J. Saturation magnetization and crystalline anisotropy calculations for MnAl permanent magnet. *Journal of Applied Physics* **107**, 09A731-709A731-733 (2010).

2 Koch, A., Hokkeling, P. & de Vos, K. New material for permanent magnets on a base of Mn and Al. *Journal of Applied Physics* **31**, S75-S77 (1960).

3 Van Den Broek, J., Donkersloot, H., Van Tendeloo, G. & Van Landuyt, J. Phase transformations in pure and carbon-doped Al< sub> 45</sub> Mn< sub> 55</sub> alloys. *Acta Metallurgica* **27**, 1497-1504 (1979).

4 Yanar, C., Wiezorek, J., Soffa, W. & Radmilovic, V. Massive transformation and the formation of the ferromagnetic $L1_0$ phase in manganese-aluminum-based alloys. *Metallurgical and Materials Transactions A* **33**, 2413-2423 (2002).

5 Kurtulus, Y. & Dronskowski, R. Electronic structure, chemical bonding, and spin polarization in ferromagnetic MnAl. *Journal of Solid State Chemistry* **176**, 390-399 (2003).

6 Massalski, T. B., Okamoto, H., Subramanian, P. & Kacprzak, L. *Binary alloy phase diagrams*. (ASM international, 1990).

7 Pareti, L., Bolzoni, F., Leccabue, F. & Ermakov, A. Magnetic anisotropy of MnAl and MnAlC permanent magnet materials. *Journal of Applied Physics* **59**, 3824-3828 (1986).

8 Fazakas, E., Varga, L. & Mazaleyrat, F. Preparation of nanocrystalline Mn–Al–C magnets by melt spinning and subsequent heat treatments. *Journal of Alloys and Compounds* **434**, 611-613 (2007).

9 Zeng, Q., Baker, I., Cui, J. & Yan, Z. Structural and magnetic properties of nanostructured Mn–Al–C magnetic materials. *Journal of Magnetism and Magnetic Materials* **308**, 214-226 (2007).

10 Le Breton, J., Bran, J., Folcke, E., Lucis, M., Lardé, R., Jean, M. & Shield, J. Structural modifications in a Mn< sub> 54</sub> Al< sub> 43</sub> C< sub> 3</sub> melt-spun alloy induced by mechanical milling and subsequent annealing investigated by atom probe tomography. *Journal of Alloys and Compounds* **581**, 86-90 (2013).

11 Lucis, M. J., Prost, T. E., Jiang, X., Wang, M. & Shield, J. E. Phase Transitions in Mechanically Milled Mn-Al-C Permanent Magnets. *Metals* **4**, 130-140 (2014).

12 Sakka, Y., Nakamura, M. & Hoshimoto, K. Rapid quenching and properties of hard magnetic materials in MnAl-X (X= Ti, Cu, Ni, C, B) systems. *Journal of Materials Science* **24**, 4331-4338 (1989).

13 Wang, H., Si, P., Jiang, W., Lee, J., Choi, C., Liu, J., Wu, Q., Zhong, M. & Ge, H. Structural Stabilizing Effect of Zn Substitution on MnAl and Its Magnetic Properties. *Open Journal of Microphysics* **1**, 19 (2011).

14 H. X. Wang, P. Z. S., W. Jiang, X. F. Xiao, J. G. Lee, C. J. Choi, M. Zhong, Z. F. Li and H. L. Ge. Structure and Magnetic Properties of Cu Doped MnAl. *Physical Science International Journal* **4**, 5, doi:10.9734/PSIJ/2014/5326 (2014).

15 Liu, Z., Chen, C., Zheng, Z., Tan, B. & Ramanujan, R. V. Phase transitions and hard magnetic properties for rapidly solidified MnAl alloys doped with C, B, and rare earth elements. *Journal of Materials Science* **47**, 2333-2338 (2012).

16 Prost, T. E. Magnetic Properties Study of the Mn-Al System with Additions of B or C and Mechanical Milling Techniques. (2012).

17 Rave, W. & Ramstöck, K. Micromagnetic calculation of the grain size dependence of remanence and coercivity in nanocrystalline permanent magnets. *Journal of Magnetism and Magnetic Materials* **171**, 69-82 (1997).

18 Dahle, A. K., Lee, Y. C., Nave, M. D., Schaffer, P. L. & StJohn, D. H. Development of the as-cast microstructure in magnesium–aluminium alloys. *Journal of light metals* **1**, 61-72 (2001).

19 Lee, Y., Dahle, A., StJohn, D. & Hutt, J. The effect of grain refinement and silicon content on grain formation in hypoeutectic Al–Si alloys. *Materials Science and Engineering: A* **259**, 43-52 (1999).

20 Jin, Q., Eom, J.-P., Lim, S.-G., Park, W.-W. & You, B.-S. Grain refining mechanism of a carbon addition method in a Mg–Al magnesium alloy. *Scripta Materialia* **49**, 1129-1132 (2003).

21 Williamson, G. & Hall, W. X-ray line broadening from filed aluminium and wolfram. *Acta Metallurgica* **1**, 22-31 (1953).

Chapter 7 Grain refinement of $Mn_{53}Al_{43}C_3Zr_1$ alloy by surfactant-assisted mechanical milling

In this chapter, nanocrystalline ε-phase and τ-phase $Mn_{53}Al_{43}C_3Zr_1$ powders were prepared through surfactant-assisted mechanical milling. Surfactants can prevent the rewelding of the crashed particles during the milling process. It has been observed that the grain refinement could be achieved by surfactant-assisted mechanical milling, which could enhance the coercivity. Maximum coercivity ~3.5 kOe was observed in nanocrystalline ε-phase milled and τ-phase milled $Mn_{53}Al_{43}C_3Zr_1$ powders. However, loss of ordering in $L1_0$ structure in τ-phase milled alloy was found with further milling, causing decrease in coercivity. The formation of other equilibrium phases, including ε phase, β-Mn phase and ZrO phase, induced the loss of magnetization in both τ- and ε-milled alloys. Meanwhile, the amorphous materials formed during mechanical milling enhanced the magnetization in long-time milled samples, as shown in the hysteresis loops and confirmed by the DTA results.

7. 1 Introduction

$L1_0$-structured (τ phase) Mn-Al permanent magnets, abundant and inexpensive, shows promising permanent magnetic properties: high experimental coercivity (~4.8 kOe) and potential maximum energy product of ~12 MGOe[1-3]. It has a chemically ordered face centered tetragonal structure with alternating monatomic layers of Mn and Al along the c-axis direction. The τ phase is formed by rapidly cooling the high-temperature

antiferromagnetic ε phase (hcp) followed by heat treatment at 450–600 °C[4-6]. However, τ phase is a metastable phase, higher annealing temperature results in decomposition to the γ (Al_8Mn_5) and β (Mn) phases[7]. Existence of C in the interstitial sites in MnAl alloys could stabilize the τ phase by suppressing the formation of equilibrium phases, causing a decrease of Curie temperature at the same time[2,8,9]. Meanwhile, due to the hyperstoichiometric composition of τ-phase Mn-Al alloy ($0.40<X_{Al}<0.46$), the saturation magnetization is smaller than stoicihometrically perfect $L1_0$-structure Mn-Al alloy[3]. Doping of 1 at.% Zr in $Mn_{54}Al_{43}C_3$ could enhance the saturation magnetization to 128 emu/g. Thus $Mn_{53}Al_{43}C_3Zr_1$ was used to maximize the saturation magnetization in this study.

Grain refinement by mechanical milling/alloying has been achieved in Mn-Al-based alloys[10-12]. Mechanical alloying of Mn-Al and Mn-Al-C powder followed by heat treatment resulted in formation of τ-phase Mn-Al alloy, but the saturation magnetization was low due to its composition and phase presented[10]. Mechanical milling of ε-phase Mn-Al alloy obtained from gas atomization[11] and melt-spinning[12] resulted in higher coercivity with loss of magnetization. Even more dramatic loss of magnetization was observed in τ-phase milled alloy[12]. Surfactant-assisted mechanical milling, without cold welding process, could lead to grain refinement with an appropriate surfactant and organic carrier liquid[13]. It's been briefly studied that τ-phase MnAl alloy milled with surfactant consisted of flat platelets with a tremendously high aspect ratio, which might cause relatively stable coercivity after milling ~32 h[12]. In this study, systematic efforts have been made to study the phase transformations and magnetic properties of surfactant-assisted mechanically-milled Mn-Al-based alloy.

7. 2 Experimental procedure

The composition of $Mn_{53}Al_{43}C_3Zr_1$ was chosen to maximize saturation magnetization of 128 emu/g. The alloys were prepared by arc melting high purity (>99.97%) Mn, Al, C, and Zr elements in an Ar atmosphere. ε-phase ribbons were obtained by rapid solidification through a single-roller melt spinner at a tangential wheel speed of 40 m/s. To ensure homogeneity during further processing and measurement, the as-solidified ribbons were hand-grinded in a mortar and pestle into powders. The powders were heat treated at 500 ℃ for 10 min by sealing in quartz capsules after repeated evacuation/backfill cycles using UHP Ar followed by water quenching to retain the τ phase. Mechanical milling was done in a SPEX 8000 Mixer/Mill using hardened steel vials and balls in nitrogen atmosphere. The total mass of the balls was 4 g and the ball-to-sample weight ratio was kept 10:1 during the experiment. To reduce temperature excursions, the milling was done on an intermittent basis, with 5 minutes of milling followed by 5 minutes off. Heptane (99.8% purity) was used as milling medium and oleic acid (90%) as surfactant during milling. The amount of surfactant used was the same as the weight of the powder.

Structural and morphological characterization were done using x-ray diffraction (Rigaku Multiflex using Cu-Kα radiation) and scanning electron microscopy (SEM). Samples for magnetic measurements were prepared by embedding the powders in epoxy. Magnetic measurements at room temperature were performed using vibrating sample magnetometer (Lakeshore 8500) with measuring field up to 9 kOe.

7. 3 Results and discussion

7. 3. 1 Phase transformation and magnetic properties of τ-phase milled (τ-milled) alloy

Figure 7.1 shows the XRD data of τ-milled samples for different milling times. The samples have mainly ordered $L1_0$ structure with the presence of ε phase, β-Mn phase and ZrO phase. As the alloy is milled, the XRD peaks are getting broader, indicating a possible smaller crystallite size and increasing strain. Fracture surfaces (cleavage steps, feather markings) of the $Mn_{53}Al_{43}C_3Zr_1$ ribbons exhibit mainly transgranular failure mode (Figure 7. 2), which confirmed that smaller crystallite size could be achieved through mechanical milling.

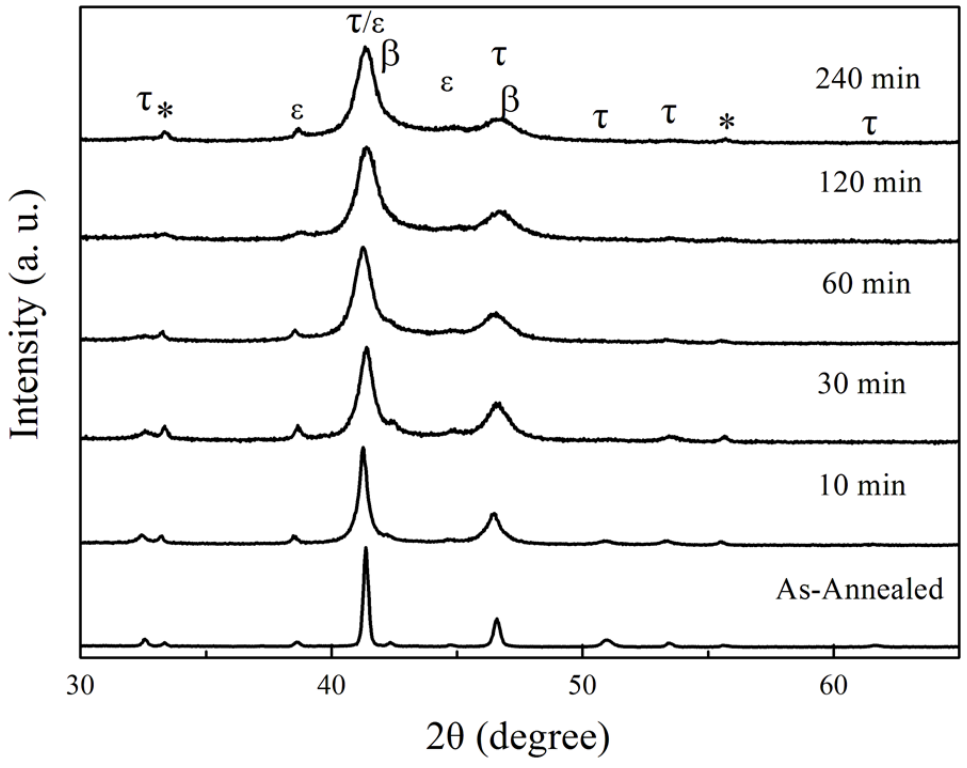

Figure 7.1 XRD patterns for τ-milled samples

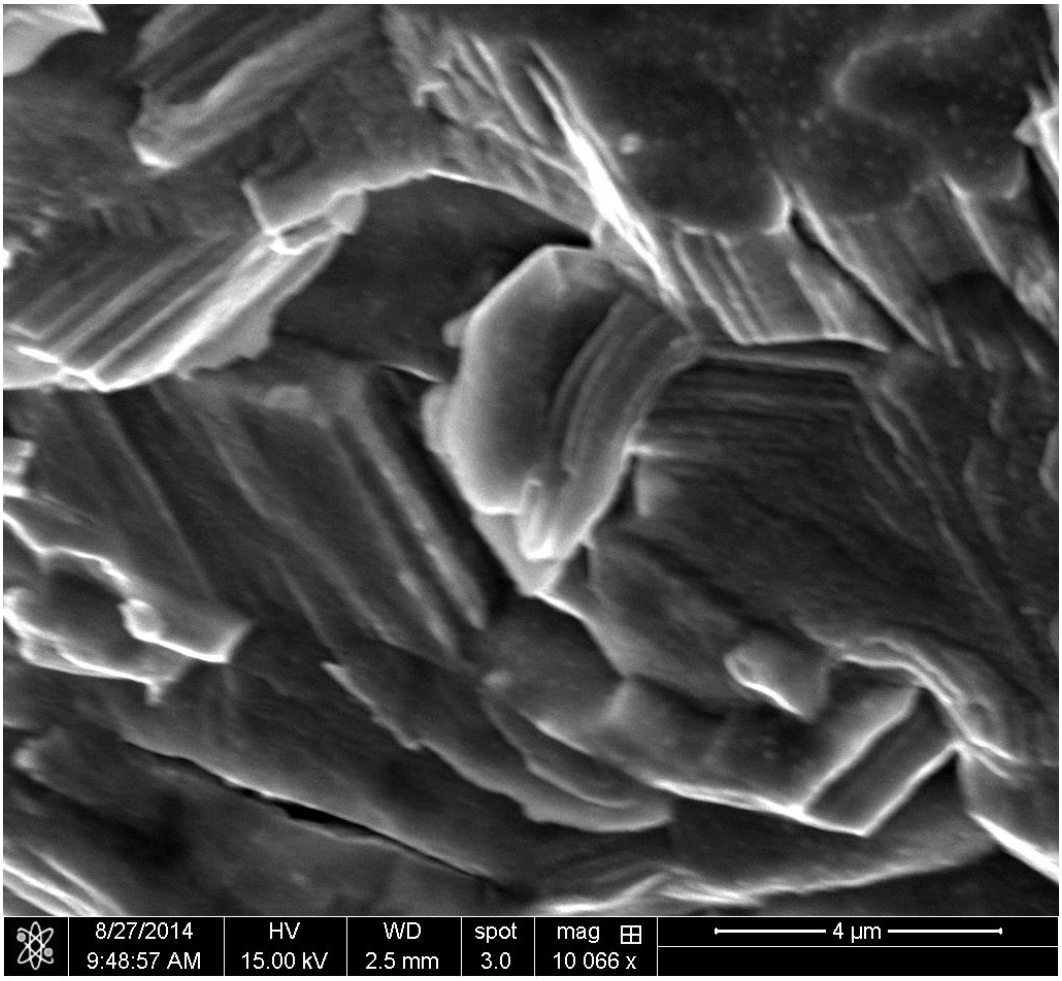

Figure 7.2 Scanning electron microscopy images of fracture surfaces

Figure 7. 3 presents the hysteresis loops for the powders milled for a variety of times (10, 30, 60, 120, 240 min). The corresponding magnetization at 9 kOe decreased from 78 emu/g to around 20 emu/g with milling up to 60 min, while even lower magnetizations were observed with further milling. A kink in the 120-min and 240-min milled samples appeared in the 2nd quadrant, indicating the existence of a 2nd phase, which shows a relatively higher magnetization and lower coercivity than that of the τ phase. Since there's no new phases appearing in the corresponding XRD patterns, amorphous materials could be responsible for the new phase. DTA was then employed to

monitor the phase transformation as shown in Figure 7. 5. Compared to the DTA curve for as-annealed $Mn_{53}Al_{43}C_3Zr_1$, the exothermic peak, at about 420 ℃, was found in both 120-min and 240-min milled samples. This indicated the existence of amorphous materials, which could be the cause of consistent magnetization with further milling up to 240 min.

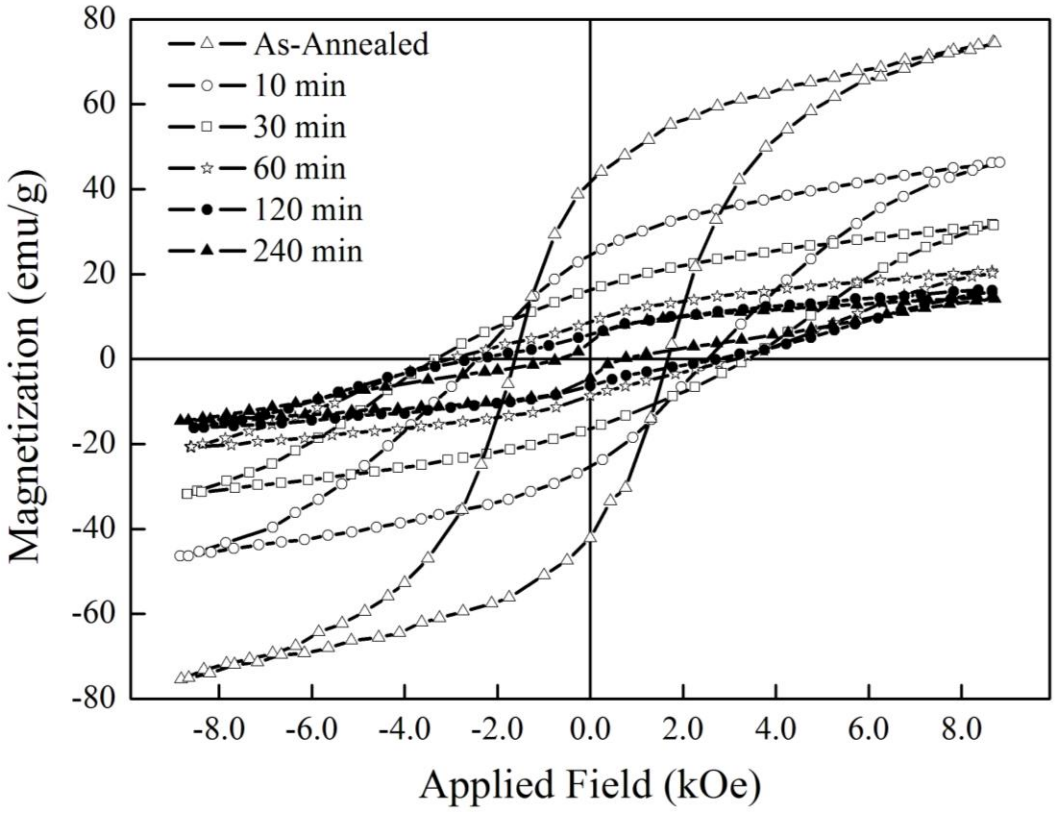

Figure 7.3 Hysteresis loops for τ-milled samples. Milling time ranges from 10 min to 240 min.

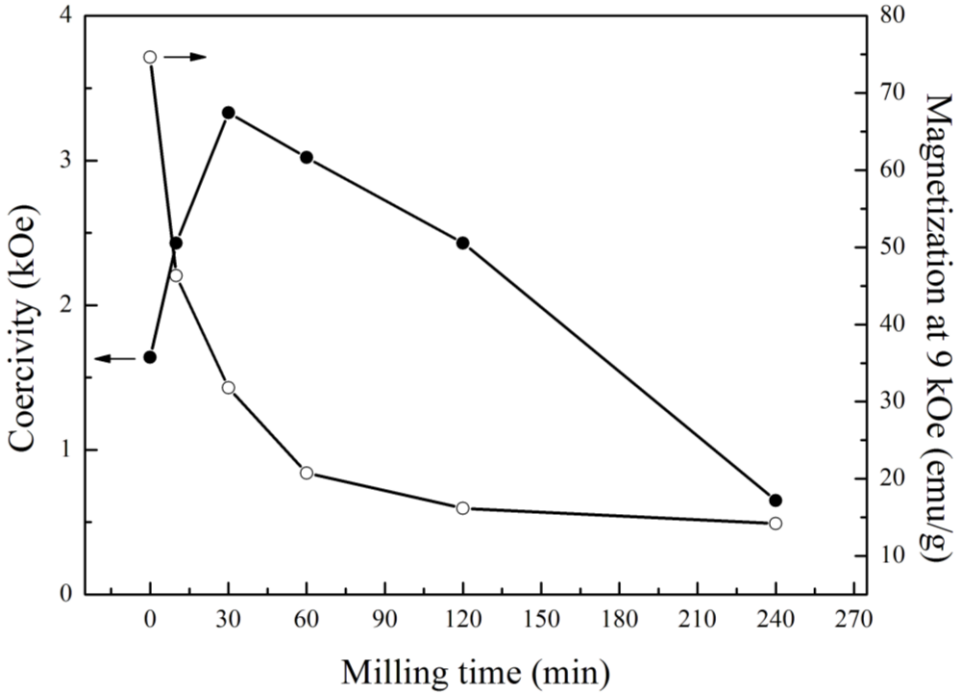

Figure 7.4 Coercivity & magnetization at 9 kOe as a function of milling time

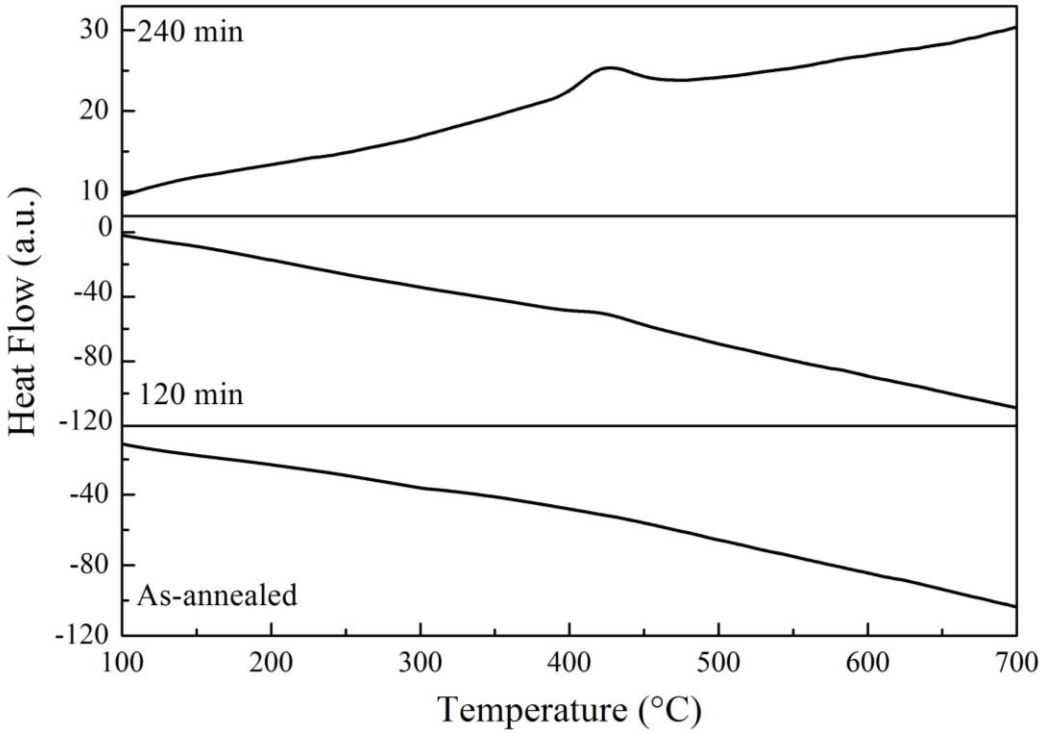

Figure 7.5 DTA curves for as-annealed τ-phase $Mn_{53}Al_{43}C_3Zr_1$ and as-milled for 120 min and 240 min

Initial increase in coercivity was followed by a subsequent decrease upon further milling as shown in Figure 7.4. The maximum coercivity was 3.3 kOe when milled for 30 min. Enhancement of coercivity with milling could be due to decrease of grain size as can be seen from peak broadening in the XRD pattern. However, the formation of the amorphous materials and the effect of chemical ordering of the $L1_0$ phase could be responsible for the decrease of coercivity with further milling. To evaluate the effect of chemical ordering of the $L1_0$ phase in a quantitative way, the following equation was used to calculate the ordering parameter *S*

$$S \cong 0.77\sqrt{\frac{I_{(110)}}{I_{(111)}}} \tag{7.1}$$

where $I_{(110)}$ and $I_{(111)}$ are the integrated intensities of the (110) and (111) diffraction peaks from the XRD patterns. Figure 7. 6 shows the dependence of long-range ordering parameter on milling time and correlation between coercivity on S. Slight increase of S was observed when milled for 10 min, showing short-time milling could enhance the ordering. Further milling caused decrease of S, indicating the order-disorder transformation during mechanical milling. As expected, coercivity increases with *S* as shown in Figure 7.6 (b), since magnetic anisotropy is proportional to the degree of order in $L1_0$ structure.

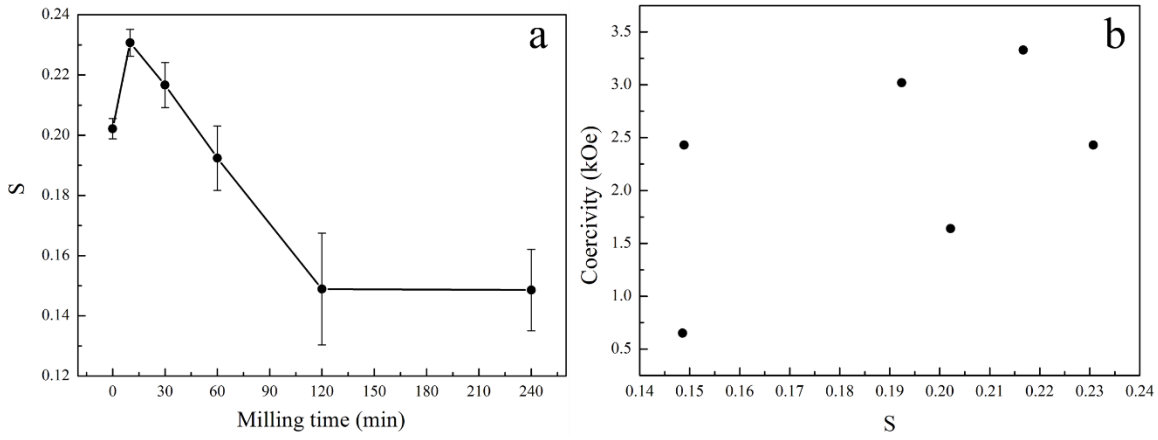

Figure 7.6 (a) The dependence of long-range ordering parameter on milling time; (b) Coercivity as a function of ordering parameter

7. 3. 2 Phase transformation and magnetic properties of ε-phase milled (ε-milled) alloy

Figure 7.7 shows the XRD patterns of ε-milled samples after conversion to τ phase. The conversion was conducted by heat treatment at 500℃ for 10 min followed by water-quenching. The milling time ranges from 1 h to 16 h. The samples have mainly ordered $L1_0$ structure with the presence of an increasing fraction of ε phase, β-Mn phase and ZrO phase with elongated milling time, as can be seen from the increase of peak intensities from those phases compared to that of τ phase. Earlier work shows that in the mechanical milling process, the resulting product is obtained from the competition between the increase of stresses in the system, which destabilizes it, and the thermodynamics tendency to equilibrium. Thus amorphization could occur due to the destabilization process. Meanwhile, some room-temperature stable phases, including ε phase, β-Mn phase and ZrO phase, could also be induced even before heat treatment, which might not be detected by XRD due to their low amounts. Since τ phase forms

through heat treatment from ε phase, heat treatment of amorphous materials would induce the formation of more equilibrium phases. As expected, the XRD peaks are getting broader with milling time, which were solely due to grain size reduction, since strain would be released during heat treatment.

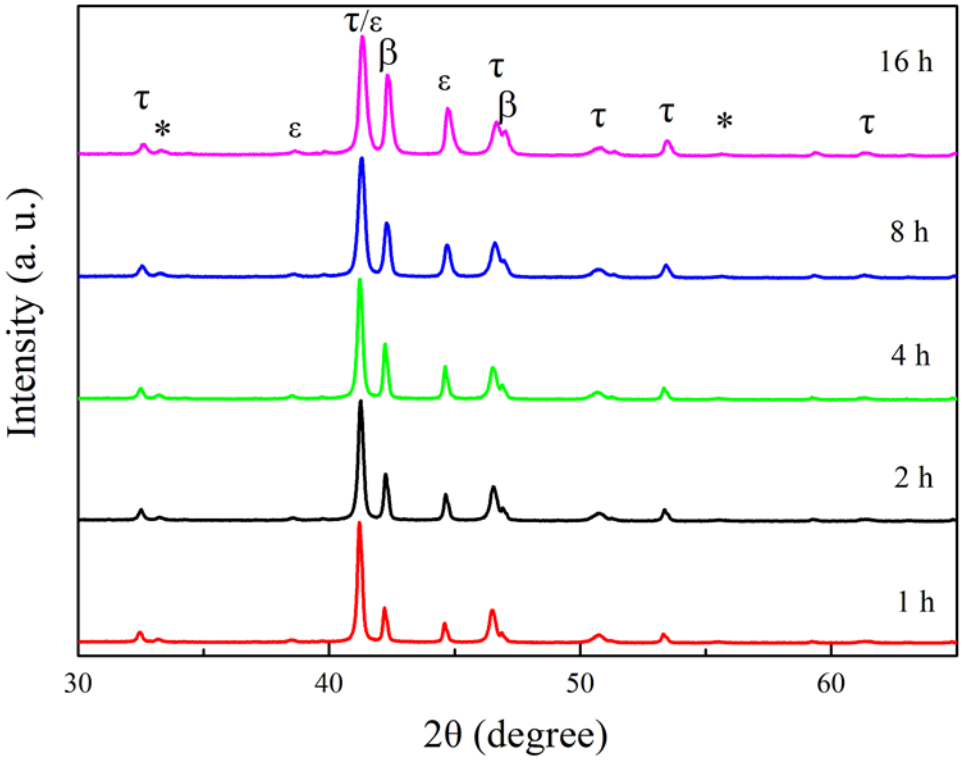

Figure 7.7 XRD patterns for ε-milled samples after conversion to τ phase

Figure 7.9 shows the hysteresis loops at 300 K of the samples milled for different times. Similar to the τ-milled samples, the coercivity increases to 3.5 kOe with the short milling time ~2 h. However, the dramatic loss of coercivity with further milling in τ-milled samples does not occur, as a relatively consistent coercivity result for sample milled up to 16 h. It might be attributed to its microstructure of platelet-like particles observed in [Ref.13]. The decrease in the magnetization with milling time was observed due to the formation of other equilibrium phases, including ε, ZrO, and β phases, as

shown in the XRD patterns. But the decrease is less dramatic than in the τ-milled samples, since no chemical ordering is lost during conversion from ε phase to τ phase. A kink in the hysteresis loop of 16-h milled sample indicates the existence of amorphous materials, which could be eliminated by elongated heat treatment.

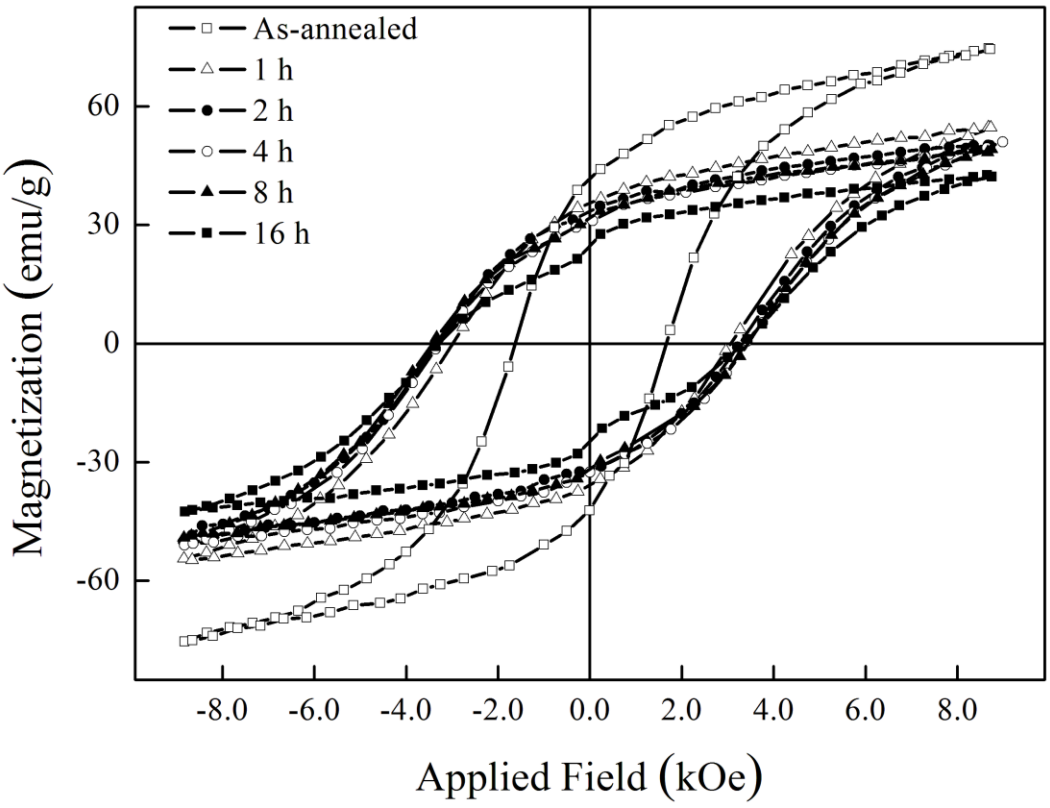

Figure 7.8 Hysteresis loop for ε-milled samples after conversion to τ phase

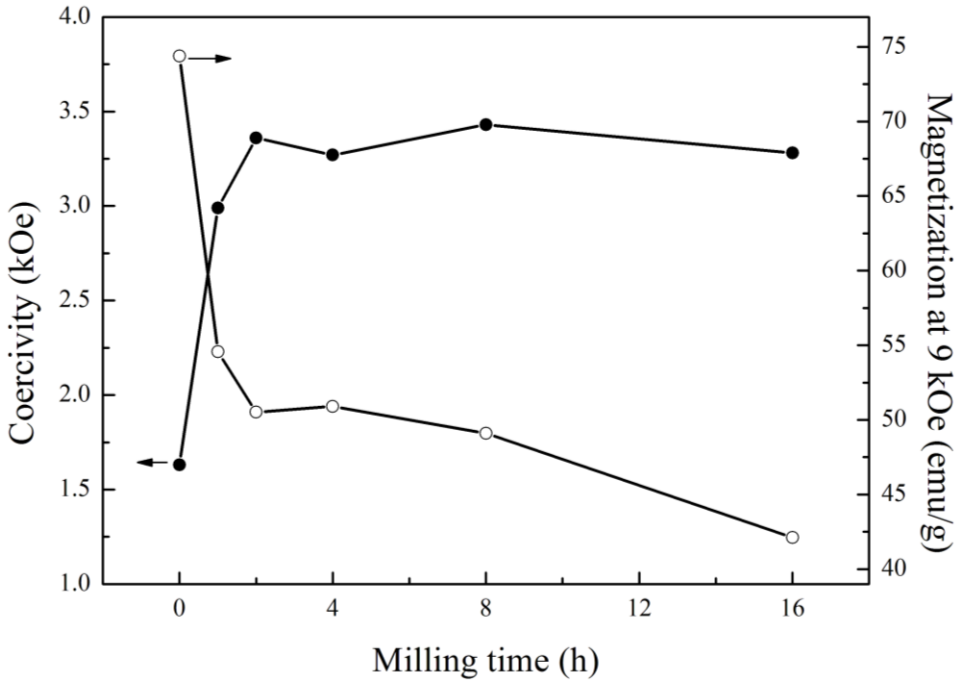

Figure 7.9 Coercivity & magnetization at 9 kOe vs milling time

7. 4 Conclusion

In summary, the effects of surfactant-assisted mechanical milling on magnetic properties for ε-phase and τ-phase $Mn_{53}Al_{43}C_3Zr_1$ alloys were investigated. In both cases, the loss of magnetization was attributed to the formation of room-temperature stable phases, including ε phase, β-Mn phase and ZrO phase. In τ-milled alloy, initial increase in coercivity when milled ~30 min was due to decrease of grain size, while loss of chemical ordering in $L1_0$ structure with further milling resulted in a subsequent decrease. In ε-milled alloy, an increase in coercivity with milling time ~ 2 h and being consistent with further milling might be related to its microstructure of platelet-like particles.

References

1 Zeng, Q., Baker, I. & Yan, Z.-c. Nanostructured Mn–Al permanent magnets produced by mechanical milling. *Journal of Applied Physics* **99**, 08E902-908E902-903 (2006).

2 Zeng, Q., Baker, I., Cui, J. & Yan, Z. Structural and magnetic properties of nanostructured Mn–Al–C magnetic materials. *Journal of Magnetism and Magnetic Materials* **308**, 214-226 (2007).

3 Park, J., Hong, Y., Bae, S., Lee, J., Jalli, J., Abo, G., Neveu, N., Kim, S., Choi, C. & Lee, J. Saturation magnetization and crystalline anisotropy calculations for MnAl permanent magnet. *Journal of Applied Physics* **107**, 09A731-709A731-733 (2010).

4 Van Den Broek, J., Donkersloot, H., Van Tendeloo, G. & Van Landuyt, J. Phase transformations in pure and carbon-doped Al< sub> 45</sub> Mn< sub> 55</sub> alloys. *Acta Metallurgica* **27**, 1497-1504 (1979).

5 Yanar, C., Wiezorek, J., Soffa, W. & Radmilovic, V. Massive transformation and the formation of the ferromagnetic $L1_0$ phase in manganese-aluminum-based alloys. *Metallurgical and Materials Transactions A* **33**, 2413-2423 (2002).

6 Kurtulus, Y. & Dronskowski, R. Electronic structure, chemical bonding, and spin polarization in ferromagnetic MnAl. *Journal of Solid State Chemistry* **176**, 390-399 (2003).

7 Massalski, T. B., Okamoto, H., Subramanian, P. & Kacprzak, L. *Binary alloy phase diagrams*. (ASM international, 1990).

8 Pareti, L., Bolzoni, F., Leccabue, F. & Ermakov, A. Magnetic anisotropy of MnAl and MnAlC permanent magnet materials. *Journal of Applied Physics* **59**, 3824-3828 (1986).

9 Fazakas, E., Varga, L. & Mazaleyrat, F. Preparation of nanocrystalline Mn–Al–C magnets by melt spinning and subsequent heat treatments. *Journal of Alloys and Compounds* **434**, 611-613 (2007).

10 Saito, T. Magnetic properties of Mn–Al system alloys produced by mechanical alloying. *Journal of Applied Physics* **93**, 8686-8688 (2003).

11 Chaturvedi, A., Yaqub, R. & Baker, I. A comparison of τ-MnAl particulates produced via different routes. *Journal of Physics: Condensed Matter* **26**, 064201 (2014).

12 Lucis, M. J., Prost, T. E., Jiang, X., Wang, M. & Shield, J. E. Phase Transitions in Mechanically Milled Mn-Al-C Permanent Magnets. *Metals* **4**, 130-140 (2014).

13 Chakka, V., Altuncevahir, B., Jin, Z., Li, Y. & Liu, J. Magnetic nanoparticles produced by surfactant-assisted ball milling. *Journal of Applied Physics* **99**, 08E912 (2006).

Chapter 8 Conclusions

In this chapter, a brief summary on $L1_0$-type permanent magnetic materials, FeNi and MnAl alloys, is presented. This research focuses mainly on the fabrication of $L1_0$-type magnetic materials and improvement on their magnetic properties, saturation magnetization and coercivity.

In stoichiometric Fe-Ni alloys, slight decrease in grain size (extensively increase in grain boundary) was caused by high-energy mechanical alloying, while the initial increase in internal strain (extensively dislocation density) was followed by a subsequent decrease with further alloying. However, the decrease of the net defects concentration was revealed by Doppler broadening positron annihilation spectroscopy, which is due to enhancement of chemical homogeneity and annihilation of vacancies/vacancy agglomerate at grain boundaries in the alloy. Thus, the mechanical alloying technique could not be used to generate more defects in Fe-Ni alloy. Furthermore, decrease of relative permeability with internal strain was attributed to the pinning of domain walls by dislocations.

Amorphous metallic glass $Fe_{32}Ni_{52}Zr_3B_{13}$, prepared by rapid solidification, undergoes crystallization during high-energy mechanical milling. It's due to the enhanced vacancy-type defect concentrations allowing growth of pre-existing Fe(Ni) nuclei. The milling and enhanced vacancy concentration also de-stabilizes the glass, leading to decreased crystallization temperatures for both phases, and ultimately eliminating the glass transition altogether. During the crystallization process, FeNi phase with higher crystallization temperature crystallized earlier than $Zr_3Ni_{20}B_6$ phase with lower

crystallization temperature, indicating milling-induced crystallization is a temperature-independent process.

In near-equiatomic MnAl alloy, improvement of saturation magnetization, ~ 128.0 ±1 emu/g, was achieved in $Mn_{53}Al_{43}C_3Zr_1$ alloy, which is prepared by rapid solidification followed by heat treatment. Results from Rietveld refinement on $Mn_{54}Al_{43}C_3$ and $Mn_{53}Al_{43}C_3Zr_1$ revealed that the Zr substituted the antiferromagnetically coupled Mn atoms in Al layer. To further improve the coercivity in $Mn_{53}Al_{43}C_3Zr_1$, microstructure modification was conducted by addition of excessive C and through surfactant-assisted mechanical milling separately. Decrease of grain size with C addition and the formation of some nonmagnetic phases enhanced the coercivity to 3.5 kOe, but the decrease of the saturation magnetization was caused by the formation of the nonmagnetic phases. Grain refinement could also be achieved in mechanically milled ε-phase and τ-phase $Mn_{53}Al_{43}C_3Zr_1$ powders, which enhanced the coercivity ~ 3.5 kOe in both cases. However, the formation of other equilibrium phases, including ε phase, β-Mn phase and ZrO phase, during the milling induced the loss of magnetization in both τ- and ε-milled alloys.